SLAC-PUB-694
December 1969
(TH) and (EXP)

VECTOR DOMINANCE MODEL INVESTIGATIONS AT SLAC*

Zaven G. T. Guiragossián

Stanford Linear Accelerator Center
Stanford University, Stanford, California 94305

(Invited talk given at the International Seminar on Vector Mesons and Electromagnetic Interactions, Dubna, September 23-26, 1969.)

*Work supported by the U. S. Atomic Energy Commission.

Since most of the current investigations at SLAC are relevant in one way or another with the Vector Meson Dominance[1] model, in my talk I shall try to summarize the results of several SLAC experiments and discuss their implications. Being the last speaker in this interesting Seminar, perhaps such a summary of several topics can serve the purpose of showing us where current VMD concepts need to be modified and where a better dynamical understanding is required prior to VMD applications.

The discussed experimental results can be divided in the following VMD related topics: (a) $\sigma_{tot}(\gamma p)$ and the forward vector meson photoproduction cross sections; (b) vector meson photoproduction by linearly polarized photons; (c) single pion photoproduction in the t-and u-channels and $\pi^- p \longrightarrow \rho^o n$; (d) t-channel Δ-photoproduction and $\pi^+ p \longrightarrow \rho^o \Delta^{++}$; (e) A-dependence of $\sigma_{tot}(\gamma A)$ and $\sigma(\gamma A \longrightarrow \pi A)$; and (f) ep inelastic scattering processes.

I. $\sigma_{tot}(\gamma p)$ and Forward Vector Meson Photoproduction

During the course of this year, three different methods were used at SLAC to obtain measurements of the total hadronic γp cross section from threshold to 16 GeV photon energies. Since the experimental methods used in obtaining these measurements were quite different, a short discussion on these methods would be of general interest before we examine the new data.

A. Laser induced photon beam

An almost monochromatic and polarized photon beam is prepared based on an investigation done concurrently at Yerevan (F. R. Arutyunian et al.[2]) and Tufts University (R. Milburn[3]). A high energy electron beam (up to 16 GeV) is intercepted over a distance of 5 meters and at an angle of ~ 3 mrad by ruby laser light (6943 Å, 1.786 eV, 2 joule maximum output, 50 nsec pulse lengths). The backscattered Compton radiation is collimated to an angular definition of 10^{-5} rad.

When the laser light is polarized, a few hundred almost monochromatic and ~95% polarized, high energy photons are obtained by 10^{11} electrons in a 1 μsec pulse. However, due to the laser cooling requirement, this beam is available only for 2 pulses/sec. This rate matches well with the detector cycle time in our experiment[4] — a 2-meter hydrogen bubble chamber. Figure 1 shows the experimental beam layout and the photon energy spectra, obtained from kinematical fits to e^+e^- pair-production events and those from the reaction $\gamma p \to p\pi^+\pi^-$ (shaded histograms). Using the e^+e^- pairs as a reliable photon flux monitor, the count of hadronic events yields the following total cross sections, at three separate photon energy exposures:

at k_γ =	1.44	2.84	4.66 GeV
$\sigma_{tot}(\gamma p)$ =	145.1 ± 5.7	131.3 ± 4.3	124.2 ± 3.9 μb

B. Tagged photon beam

A tagged photon beam was developed at SLAC from a low intensity positron beam of energies up to 19.5 GeV. Utilizing the bremsstrahlung process on a very thin radiator, the scattered positron is momentum analyzed and recorded by counter telescopes with known momentum-to-space correlation. The emitted photon energy is found by $k_\gamma = E^e_{in} - E^e_{out}$. The photon tagging system measures the incident photon flux and at the same time provides an effective trigger to indicate the presence of a known energy photon at the experimental target. Unfortunately, very few photons can be recorded during the short pulse length of this accelerator, thus limiting the experimenters to use only about 1000 photons/sec.

Once the presence of a known energy photon is indicated at the experimental target, a good hadronic event is detected by small pulse-height signals from lead-scintillator sandwich counters together with the absence of γ or electron-induced showers in a forward shower counter. Figure 2 gives the experimental

arrangements of this system and the results of $\sigma_{tot}(\gamma p)$ measurements[5] are displayed in Fig. 3. From this experiment it is seen that the total hadronic γp cross section drops with energy in a very slow manner to a value of 113 ± 2.5 μb at 16.5 GeV.

C. $q^2 \rightarrow 0$ extrapolation from inelastic ep scattering

A third and a newer method of measuring $\sigma_{tot}(\gamma p)$ consists in extrapolating the inelastic ep scattering differential cross sections to correspond to zero mass for the exchanged virtual photons. Under the single-photon-exchange assumption, the inelastic ep scattering cross section is related to the total hadronic cross sections by virtual photons in the following representation[6]:

$$\frac{d^2\sigma}{d\Omega dE'}(ep \rightarrow We') = \Gamma(E, E', \theta)\left[\sigma_T(q^2, W) + \epsilon\sigma_L(q^2, W)\right] \qquad (1)$$

where the virtual photon spectrum is measured by

$$\Gamma(E, E', \theta) = \frac{\alpha}{4\pi^2}\left(\frac{K}{q^2}\right)\left(\frac{E'}{E}\right)\frac{2}{1-\epsilon} \qquad (2)$$

Here, the virtual photon polarization parameter is given by

$$\epsilon(E, E', \theta) = \frac{1}{1 + 2\left(1 + \frac{\nu^2}{q^2}\right)\tan^2\left(\frac{\theta}{2}\right)}$$

where $q^2 = 4EE' \sin^2(\theta/2)$, is the virtual photon mass squared, with energy $\nu = E-E'$ and θ is the electron scattering angle in the laboratory system. The effective mass of the final hadrons produced in this process is $W = (M^2+2M\nu-q^2)^{1/2}$ and the corresponding real photon energy to produce such a final state is $K = (W^2-M^2)/2M$. In Eq. (1), $\sigma_T(q^2, W)$ is the total γp hadronic cross section by virtual photons polarized transversely to their momenta $\vec{q}$ and in the limit of $q^2 \rightarrow 0$, this cross section becomes $\sigma_{tot}(\gamma p)$ with center-of-mass energy W.

Accordingly, $\sigma_L(q^2, W)$, the cross section by longitudinally polarized virtual photons, vanishes in the same q^2 limit due to the gauge invariance condition.

Using the 8 and 20 GeV/c spectrometer systems, a group of MIT and SLAC experimenters have measured the inelastic ep scattering cross sections at small q^2 values. Some of these measurements are represented in Fig. 4, together with functional fits to the data and the $q^2 \rightarrow 0$ extrapolated points. From several such measurements and fits, the above relations are used to obtain values of $\sigma_{tot}(\gamma p)$, as a function of W. Figure 5 displays the results of this experiment.[7] At lower center-of-mass γp energies a rich structure is seen due to isobar formations, very much like the πp total cross sections.

Now we discuss recent SLAC measurements of the forward vector meson photoproduction cross sections; of particular interest to VMD applications are the zero momentum transfer extrapolated values which are equivalent to Compton scattering: $\frac{d\sigma}{dt}(\gamma p \rightarrow V^o p)$ at $t = 0$. In an experiment which covers 5.5 to 17.8 GeV photon energies, the 1.6 GeV/c spectrometer is used with a bremsstrahlung beam and the recoil protons are momentum analyzed to give missing mass yield curves at fixed recoil angles. In Fig. 6, the subtracted proton yield from adjacent bremsstrahlung tip energy runs is shown for a fixed momentum transfer value. After corrections for several factors, such spectra are fit to solve for several resonance parameters and smooth background levels and the amount of each particle's production is determined. Corrections are made also to account for the ω^o contribution under the ρ^o step size. In this experiment[8] measurements at t values of less than 0.1 or 0.2 $(GeV/c)^2$ are not possible. For this reason, the authors have searched for a reasonable functional representation to fit to the t-distribution data with a minimum number of parameters and thus to obtain the t=0 cross sections. Such a representation may be obtained by

relating under VMD the process $\gamma p \rightarrow V^o p$ with that of $V^o p \rightarrow V^o p$ and further, by connecting the $V^o p$ elastic scattering cross sections with quark model relations[9] which relate to πp and Kp elastic scattering measurements. Therefore, in such a functional representation, in principle there should not be any free parameters once the γ-V^o coupling constant is known in the relation:

$$\frac{d\sigma}{dt}(\gamma p \rightarrow V^o p) = \frac{\alpha}{4}\left(\frac{\gamma_V^2}{4\pi}\right)^{-1} \frac{d\sigma}{dt}(V^o p \rightarrow V^o p) \quad .$$

Figure 7 shows the measured cross-sectional momentum transfer dependence in ρ^o photoproduction, at the indicated energies. The curves shown are not fits to the data. These are absolute evaluations obtained from measured πp elastic cross sections inserted in the VMD/quark-model relationship given in this figure. The constant C_ρ is determined at one energy t-spectrum and thereafter held fixed. The excellent agreement between the curves and the data points indicate the validity of both model dependent assumptions. Figure 8 exhibits the results of ϕ^o photoproduction data, where similarly, the curves are obtained by the inserted VMD/quark-model representation. I have summarized the results of several experiments for ρ^o photoproduction in Fig. 9 and those for ω^o and ϕ^o photoproduction in Fig. 10. The latest DESY-MIT results are not included in these figures. These have been discussed earlier by S.C.C. Ting at this Seminar, where it was shown that the forward ρ^o photoproduction cross sections behave very much like the πp elastic cross sections in their energy dependence.

The results which we have discussed so far are connected by a VMD relationship which is free of interference terms among the vector meson photoproduction amplitudes. The assumptions which enter into this relationship are summarized in one of our recent studies.[10] Thus, the total hadronic γp cross section is

related to forward vector meson photoproduction by:

$$\sigma_{tot}(\gamma p) = \sqrt{4\pi\alpha} \sum_{V} \left[\left(\frac{\gamma_V^2}{4\pi} \right)^{-1} \cdot \frac{1}{1+\beta_V^2} \cdot \frac{d\sigma}{dt} (\gamma p \rightarrow V_t^o p) \Big|_{t=0} \right]^{\frac{1}{2}} \hbar c \qquad (3)$$

where β_V is the ratio of real over imaginary parts of the scattering amplitude $A(\gamma p \rightarrow V^o p)$ at the forward direction and V_t^o is the part of transversely polarized vector meson. However, experimental observation shows that, in the forward direction, the transversality requirement in V_t^o is already satisfied and need not be imposed by a transversality projection as in other cases. That is, in the forward direction, the vector mesons maintain the physical photon polarization of $\lambda = \pm 1$. Further, the ϕ^o amplitude relative phase is uncertain. This phase should be negative if the photon in SU(3) symmetry is a singlet U-spin zero particle and if the electromagnetic interactions conserve U-spin. In his talk at this Seminar, S. B. Gerasimov investigated modifications to the above VMD relation, due to spin dependent effects in the photoproduction of vector mesons. The required modification in Eq. (3) is a term $\left(1 + \frac{\sigma_\perp}{\sigma_{||}}\right)$ multiplying the factor $\left(1+ \beta_V^2\right)$ in the denominator. Here $\sigma_\perp (\sigma_{||})$ is the forward photoproduction cross section for vector mesons which are transversely polarized and which have their polarization aligned perpendicular (parallel) to the photon electric polarization vector. As we shall see in the following section, preliminary results indicate that the effect of such a term in Eq. (3) would be small.

In Fig. 11, the validity of this VMD relationship is examined. All of the known $\sigma_{tot}(\gamma p)$ measurements are shown, except for the new DESY results which now agree with the trend of others. The shaded area is the right-hand side evaluations in Eq. (3), with all experimental errors taken into consideration (open circle points). In this calculation the ω^o and ϕ^o coupling constants are

held fixed to the values of $\gamma_\omega^2/4\pi = 3.70 \pm 0.70$ and $\gamma_\phi^2/4\pi = 2.75 \pm 0.40$ and γ_ρ is varied to seek an agreement. The result is a value of $\gamma_\rho^2/4\pi = 0.40$ if the ϕ^o phase is additive and 0.35 if otherwise. In this Seminar, J. E. Augustin presented the recently updated Orsay results for these coupling constants, where the photon is on the vector meson's mass shell. The changes are in the ρ^o and ϕ^o values; the colliding beam experiment improved values are $\gamma_\phi^2/4\pi = 2.88 \pm 0.23$ and from ρ^o leptonic decays, $\gamma_\rho^2/4\pi = 0.46 \pm 0.04$.

II. Vector Meson Photoproduction by Linearly Polarized Photons

The laser induced photon beam discussed earlier, is utilized also to obtain linearly polarized photons. The amount of such polarization is very high, ~95% at 2.8 GeV and ~93% at 4.7 GeV photons. Here, we discuss some of the interesting preliminary results[11] which are part of an 800,000 picture exposure in the SLAC/LRL 2-meter hydrogen bubble chamber.

Vector meson photoproduction by linearly polarized photons can best be used to investigate the various exchange mechanisms in these processes. Specifically, we are able to isolate the large diffractive amplitudes in these processes by examining the vector meson decay correlations with respect to the beam photon electric polarization direction.

The vector meson photoproduction reactions are isolated among the topological 3-prong events. After track geometrical reconstruction and kinematical fits the following final states are categorized

$$\begin{aligned} &\text{(a)} && \gamma p \to p\pi^+\pi^- \\ &\text{(b)} && \gamma p \to p\pi^+\pi^-\pi^o \\ &\text{(c)} && \gamma p \to pK^+K^- \end{aligned} \qquad (4)$$

Figure 12a, b shows the $\pi^+\pi^-$ effective mass spectra from reaction (4a) events at 2.8 and 4.7 GeV photon energies, respectively. ρ^o production is the dominant channel in this final state. The superimposed curves are from a maximum likelihood fit to the data assuming p-wave Breit-Wigner resonance shapes for Δ^{++} and ρ^o photoproduction in addition to phase space. Also, a factor[12] of $(m_\rho/m_{\pi\pi})^4$ modifies the ρ^o shape to account for the unsymmetrical resonance form. To explain such a form, an interference model has been suggested[13] where in addition to ρ^o formation, photons couple directly to pion pairs and where one of the pions rescatters off the target proton. This model gives an unsymmetrical resonance shape and predicts that the exponential slope of $d\sigma/dt$ decreases with increasing dipion mass, around the ρ^o region. As shown in Fig. 13, supporting evidence for such an interference model is found in a streamer chamber experiment[14] using a high energy bremsstrahlung beam. The effect of such a model on ρ^o region decay distributions is negligible and better data are required to establish uniquely the existence of interfering diagrams, as seen on Fig. 13.

The analysis of vector meson decay correlations with linearly polarized photons can be viewed in a coordinate system given in Fig. 14. Here, the production plane of $\gamma p \rightarrow V^o p$ contains the x-z axes, and the decay polar and azimuthal angles, with respect to the quantization axis, are θ and ϕ. The angles Φ and Ψ define the relative orientations of the production and decay planes, with respect to the electric polarization vector of the beam photon, in this system. Vector meson decay intensity distributions are analyzed in terms of nine parameters, utilizing a most general[15] normalized functional form, specifically, for

linearly polarized photons:

$$I(\theta,\phi,\Phi) = \frac{1}{2\pi}\cdot\frac{3}{4\pi}\left\{\left[\frac{1}{2}\left(1-\rho_{00}^{(0)}\right)+\frac{1}{2}\left(3\rho_{00}^{(0)}-1\right)\cos^2\theta - \rho_{1-1}^{(0)}\sin^2\theta\cos 2\phi - 2\sqrt{2}\,\mathrm{Re}\rho_{10}^{(0)}\sin\theta\cos\theta\cos\phi\right]\right.$$

$$- P\cos 2\Phi\left[\rho_{00}^{(1)}\cos^2\theta + \rho_{11}^{(1)}\sin^2\theta - \rho_{1-1}^{(1)}\sin^2\theta\cos 2\phi - 2\sqrt{2}\,\mathrm{Re}\rho_{10}^{(1)}\sin\theta\cos\theta\cos\phi\right]$$

$$\left.+ P\sin 2\Phi\left[\mathrm{Im}\rho_{1-1}^{(2)}\sin^2\theta\sin 2\phi + 2\sqrt{2}\,\mathrm{Im}\rho_{10}^{(2)}\sin\theta\cos\theta\sin\phi\right]\right\}$$

In this representation, $\rho_{ij}^{(\lambda)}$ are the vector meson spin density matrix elements and P refers to the percentage of beam linear polarization. Utilizing the measurement of these density matrix elements, several combinations can be constructed which give an understanding of dynamical mechanisms. Among the most relevant measurements are the vector meson photoproduction polarization asymmetry $\sum$, and the parity exchange asymmetry P_σ:

$$\sum = \frac{\sigma_{\parallel}-\sigma_{\perp}}{\sigma_{\parallel}+\sigma_{\perp}} = \frac{\rho_{11}^{(1)}+\rho_{1-1}^{(1)}}{\rho_{11}^{(0)}+\rho_{1-1}^{(0)}}$$

and (5)

$$P_\sigma = \frac{\sigma_+ - \sigma_-}{\sigma_+ + \sigma_-} = 2\rho_{1-1}^{(1)} - \rho_{00}^{(1)}$$

where $\sigma_+(\sigma_-)$ is the cross section for $\gamma p \rightarrow V^o p$ due to natural (unnatural) parity exchange mechanisms.

The expected strong decay correlations are examined in Fig. 15, where it is seen that the ρ^o decay plane is mostly oriented along the beam photon electric polarization direction, as expected from a predominant diffraction mechanism. Figure 16 shows the existing measurements[11,16] of $\sum$, in $\gamma p \rightarrow \rho^o p$, where a

value of $\Sigma = 1$ corresponds to pure diffractive amplitudes. The cross-sectional asymmetry in reaction (4a), between natural and unnatural parity exchange processes, is given in Fig. 17, where contributions from unnatural parity exchanges are found to be small for this reaction. Various model dependent predictions can be tested readily. For example, a quark model for this interaction requires[17] that the statistical tensor[18] $\mathrm{Im}T_2^2$ vanish, when the photon polarization vector is perpendicular to the scattering plane and when the quantization axis is normal to the $\gamma p \rightarrow \rho^o p$ production plane. Figure 18 shows that such a prediction is well satisfied. This statistical tensor is measured by the expectation value of: $-5/4 \langle \sin^2\theta \sin 2\phi \rangle$.

The ω^o photoproduction properties are studied by the analysis of reaction (4b) events. Figure 19 displays the $\pi^+\pi^-\pi^o$ mass spectra, where a special selection on the reconstructed photon energy values is used to purify the ω^o sample. A similar decay correlation analysis is performed, where we find drastic differences in comparison to ρ^o photoproduction. For example, the distribution in the angle Ψ is found to be flat and the deduced parity exchange asymmetry $P_\sigma \approx 0$, as shown in Fig. 20. This indicates that natural and unnatural parity exchanges contribute about equally in $\gamma p \rightarrow \omega^o p$ dynamics. In constrast to ρ^o photoproduction, at these energies ω^o photoproduction has large non-diffractive contributions, presumably from the one-pion-exchange mechanism. In the following table, the vector meson photoproduction properties from this experiment are summarized; the cross sections are given in μb or $\mu b/(\mathrm{GeV/c})^2$.

	k_γ = 2.8 GeV		k_γ = 4.7 GeV
$\gamma p \rightarrow \rho^o p$			
σ	20.1 ± 1.2		15.2 ± 0.7
$d\sigma/dt$ at t=0	151 ± 15		115 ± 10
$\gamma p \rightarrow \omega^o p$			
σ	4.2 ± 0.5		2.4 ± 0.4
σ_{diff}		1.1 ± 0.5	
$(d\sigma/dt)_{diff}$ at t=0		11.0 ± 4.0	
$\gamma p \rightarrow \phi^o p$			
σ	0.33 ± 0.13		0.45 ± 0.16
$\gamma p \rightarrow \rho^- \Delta^{++}$			
σ	1.7 ± 0.7		0.7 ± 0.3
$\Gamma_{\rho\pi\gamma}$(MeV) OPE deduced:		0.14 ± 0.06	
$\Gamma_{\omega\pi\gamma}$(MeV) world average:		1.18	

III. Single Pion Photoproduction and $\pi^- p \rightarrow \rho^o n$

Single pion photoproduction and ρ^o pion production are processes which can be related directly by Vector Meson Dominance. Assuming isospin conservation, the reaction

$$\pi^- p \rightarrow \rho^o n \qquad (6)$$

in the time-reversed mode, compares with the isovector photon part of single pion photoproduction. Here, it is assumed that a direct γ-to-ρ^o transition can take place, with a definite coupling constant $\gamma_\rho^2/4\pi$, on the transverse polarization

components of the ρ^o. In such a transition, q^2 dependent effects, to account for the massless photon on one side and massive vector mesons on the other side, can play an important role especially at moderate energies. This issue is as yet unresolved and requires further theoretical understanding. We shall take the point of view that a geometrical solution may be obtained to account for this effect. Such a solution would be helpful to arrive at a more complete theoretical understanding where q^2 extrapolation effects, possibly in correlation with W, the total center-of-mass energy, are explained.

A. t-channel

The isovector photon contribution can be isolated by taking the cross-sectional average of π^+ and π^- photoproduction from the reactions:

$$\gamma p \rightarrow \pi^+ n \tag{7}$$

and

$$\gamma n \rightarrow \pi^- p \tag{8}$$

In one-pion-exchange, the photon isovector and isoscalar amplitudes, A_V and A_S, in reaction (7) are in the $|A_V + A_S|^2$ combination and in reaction (8) in the $|A_V - A_S|^2$ combination. Therefore, the average of both cross sections, removes the unknown interference term and measures the predominant $|A_V|^2$. Earlier, in Fig. 11 we observed the relative level of $|A_S|^2$ and $|A_V|^2$ contributions in γ-V^o transitions and found that experimentally $|A_S/A_V|^2 \sim 2\%$.

There has been extensive measurements of reactions (7), (8) and

$$\gamma p \rightarrow \pi^o p \tag{9}$$

differential cross sections. Figure 21 shows the relative cross-sectional behavior in the t-and u-channels for reactions (7) and (9). Reaction (7) is characterized by a sharp forward peak and as seen in Fig. 22, at higher energies there are three different exponential slopes in the momentum transfer distribution.[19,20] The

curves drawn on this figure are merely to guide the eye. Several Regge pole parametrizations have been attempted and as yet, there does not seem to be a satisfactory theoretical interpretation which explains the data of single-pion photoproduction both by unpolarized and linearly polarized photons. Figure 23 gives the measurements of π^--to-π^+ photoproduction ratio on deuterium,[19, 21, 22] R; this ratio is used in extracting the reaction (8) differential cross sections by $\sigma^- = R\sigma^+$.

As a measure of the isovector photon amplitude, the available data is utilized to form the π^+-π^--averaged differential cross section, $1/2\left[\sigma(\gamma p \longrightarrow \pi^+ n) + \sigma(\gamma n \longrightarrow \pi^- p)\right]$, at a given center-of-mass energy. This distribution can be compared directly with the VMD prediction, given by the following expression and the data of reaction (6):

$$\frac{\alpha}{4}\left(\frac{\gamma_\rho^2}{4\pi}\right)^{-1}\left(\frac{p_{\pi^-}}{p_\rho}\right)^2_{c.m.} \cdot \frac{E(s_\gamma)}{E(s_\rho)}\, P_{\rho^o}(t)\, \frac{d\sigma}{dt}(\pi^- p \longrightarrow \rho^o n) \qquad (10)$$

Here, E(s) is the cross-sectional energy dependence of reaction (6), and P_{ρ^o} is the ρ^o transverse polarization projection. The spin density matrix element of the ρ^o, $\rho_{ik}(t)$, are deduced from an analysis of the ρ^o decay distributions. As such, the transverse polarization projection P_{ρ^o} is equal to the element ρ_{11} when the correspondence is with pion photoproduction by unpolarized photons. Also, the combination of spin density matrix elements of $\rho_{11} + \rho_{1-1}$ describes a vector particle's transverse polarization state perpendicular to the production plane and similarly, $\rho_{11} - \rho_{1-1}$ describes the state with transverse polarization parallel to the production plane. Therefore, another VMD relationship can be constructed which relates the measurement of pion photoproduction polarization asymmetry, $\sum = (\sigma_\perp - \sigma_{||})/(\sigma_\perp + \sigma_{||})$, from reactions (7) and (8) with the spin density matrix

elements of ρ^o's from reaction (6):

$$A(\pi^+,\pi^-) = \frac{\sum(\gamma p \to \pi^+ n) + R(\pi^-/\pi^+)\ \sum(\gamma n \to \pi^- p)}{1 + R(\pi^-/\pi^+)} = \frac{\rho_{1-1}}{\rho_{11}} \qquad (11)$$

The prevailing question in all of this is: in which reference system these ρ^o spin density matrix elements ρ_{ik} must be evaluated, so that only the physical photon-like properties are abstracted. Earlier, the helicity reference[24] system was considered to be a natural frame for such an application. However, in view of the spin rotational properties of massive particles under Lorentz transformations, theoretical considerations[25] have shown, that the unique choice of the helicity frame for ρ^o's, a priori, is not well justified. That is, for VMD applications a criterion of choice on the quantization axis does not exist free of additional assumptions, where this axis lies in the production plane of reaction (6). In one of our recent studies[26] we have shown that the density matrix element evaluation in the ρ^o helicity frame does not reproduce the polarization asymmetry measurements of photoproduction as required from Eq. (11). This result is found on Fig. 24. To find an agreement, it was necessary to evaluate the ρ^o spin density matrix elements in a system where the element ρ_{10} is suppressed by a unitary transformation. This is equivalent to a dynamical rotation of the quantization axis within the production plane. The element ρ_{10} describes the quantum-mechanical admixture of transverse and longitudinal polarizations. Further, such a unitary transformation was generalized[26] to account for the large s-wave interference contributions in the ρ^o region, so that these could be handled directly in the ρ^o-region decay angular distribution analyses. Figure 24b shows the resultant agreement[26] in this transversality system, with the available data[27,28] and a theoretical calculation.[29] Equivalently good agreement is found in this system, in the VMD predictions of Eq. (10) when compared[26] with linearly

polarized and unpolarized photoproduction data of reactions (7) and (8), as shown on Fig. 25. This agreement is reached with a γ–ρ coupling constant value of $\gamma_\rho^2/4\pi = 0.40$; a result similar to that found in Fig. 11.

We may expect that a proper dynamical q^2 extrapolation in correlation with $W = \sqrt{s}$ should reproduce the above geometrical results. It has been shown, by a model dependent investigation which is good in the forward direction[30] and by studying the behavior of invariant amplitudes,[31] that the helicity frame is the correct frame to use only at very high energies; that is at energies where the $q^2 = m_\rho^2$ effect is negligible. For example, in the helicity frame of reaction (6) the model dependent study required a 40% correction at 4 GeV which reduces to a few percent at 16 GeV pion energies. Thus, if this dynamical coordinate rotation is equivalent to the proper q^2 extrapolation, then we may predict that at very high energies ($\gtrsim$ 16 GeV) the measurement of the element ρ_{10} in the helicity frame of reaction (6) would be negligibly small.

B. u-channel

Single pion photoproduction data in the u-channel, recently has been available from SLAC. In one of the experiments, these small cross sections were measured,[32] using the 1.6 GeV/c spectrometer to detect the π^+ backward scattering from reaction (7); and in another,[33] the 20 GeV/c spectrometer is used, to detect the proton forward scattering from reaction (9). In these experiments the covered u range extended out to values of 1.5 $(GeV/c)^2$. The momentum transfer distributions show such a smooth variation that it is not possible to guess at the dominant exchange mechanism which characterize the reaction dynamics. Several Regge trajectories may be exchanged and further, the absence of reaction (8) measurements make it difficult to constrain the various possibilities. However, we propose to use VMD predictions from the above expression

(10) and u-channel data[34] of reaction (6), as a reasonable representation for the isovector part of single-pion photoproduction and thus, introduce an additional constraint on the various dynamical model parametrizations. That is, in the absence of u-channel measurements for reaction (8), this VMD constraint may be used to discriminate between various phenomenological fits to the data of reactions (7) and (9). In turn, the present VMD results may be checked with such fits to the data of all single-pion photoproduction channels, when the isovector part is isolated. Therefore, we shall use VMD in the u-channel of reaction (6) to abstract the isovector amplitude entering in the processes of single-pion u-channel photoproduction and specifically, make a direct test on a phenomenological description[35] where Regge poles for the Δ, N_α and N_γ trajectory exchanges are used.

Figure 26 shows the SLAC data of reaction (7) in the u-channel along with a specific theoretical fit to the data assuming the above three Regge trajectories are exchanged. The reaction (9) data is illustrated on Fig. 27 and the fits are from the same Regge pole parameterizations. In all cases, adequate descriptions are obtained, out to values of $|u| < 1.0$ $(GeV/c)^2$. We now present our analysis for the u-channel properties of reaction (6) which are relevant to this investigation.[34] Figure 28a displays the u-channel differential cross section, where the backward peak has a value of 64.5 ± 12.9 $\mu b/(GeV/c)^2$. The ρ^o spin density matrix elements are determined again in a complete transversality system. Figure 28d gives the ratio ρ_{1-1}/ρ_{11} which in VMD represents the behavior of the isovector part in the cross-sectional polarization asymmetry $\sum_v$, for $\gamma_v p \rightarrow \pi^+ n$.

Using isospin decomposition, the u-channel photoproduction scattering amplitudes can be separated in terms of isovector and isoscalar photon parts. Further, the isovector photon part can be decomposed in terms of I = 3/2 and

I = 1/2 u-channel baryon exchange contributions. Thus,

$$A(\gamma p \rightarrow \pi^+ n) = \sqrt{1/3}\, A_V(s,u,3/2) - \sqrt{2/3}\, A_V(s,u,1/2) - \sqrt{2/3}\, A_S(s,u,1/2)$$

$$A(\gamma n \rightarrow \pi^- p) = \sqrt{1/3}\, A_V(s,u,3/2) - \sqrt{2/3}\, A_V(s,u,1/2) + \sqrt{2/3}\, A_S(s,u,1/2) \qquad (12)$$

$$A(\gamma p \rightarrow \pi^o p) = \sqrt{2/3}\, A_V(s,u,3/2) + \sqrt{1/3}\, A_V(s,u,1/2) - \sqrt{1/3}\, A_S(s,u,1/2)$$

In any phenomenological parameterization[35,36] to fit the available data of reactions (7) and (9), the fractional contributions to the u-channel cross section can be isolated in terms of the I = 3/2, I = 1/2 exchanges and their interference. The normalized contributions are designated in an obvious notation by: $I_\Delta(s,u)$, $I_N(s,u)$ and $I_{\Delta N}(s,u)$, where the sum of these is unity. A free parameter in such fits is δ, the isoscalar over the isovector parts in the I = 1/2 u-channel exchanges. This represents the isoscalar-isovector photon admixture in the photonucleon system. Hence, using these fitted parameter values, the isovector photon contributions in reaction (7) can be isolated and this can be compared directly with VMD results of Eq. (10), by the following relation:

$$\frac{d\sigma}{du}(\gamma_V p \rightarrow \pi^+ n) = \frac{d\sigma}{du}(\gamma p \rightarrow \pi^+ n)\left[I_\Delta(u) + \frac{I_N(u)}{(1+\delta)^2} + \frac{I_{\Delta N}(u)}{1+\delta}\right] \qquad (13)$$

From the isospin decomposition in (12), the phenomenologically parameterized value of δ is expected to be a negative fraction.

In Fig. 29a the u-channel differential cross section of reaction (7) from 4.16 - 5.23 GeV photon energies[32] is shown, where we have made an energy extrapolation to 4.0 GeV using the experimentally determined[32] energy dependence of k^{-3}. In the absence of any isoscalar photon contribution, that is with Δ-exchange dominance, the VMD prediction from Eq. (10) should agree with the results in this figure. The presence of large N-exchange contributions enter subtractively in the

I = 1/2 parts of the scattering amplitude and cause a relative depression in the u-channel cross section of reaction (7) with respect to the isovector VMD predictions of Eq. (10). Figure 29b shows the normalized fractional contributions in the u-channel cross section of reaction (7) due to Δ-exchange, N-exchange (N_α and N_γ) and their interference, from a specific Regge pole phenomenological parameterization[35] to this reaction. A value of $\delta = -0.376$ is used at 4.0 GeV. In this fit, it is also found that a satisfactory solution is obtained, only when the $N_\gamma(1512)$ trajectory contribution is included, with a relatively large value for its residue function.

The points on Fig. 30b represent the VMD measure on the isovector part $\gamma p \rightarrow \pi^+ n$ u-channel cross section, at 4.0 GeV. The curve drawn in this figure is from Eq. (13), the parameterization shown in Fig. 29b and the cross sections in Fig. 29a. Accordingly, the abstracted isovector part of $\gamma p \rightarrow \pi^+ n$ agrees well with VMD predicted isovector cross sections, in the u range of $|u| < 1.0$ $(GeV/c)^2$. Again, the agreement is obtained[34] with a value of $\gamma_\rho^2/4\pi = 0.40$.

A direct comparison, between the VMD points in Fig. 30b and the $\gamma p \rightarrow \pi^+ n$ cross-sectional measurements in Fig. 29a, indicate the presence of large contributions from I = 1/2 u-channel exchanges. Since a large value is required for the N_γ trajectory residue function,[35] over that for the N_α trajectory, our comparison in Fig. 30b together with this, implies a strong coupling of $N_\gamma(1512)$ with the isovector γ-nucleon channel. In VMD, this is equivalent to a strong coupling of $N_\gamma(1512)$ with the virtual-ρ^o-nucleon system. All of these implications become significantly interesting when the measured $\sigma_{tot}(\gamma p)$ cross-sectional energy dependence is examined, in comparison with measured $\pi^+ p$ and $\pi^- p$ total cross sections. Combining VMD and quark model predictions[37] a relationship is obtained that is shown on Fig. 31. The curve drawn on this figure comes from the

indicated relation; the measurements of $\pi^+ p$ and $\pi^- p$ total cross sections and the γ-ρ coupling constant with a value of $\gamma_\rho^2/4\pi = 0.40$. The agreement between this curve and the measured $\sigma_{tot}(\gamma p)$ values is excellent, except for the $N_\gamma(1512)$ region. The $\sigma_{tot}(\gamma p)$ energy spectrum has a large over enhancement at the $N_\gamma(1512)$ region, in support of the predominant $N_\gamma(1512)$ coupling to the γ-nucleon channel. The indicated predominance of $N_\gamma(1512)$ coupling to the isovector-γ-nucleon (or virtual-ρ^o-nucleon) channel is an interesting phenomenon and requires further detailed investigations, both theoretically and experimentally.

IV. Δ-Photoproduction and $\pi^+ p \rightarrow \rho^o \Delta^{++}$

In Fig. 32 the momentum transfer distribution of several two-body photoproduction reactions is shown, for a relative comparison. In relation to all of the measured channels, it is seen that the reaction:

$$\gamma p \rightarrow \pi^- \Delta^{++} \qquad (14)$$

has the largest forward cross section. This cross section and its energy dependence are measured, using the SLAC 20 GeV/c spectrometer to analyze the pions at a fixed scattering angle. The missing mass distributions, obtained from several end point energy bremsstrahlung beams, are fitted with a few competing channel assumptions. Figure 33 displays the results of an earlier measurement[38] of reaction (14) cross sections, in comparison with those of reaction (7) (dashed lines). It is seen that both reactions have the same cross-sectional behavior beyond the momentum transfer value of 0.2 $(GeV/c)^2$. However at smaller t, these Δ-photoproduction cross sections rise sharply as e^{12t}, where a maximum value is attained at $|t| \sim m_\pi^2$ with a dip at the forward direction. These differences, between both reactions at small t values, indicate that different types of exchanges take place among both channels. Figure 34 displays the preliminary results of

recent SLAC measurements for the differential cross sections of reactions[39] (14) and:

$$\begin{aligned} &\text{(a)} \quad \gamma p \rightarrow \pi^+ \Delta^0 \\ &\text{(b)} \quad \gamma n \rightarrow \pi^- \Delta^+ \\ &\text{(c)} \quad \gamma n \rightarrow \pi^+ \Delta^- \end{aligned} \tag{15}$$

at 16 GeV. The curves drawn on this figure are merely to guide the eye. The cross sections for reaction (15b) and (15c) are obtained from deuterium to hydrogen target subtractions. Figure 35 gives the deuterium-to-hydrogen ratio for Δ-photoproduction with the same charged pions. If an isospin-one single particle exchange is the dominant mechanism in these reactions, then the ratio of (15c) to (15a) should be 3:1, or equivalently, the deuterium-to-hydrogen ratio for Δ-photoproduction with π^+'s should be 4:1. Similarly, the same ratio with π^-'s should be 4:3. The results given in this figure indicate that the measured ratios for the π^+'s are not well satisfied by this reaction hypothesis, whereas those for the π^-'s are in agreement.

The photon isoscalar and isovector amplitudes enter in opposite phases in reaction (15b), as compared with the additive phases in reaction (14). The presence of a photon isoscalar-isovector interference term is seen readily in Fig. 36. Here, for comparison, the single-pion photoproduction π^- to π^+ ratio (smooth curve) is also given at 16 GeV. In VMD applications, the effect of these photon isoscalar-isovector (or ρ^0-ω^0) interference terms are removed, in a manner discussed previously, by taking the cross-sectional average of reactions (14) and (15b).

Clearly, with such a rich variety entering in the reaction dynamics of Δ-photoproduction, VMD comparisons cannot be made prior to an adequate dynamical description. This is due to the additional requirement, that we must have

a knowledge on the behavior of amplitudes when crossing in the reaction's description, from the s-to the u-channel. That is, for VMD applications, in addition to time-reversal invariance and isospin conservation assumptions, the analytical behavior of amplitudes must be known when crossing, for example, from $\pi^+ p \rightarrow \gamma \Delta^{++}$ (in the s-channel) to $\gamma p \rightarrow \pi^- \Delta^{++}$ (in the u-channel). In this case, it is the s-channel amplitudes that relate by VMD to the cross sections of:

$$\text{(a)} \qquad \pi^+ p \rightarrow \rho^o \Delta^{++}$$

and (16)

$$\text{(b)} \qquad \pi^+ p \rightarrow \omega^o \Delta^{++}$$

whereas, the Δ-photoproduction process is carried in the reaction description's u-channel. When several Regge trajectories are exchanged in reactions (16) and Δ-photoproduction processes, under s-to-u crossing, amplitudes with even signature trajectories do not change sign but the amplitudes with odd signature trajectories reverse their sign. For these reasons, it is not possible to obtain VMD predictions from reactions (16), without a proper dynamical description. Such a model dependent description is obtained from a recent study.[40] Regge parameterizations are made, on the measurements[41] of reaction (16) cross sections and vector meson density matrix elements, assuming that π, ρ, A_1, A_2 and B trajectories could be exchanged.

In Fig. 37, the average of Δ^- and Δ^{++} photoproduction cross sections is shown. The crossed points are from a VMD prediction using the data of reaction (16a), while the s-to-u channels crossing effects are neglected. A large and systematic disagreement is obtained, when such dynamical effects are not considered. The smooth curve is obtained,[40] by applying VMD, only after a proper dynamical description of reactions (16) is at hand. Primarily, the difference

comes from the interference term as a result of the unnatural parity exchanges (π, A_1), entering in reaction (16a). Such a term changes sign, when the amplitudes are crossed from the s- to the u-channel. This curve agrees well with the Δ-photoproduction data, except at the very forward direction. Although, sufficient uncertainties exist in the analysis of both the pion and photon initiated reactions, that firm statements cannot be made, this example, reiterates the necessity of having an adequate dynamical description prior to the VMD application.

V. A-Dependence of $\sigma(\gamma A \longrightarrow \pi A^*)$ and $\sigma_{tot}(\gamma A)$

The studies of photon transmission through nuclear matter and high energy photonuclear processes have paused as a challenge to both theoretical and experimental investigations. The measurements of photon initiated processes on complex nuclei have shown that our initial understanding are only within an order of magnitude in so far as the cross-sectional dependence on nucleon number A and further, the dependence of these on photon energy, is concerned. The level of the total hadronic γp cross-sectional values, implies a nuclear mean free path of 700-800 fermies for photons. Such a large mean free path value, allows the photons to penetrate at all parts of the nuclear volume. So that, on a nucleus, a volume dependent photon interaction rate is obtained, which is proportional to the number of nucleons, A. On the other hand, if the hadronic interactions of photons are mediated by vector mesons which have a mean free path of a few fermies, then only the surface of the nucleus participate in the interaction processes and the rest of the nucleus is overshadowed by the surface nucleons. In this case, a surface dependent photon interaction rate is obtained which is proportional to $A^{2/3}$. However, the mediating virtual vector mesons are recreated continually by the photons; and the photons have access to all depths in the nuclear medium. Therefore, in this case also,

there should be some volume dependent effects as well. The energy dependence of both surface and volume effects may well be different, since these virtual hadrons can be reabsorbed readily, inside the nuclear medium. In this picture, the understanding of photonuclear absorption processes extends[42] itself naturally to neutrino induced processes, when these are mediated by pions; compare $\gamma \rightarrow V^0$ with $\nu_\ell \rightarrow \ell^{\pm}(\pi^{\mp})$.

The photonuclear absorption problem is complicated further by the presence of (a) two-step interaction processes,[43] where delicate cancellations occur as a function of energy; (b) q^2 extrapolation effects[44] in such two-step processes (cf. Fig. 44); (c) exclusion principle and nucleon-nucleon interaction correlation effects;[45] (d) and a proper multiple scattering treatment on outgoing hadrons. In this Seminar, K. Gottfried presented in detail some of these issues.

Recently, SLAC cross-sectional measurements[46] of single pion photoproduction processes on complex nuclei:

$$\gamma A \longrightarrow \pi^{\pm} A^* \qquad (17)$$

where made, at 8 and 16 GeV photon energies. The outcoming charged pions, from a bremsstrahlung beam, are momentum analyzed at a fixed angle, using the 20 GeV/c spectrometer system. The single meson photoproduction cross sections are obtained by fitting the pion yield spectra near the bremsstrahlung end-point energies and applying energy conservation. However, in this experiment the resolution is coarse enough that nuclear excitations up to 100 MeV are accepted. Recoiling nuclear products are not detected and the experimental uncertainties are due primarily to folding the momentum distribution of target nucleons in the above fitting procedure, assuming a condensed Fermi gas model. This model is used assuming a maximum nucleon momentum of 260 MeV/c, where a change of ± 40 MeV/c in this value results to a systematic change in the cross-sectional values of ± 16% at $t = -0.45$ and ± 1% at $t = -0.01$ $(GeV/c)^2$.

Figure 38 shows the momentum transfer dependence of Z_{eff}, which is the differential cross sections ratio, of single pion photoproduction from complex nuclei to that from hydrogen. The value of Z_{eff} obtained from each element are normalized by the value obtained at $t = -0.16$ $(GeV/c)^2$ for that element. The curves drawn on this figure are from the Fermi gas model, with a 260 MeV/c nucleon momentum cutoff value. The measurements of Z_{eff} do not agree with this model, at both small and large momentum transfers. This indicates the presence of several effects, which we discussed above, in these incoherent (charge-exchange) processes.

A definite energy dependence of Z_{eff} is predicted[43] from theoretical considerations of the two-step interaction process with VMD. Figure 39 displays the theoretical behavior of such a dependence, both on photon energy and target nucleon number A. In comparison with such a formalism, the measurements of Z_{eff} from this experiment, for π^+ photoproduction at 8 and 16 GeV, indicate that such a predicted energy dependence is not present. This comparison is shown on Fig. 40, where the curves are normalized to the carbon Z_{eff} measurements, at each momentum transfer value. The π^- photoproduction cross sections are measured also at 16 GeV. On Fig. 41, the π^-/π^+ photoproduction ratios on complex nuclei are given, where no statistically significant A-dependence is seen. These ratios have the same level as observed earlier from deuterium data.

The A-dependence of the total hadronic photoabsorption cross sections, $\sigma_{tot}(\gamma A)$, are measured in a counter arrangement experiment[5] which we discussed in Section I. The A-dependence in these cross sections is also predicted[43c] using the optical model, to describe the nucleus and assuming ρ-dominance, to describe the hadronic part in photoabsorption. In such a description, aside from nuclear density parameters, the A-dependence is given in terms of the

ρ-nucleon interaction total cross section, $\sigma_{tot}(\rho N)$. The A-dependence is displayed on Fig. 42, in the form of the measured cross-sectional ratios, $\sigma_{tot}(\gamma A)/A\sigma_{tot}(\gamma p)$. In this form, the A-dependence is insensitive to the value of the coupling constant $\gamma_\rho^2/4\pi$ and primarily, it is a function of $\sigma_{tot}(\rho N)$. The curves drawn on this figure are from the optical model formulation,[43c] with the indicated values for $\sigma_{tot}(\rho N)$. Here, the best fit value is obtained to be: $\sigma_{tot}(\rho N) = 20.4 \pm 2.7$ mb. The authors[5] have investigated the effect of a -0.20 fractional real part amplitude contribution and find, that this influences the above $\sigma_{tot}(\rho N)$ value, to within the quoted errors. Assuming ρ-dominance, and reducing the measurements of $\sigma_{tot}(\gamma N)$ to compensate for the ω^o and ϕ^o contributions,[10] the relation:

$$\sigma_{tot}(\gamma N)(\text{reduced}) = \left(\frac{\alpha}{4}\right)\left(\frac{\gamma_\rho^2}{4\pi}\right)^{-1} \sigma_{tot}(\rho N) \qquad (18)$$

yields a value of $\gamma_\rho^2/4\pi = 0.38 \pm 0.05$; in agreement with the results that we discussed previously.

The amount of surface nucleon overshadowing, by the hadronic part in the photoabsorption process on nuclei, is clearly manifested on Fig. 43. The cross-sectional ratios, $\sigma_{tot}(\gamma A)/\sigma_{tot}(\gamma p)$, measured at an average photon energy of $\sim$ 13 GeV, fall below the drawn line of $\sigma_{tot}(\gamma A)/\sigma_{tot}(\gamma p) = A$. A fit to these measured ratios, results to an A-dependence of $\sigma_{tot}(\gamma A)$, to be: $A^{0.90}$ at $\sim$ 13 GeV k_γ. A similar experiment from DESY,[47] results to an A-dependence of $A^{0.95\pm0.02}$, at an average photon energy of $\sim$ 5.5 GeV. Thus, in effect, there appears to be an energy dependence to the A-dependence. Such a phenomenon follows readily from a recent theoretical investigation[48] on the propagation of photons, by V. N. Gribov. Here, in the electromagnetic interactions of hadrons, the dependence on characteristic longitudinal distances or interaction duration

times are examined and specifically, for the hadronic total photoabsorption on nuclei, useful conclusions are obtained, irrespective of vector meson dominance assumptions. In this picture, photon propagation proceeds through fluctuations between the state of the quantum and its virtual decays into hadrons, having some characteristic mass μ. If at some lower limiting photon energies, this fluctuation time is $\delta \sim 1/\mu$, then at higher photon energies k, the duration in fluctuations of $\gamma \rightarrow$ hadrons $\rightarrow \gamma$, increases with photon energies and occurs in a time interval of $\delta \sim k/\mu^2$. In terms of the charge renormalization constant due to hadrons, Z_3, the quantity $1-Z_3$, represents part of the time that the photon spends in the hadronic states. This quantity has a Green's function integral representation, to describe the hadronic contributions to photon propagation. Thus, the convergence properties of this integral representation are examined under several limiting conditions.

In this picture, the photons interact with the nucleons of a nucleus only during a fluctuation that lasts for a time interval δ. The photon virtually decays into hadrons and these hadrons interact with nucleons inside nuclear matter, with an interaction mean free path ℓ. Let us consider first, a photon energy region such that $\delta \leq \ell$. Here, $\sigma_{tot}(\gamma A)$ is determined by: (a) the probability that a photon hits a nucleus having a radius R ($\sim \pi R^2$), (b) the probability that a hadronic fluctuation takes place ($\sim C_{\gamma h}$, cf. $\alpha/4\ (\gamma_\rho^2/4\pi)^{-1}$) and that, (c) this fluctuation occurs inside the nucleus ($\sim C_{\gamma h} \cdot R/\delta$), finally, (d) the probability that the created virtual hadrons have sufficient amount of time, to complete an interaction with any nucleons of the nucleus ($\sim \delta/\ell$).

Thus, $\sigma_{tot}(\gamma A) \sim \pi R^2 \cdot C_{\gamma h} \cdot R/\delta \cdot \delta/\ell \sim C_{\gamma h}\, \pi R^3/\ell \sim A \cdot \sigma_{tot}(\gamma N)$; in this photon energy region, the hadronic total photoabsorption process takes place throughout the nuclear volume. However, if the photon energy is now increased, so that $\ell < \delta < R$, then in the above, condition (d) is always satisfied and

$\sigma_{tot}(\gamma A) \sim C_{\gamma h} \cdot \pi R^3/\delta$; which signifies that these volume effect cross sections decrease as the photon energy increases. A further increase in the photon energy, increases δ proportionally, to bring in a regime where $\delta \gtrsim R$ and here, the probability that these hadronic fluctuations may develop outside the nucleus emerges. In this case, all the hadrons which are formed with a probability $\sim C_{\gamma h}$, will collide with the nucleus, with a cross section $\sim \pi R^2$. Hence $\sigma_{tot}(\gamma A) \sim C_{\gamma h} \cdot \pi R^2$, and as a function of photon energies, nuclear volume effects diminish and surface effects dominate. There exists a further condition of applicability, due to the convergence requirement in the photon propagation's integral representation; it is required that $\delta^2 \gg R\ell$. For example, in this case, if the characteristic hadronic mass μ, in photon fluctuations, is taken to be $\sim m_\rho$ and $\ell \sim 1/m_\pi$, then surface effects in $\sigma_{tot}(\gamma A)$ begin to develop, only after 10 GeV photon energies.

Gribov's arguments[48] are in agreement with the discussed experimental observations. And a current proposal,[49] to carry measurements of $\sigma_{tot}(\gamma A)$ at Serpukhov energies, would help to enhance several theoretical implications along this picture, in connection with photoproduction and electroproduction processes.

VI. ep Inelastic Scattering Processes

Measurements of the total ep inelastic differential cross sections introduce a new understanding on the nature of photons and the structure of nucleons, as probed by massive quanta. In this Seminar, some of the theoretical implications from these measurements were presented by J. D. Bjorken and others. Here, we discuss recent results from a SLAC-MIT collaboration experiment,[50,51] where at a fixed angle scattered electrons are detected and momentum analyzed using the 8 and 20 GeV/c SLAC spectrometer systems and, comment on VMD related[52,53] comparisons.

Several correction factors enter in the final experimental determination of the double differential cross sections, $d^2\sigma(E,E',\theta)/dE'd\Omega$ in ep inelastic scattering. Electronic dead-time effects are removed by limiting the data rate to at most one event in a 1.6 μsec beam pulse. The incident electron beam current is measured by induction toroid and secondary emission monitors ($\sim$ 0.5% uncertainties). Scattered electrons are separated from pions by shower and total-absorption counters ($\sim$ 88% detection efficiency). A 7 cm liquid hydrogen target is used and, by a separate detection system, the target density reduction due to beam localized heating is determined (a correction factor that varied from $\sim$ 4 to $\sim$ 13%). An empty target subtraction is required ($\sim$ 7% correction). The effect of electrons produced from π^o decays and subsequent pair productions is determined by observing e^+ yields ($\lesssim$ 15% correction). Finally, the data requires a complete understanding of radiative corrections[54] due to (a) internal and external bremsstrahlung, single and multiple photon emission ($\sim$ 2% corrections) and (b) the contributions in the inelastic scattering region from the radiative tail of elastic ep scattering (21 to 26% corrections).

In contrast with the deep inelastic ep scattering regions of large q^2 and ν, the cross-sectional q^2 dependence, at the first four isobar formation regions, behaves in a manner similar to that in ep elastic scattering. This dependence is observed on Fig. 45, where the isobar electroproduction cross sections are normalized, at the same q^2, by the values of ep elastic scattering cross sections. Beyond the threshold behavior, which is initiated by the equivalent photoproduction cross sections, the q^2 dependencies scale with elastic scattering; the form factor behavior in the isobar mass regions is similar to that of the nucleon. The curves drawn on this figure are from a coupled-channel relativistic N/D model calculation,[55] with specific form factors.

To stress the importance of radiative corrections, Fig. 46 displays: (a) the uncorrected data in the isobar regions, the elastic peak (reduced by a factor of 6) and the calculated radiative tail due to elastic scattering (dashed line); (b) the radiatively corrected ep inelastic cross sections and (c) the ratio of radiatively corrected to uncorrected cross sections. It is seen that large cross-sectional corrections are required at high hadron masses, W. The cross-sectional behavior as a function of W and q^2 is given on Fig. 47, for the q^2 regions of: (a) $0.2 \leq q^2 \leq 0.5$, (b) $0.7 \leq q^2 \leq 2.6$ and (c) $1.6 \leq q^2 \leq 7.3$ $(GeV/c)^2$. These results clearly show that the isobar formation cross sections rapidly diminish as q^2 increases, whereas the inelastic continuum region of large W has a much weaker form factor dependence on q^2.

Deep inelastic ep scattering cross sections are discussed[56] in terms of the structure functions $W_1(q^2, \nu)$ and $W_2(q^2, \nu)$, given in the relation:

$$\frac{d^2\sigma}{dE'd\Omega} = \frac{4\alpha^2 E'^2}{q^4} \cos^2 \frac{\theta}{2} \left[W_2(q^2, \nu) + 2W_1(q^2, \nu) \tan^2 \frac{\theta}{2} \right] \tag{19}$$

assuming a one-photon-exchange mechanism in these processes. The term outside the brackets is the Mott cross section which describes the scattering off an infinite mass target. A comparison between Eq. (1) and (19) relates the structure functions with the virtual photon total hadronic γp cross sections by transversely and longitudinally polarized massive photons:

$$W_1(q^2, \nu) = \frac{K}{4\pi^2\alpha} \sigma_T(q^2, \nu)$$

$$W_2(q^2, \nu) = \frac{K}{4\pi^2\alpha} \frac{q^2}{q^2 + \nu^2} \left(\sigma_T(q^2, \nu) + \sigma_L(q^2, \nu) \right) \tag{20}$$

where $K = \nu - q^2/2M$, is the equivalent physical photon energy, required to photoproduce a final hadronic state with center-of-mass energy W. Thus, for fixed q^2 and large ν values, asymptotically, the structure functions behave as:

$$W_1(q^2,\nu) \to \nu\ \sigma_T(q^2,\nu)$$
$$\nu W_2(q^2,\nu) \to q^2\left(\sigma_T(q^2,\nu) + \sigma_L(q^2,\nu)\right) \tag{21}$$

Experimentally, using Eq. (19), the structure functions W_1 and W_2 are separable at the crossing points of two fixed θ lines, on the (ν, q^2) kinematical plane. The method of separation is the same as for the nucleon form factors in elastic scattering.

The functional behavior of νW_2 can be investigated by:

$$\nu W_2(q^2,\nu) = \nu \frac{d^2\sigma/dE'd\Omega}{(d\sigma/d\Omega)_{Mott}}\left[1 + \frac{1}{1+R}\left\{2\left(1+\frac{\nu^2}{q^2}\right)\tan^2\frac{\theta}{2}\right\}\right]^{-1} \tag{22}$$

where, the sensitivity on $R = \sigma_L(q^2,\nu)/\sigma_T(q^2,\nu)$ is small, if the term in the curly brackets is much less than unity. In the absence of large angle measurements, Eq. (22) can be used to obtain limiting values on the behavior of $\nu W_2(q^2,\nu)$, by the extreme assumptions of R=0 and $R=\infty$. Bjorken originally suggested,[54] that in the deep inelastic region ($q^2 \to \infty$ but q^2/ν finite), the function $\nu W_2(q^2,\nu)$, should exhibit the property of scale invariance, by a dependence on only a single demensionless variable $\omega = 2M\nu/q^2$, instead of the two independent variables q^2 and ν. Also, based on different arguments,[52,58] the universal function νW_2, at large ω limits, is expected to approach a constant value.

Specific VMD predictions are given by Sakurai[52] on the q^2, ν dependences of cross sections. We list these and discuss the comparisons with experiment.

The virtual photon cross sections entering in Eq. (1) are given as:

$$\sigma_T(q^2,\nu) = \left(\frac{e}{f_\rho}\right)^2 \left(\frac{\mu^2}{q^2+\mu^2}\right)^2 \sigma_T^{\rho p}(K)$$

$$\sigma_L(q^2,\nu) = \left(\frac{e}{f_\rho}\right)^2 \left(\frac{\mu^2}{q^2+\mu^2}\right)^2 \frac{q^2}{\mu^2} \left(\frac{K}{\nu}\right)^2 \xi(K)\, \sigma_L^{\rho p}(K) \qquad (23)$$

where $\mu = m_\rho$ and $\sigma_{T(L)}^{\rho p}(K)$ are the vector-meson-nucleon total cross sections with vector meson polarizations T and L; T for polarization vectors perpendicular to the vector meson line-of-flight (helicities ± 1) and L for polarization vectors parallel to the line-of-flight (helicity 0); $\xi(K) = \sigma_L^{\rho p}(K)/\sigma_T^{\rho p}(K)$. Thus, asymptotically, $\sigma_L(q^2,\nu) \sim (1/q^2)$, $\sigma_T(q^2,\nu) \sim (1/q^4)$ and their ratio R, varies as q^2 for fixed ω:

$$R = \frac{\sigma_L(q^2,\nu)}{\sigma_T(q^2,\nu)} = \xi(K) \frac{q^2}{\mu^2} \left(1 - \frac{1}{\omega}\right)^2 \qquad (24)$$

Further, scale invariance is obtained with a definite asymptotic value in the functional behavior of νW_2:

$$\nu W_2 \longrightarrow \xi(\infty) \frac{\mu^2}{4\pi^2\alpha}\ \sigma_{\gamma p}(\infty) \left(1 - \frac{1}{\omega}\right)^3 \qquad (25)$$

Figure 48 presents the $\theta = 6^\circ$ and E = 13.5 GeV data ($0.7 \leq q^2 \leq 2.6$ (GeV/c)^2), in comparison with the VMD prediction, where a value of $\xi(K) = 1.5$ is used. The cross sections at a higher q^2 range ($1.6 \leq q^2 \leq 7.3$ (GeV/c)^2) are shown on Fig. 49, where a better comparison with VMD is achieved. The curves drawn on these figures adequately reproduce the deep inelastic ep cross sections.

Utilizing Eq. (22) and the cross-sectional measurements, the functional behavior of νW_2 is estimated, as shown on Fig. 50 for the 6° data and Fig. 51

for the 10^{o} data. In Fig. 50a the νW_2 points, from a q^2 range of $q^2 > 0.5$ $(GeV/c)^2$ are given, assuming R=0 in Eq. (22), whereas in Fig. 50c the same data are shown, assuming $R=\infty$. Figure 50e displays the νW_2 values, where $q^2 \leq 0.5$ $(GeV/c)^2$, under both R assumptions. Similarly, Fig. 51b exhibits the νW_2 behavior for R=0, Fig. 51d for $R=\infty$, at q^2 values of $q^2 > 0.5$ $(GeV/c)^2$. Among these, the best universal curve behavior for νW_2 is shown in Fig. 51b.

In the $R=\infty$ assumption ($\sigma_L \gg \sigma_T$), the νW_2 measurements do not follow a universal curve. But, in the R=0 assumption ($\sigma_T \gg \sigma_L$), beyond a threshold behavior as a function of ω, the νW_2 estimates appear to reach at the same value (~ 0.3), when $\omega \gtrsim 4$. However, here the results indicate a downward slope in νW_2, when $\omega \gtrsim 5$ in the 6^{o} data (Fig. 50), which is not apparent in the 10^{o} data (Fig. 51). This indicates that in the functional dependence of νW_2, in addition to the scale invariance variable ω, there exists a weaker q^2 dependence, to be taken into consideration specifically at high ω values. A more stringent remark applies with the expected asymptotic q^2 behavior of $\sigma_T(q^2, \nu)$. If on Fig. 51b, already a scale invariant universal curve behavior is arrived, then $\sigma_T \gg \sigma_L$, $\nu W_2(\omega) = \text{const.}$ and from Eq. (21) we obtain that $\sigma_T(q^2, \nu) \sim (1/q^2)$; which is in disagreement with the VMD predictions of Eq. (23). Using the 6^{o} and 10^{o} data alone, a preliminary attempt at separation of the structure functions is shown on Fig. 52. This is given in terms of the vector-meson-nucleon cross-sectional polarization ratio $\xi(K)$, as a function of q^2. The values of $\xi(K)$ increase[51] by $\sim 50\%$, in the range of q^2, from 1 to 4 $(GeV/c)^2$; whereas, it was expected[52] that ξ would not have a q^2 dependence.

Finally, Fig. 53 exhibits the cross-sectional overall q^2 dependence, in the deep inelastic ep scattering region, from the 6^{o} and 10^{o} data. The differential cross sections are divided by the Mott cross section and displayed for fixed values of W, the final hadronic effective mass in ep scattering. Division by the Mott

cross section, removes part of the known q^2 dependence, due to photon propagation. The curves drawn over the data points are merely to guide the eye. For a relative comparison, the equivalent elastic scattering cross-sectional ratio is also given. Thus, beyond $q^2 \gtrsim 1$ (GeV/c)^2, the ep scattering process is entirely dominated by the deep inelastic continuum where a much weaker q^2 dependence applies on the inelastic form factors. Moreover, this q^2 dependence weakens further with increasing final state hadronic masses, W.

In the deep inelastic continuum, the rise of cross sections with increasing values of W is consistent with a limiting condition[59] which implies that the form factors are bounded by the point charge scattering cross section:

$$\lim_{E \longrightarrow \infty} \left[\frac{d\sigma(ep)}{dq^2} + \frac{d\sigma(en)}{dq^2} \right] \geq \frac{1}{2} \frac{d\sigma}{dq^2} \text{ (point charge)}$$

Also, on general considerations, Markov[60] has remarked that at asymptotic energies, the total cross sections from neutrino, electron or photon beams, should have as lower bounds their corresponding point particle scattering cross sections. All of these reiterate that in these processes, as the asymptotic regions are approached, effects due to characteristic interaction lengths are relatively suppressed. Hence, the cross sections are a function of only the involved dynamical variables, in dimensionless combinations. In this sense, Matinian[61] finds that in ep inelastic scattering processes, among the dynamical variable dependences of s/μ^2, t/μ^2 and s/t, only the latter survive ($\cos \theta_t \sim \nu/\sqrt{q^2}$), in an equivalent Regge approach to this problem.

As we approach asymptotic regions (cf. Fig. 53) there does not appear to be a unique q^2 dependence in ep deep inelastic scattering; the higher is the hadronic effective mass value, the weaker is the q^2 dependence. Thus, the problem

seems to be concentrated on understanding the manner in which these asymptotic regions are approached, with the presence of effects due to interaction longitudinal distances,[48, 62] discussed earlier. These would enter in the description of the hadronic part of photon propagation and give an energy dependence to the q^2 dependence.

Acknowledgements

It is a pleasure to thank Prof. A. I. Alikhanian for his kind hospitality at the Yerevan Physics Institute, Armenia, during which time this manuscript was prepared. I would like to thank Dr. S. H. Matinian for several illuminating discussions and valuable remarks.

REFERENCES

1. For a recent review of VMD, cf. J. J. Sakurai, Currents and Mesons, (University of Chicago Press, Chicago, 1969).
2. F. R. Arutyunian et al., JETP 18, 218 (1964) and Phys. Letters 4, 176 (1963).
3. R. H. Milburn, Phys. Rev. Letters 10, 75 (1963).
4. SLAC-Tufts-UCB/LRL Collaboration, Phys. Rev. Letters 23, 498 (1969).
5. D. O. Caldwell et al., University of California, Santa Barbara, Preprint (September 1969).
6. L. N. Hand, Phys. Rev. 129, 1834 (1963).
7. MIT-SLAC Collaboration, E. D. Bloom et al., Report No. SLAC-PUB-653, Stanford Linear Accelerator Center, Preprint (September 1969).
8. SLAC-CIT-UCSB-NU Collaboration, R. Anderson et al., Report No. SLAC-PUB-644, Stanford Linear Accelerator Center, Preprint (August 1969).
9. B. Margolis, Nucl. Phys. B6, 687 (1968).
10. Z.G.T. Guiragossián and A. Levy, Nucl. Phys. B11, 449 (1969).
11. SLAC-Tufts-UCB/LRL Collaboration, contributions to the International Symposium on Electron and Photon Interactions at High Energies, Daresbury, England (September 1969).
12. M. Ross and L. Stodolsky, Phys. Rev. 149, 1172 (1966).
13. P. Söding, Phys. Letters 19, 702 (1966); A. Krass, Phys. Rev. 159, 1496 (1967).
14. M. Davier et al., Report No. SLAC-PUB-613, Stanford Linear Accelerator Center, Preprint (July 1969).
15. R. L. Thews, Phys. Rev. 175, 1749 (1968); K. Schilling, P. Seyboth and G. Wolf, Report No. SLAC-PUB-683, Stanford Linear Accelerator Center, Preprint (November 1969).

16. L. Criegee et al., Phys. Letters 28B, 282 (1968).

17. B. Gorczca and M. Hayashi, Report No. TPJU-4/69, Institute of Physics, Jagellonian University, Cracow, Preprint (1969).

18. A. Kotanski and K. Zalewski, Nucl. Phys. B4, 559 (1968).

19. P. Heide et al., Phys. Rev. Letters 21, 248 (1968).

20. A. M. Boyarski et al., Phys. Rev. Letters 20, 300 (1968).

21. A. M. Boyarski et al., Phys. Rev. Letters 21, 1767 (1968).

22. Z. Bar-Yam et al., Phys. Rev. Letters 19, 40 (1967).

23. M. Krammer and D. Schildknecht, Nucl. Phys. B7, 583 (1968).

24. I. Derado and Z.G.T. Guiragossián, Phys. Rev. Letters 21, 1556 (1968) and references therein.

25. H. Fraas and D. Schildknecht, Nucl. Phys. B6, 395 (1968).

26. Z.G.T. Guiragossián and A. Levy, Phys. Letters 30B, 48 (1969).

27. C. Geweniger et al., Phys. Letters 28B, 155 (1968) and Phys. Letters 29B, 41 (1969).

28. Z. Bar-Yam et al., contributions to the International Symposium on Electron and Photon Interactions at High Energies, Daresbury, England (September 1969).

29. J. Frøyland and D. Gordon, Phys. Rev. 177, 2500 (1969).

30. C. F. Cho and J. J. Sakurai, Report No. EFI-69-73, University of Chicago, Preprint (1969).

31. F. T. Meiere, Phys. Letters 30B, 44 (1969).

32. R. L. Anderson et al., Phys. Rev. Letters 23, 721 (1969) and Phys. Rev. Letters 21, 479 (1968).

33. D. Tompkins et al., Phys. Rev. Letters 23, 725 (1969).

34. Z.G.T. Guiragossián, Report No. SLAC-PUB-657, Stanford Linear Accelerator Center, Preprint (August 1969).

35. J. V. Beaupre and E. A. Paschos, Report No. SLAC-PUB-632, Stanford Linear Accelerator Center, Preprint (August 1969).

36. V. Barger and P. Weiler, Phys. Letters 30B, 105 (1969).

37. S. B. Gerasimov and V. A. Serdyutski, Sov. Journ. Nucl. Phys. 8, 323 (1969).

38. A. M. Boyarski et al., Phys. Rev. Letters 22, 148 (1969).

39. A. M. Boyarski et al., Contributions to the International Symposium on Electron and Photon Interactions at High Energies, Daresbury, England, September 1969.

40. E. Gotsman, Report Nos. UCSD-10P10-56 and UCSD-10P10-63, University of California, San Diego, Preprints (1969).

41. BDNPST Collaboration, Nucl. Phys. B7, 681 (1968). ABC Collaboration, Phys. Letters 27B, 174 (1968) and Phys. Letters 22, 533 (1966); Nucl. Phys. B8, 45 (1968).

42. J. S. Bell, "Weak interactions in the nuclear shadow," Report No. CERN TH-887 (1968) unpublished.

43. (a) K. Gottfried and D. R. Yennie, Phys. Rev. 182, 1595 (1969);
(b) S. J. Brodsky and J. Pumplin, Phys. Rev. 182, 1794 (1969);
(c) B. Margolis and C. L. Tang, Nucl. Phys. B10, 329 (1969).

44. W. Schmidt and D. R. Yennie, Phys. Rev. Letters 23, 623 (1969).

45. M. Nauenberg, Phys. Rev. Letters 22, 556 (1969); E. J. Moniz, G. D. Nixon, and J. D. Walecka, Contributions to the IIIrd International Conference on High Energy Physics and Nuclear Structure, Columbia University, New York, September 1969.

46. A. M. Boyarski et al., Report No. SLAC-PUB-671, Stanford Linear Accelerator Center, Preprint (October 1969).

47. H. Meyer et al., Contributions to the International Symposium on Electron and Photon Interactions at High Energies, Daresbury, England, September 1969.

48. V. N. Gribov, "High energy interactions of γ quanta and electrons with nuclei," IVth Winter Seminar on the Theory of the Nucleus and the Physics of High Energies, Part I, Leningrad (1969).

49. A. I. Alikhanian, G. L. Bayatian, G. A. Ispirian, S. H. Matinian, A. H. Ogannessian, and Z.G.T. Guiragossián, "Proposal to measure the total hadronic photoproduction cross section at the Serpukhov IHEP Accelerator," (September 1969).

50. E. D. Bloom et al., Phys. Rev. Letters 23, 930 (1969).

51. M. Breidenbach et al., Phys. Rev. Letters 23, 935 (1969); see also, L. W. Mo, Contributions to the IIIrd International Conference on High Energy Collisions, Stony Brook, New York (September 1969).

52. J. J. Sakurai, Phys. Rev. Letters 22, 981 (1969); C. F. Cho, G. J. Gounaris and J. J. Sakurai, Report No. EFI-69-54, University of Chicago, Preprint (1969).

53. Y. S. Tsai, Report No. SLAC-PUB-600, Stanford Linear Accelerator Center, Preprint (1969).

54. L. W. Mo and Y. S. Tsai, Rev. Mod. Phys. 41, 205 (1969); Y. S. Tsai, Proceedings of the International Conference on Nuclear Structure at Stanford University, 1963 (Stanford University Press, 1964).

55. P. L. Pritchett, J. D. Walecka, and P. A. Zucher, "A relativistic model for electroproduction of nuclear resonances," to be published in Phys. Rev.

56. S. D. Drell and J. D. Walecka, Annals of Phys. 28, 18 (1964).

57. J. D. Bjorken, Phys. Rev. 179, 1547 (1969).

58. H. D. Abarbanel, M. L. Goldberger, and S. B. Treiman, Phys. Rev. Letters 22, 500 (1969).

59. J. D. Bjorken, Phys. Rev. Letters 16, 408 (1966); Phys. Rev. 163, 1767 (1967).

60. M. A. Markov, "Form factors and total cross sections of weak and electromagnetic interactions," Report No. E2-4370, Dubna (1969).

61. S. H. Matinian, Yerevan Physics Institute, private communication.

62. B. L. Ioffe, "Space-time picture of photon and neutrino scattering and electroproduction cross section asymptotics," Report No. 694, ITEF, Moscow (1969).

FIGURE CAPTIONS

1. (a) Schematic layout of laser induced photon beam. (b)-(d) Photon energy spectra at 1.4, 2.8, and 4.7 GeV beam settings, as determined from e^+e^- pair-energy measurements and from events fitting the reaction $\gamma p \rightarrow p\pi^+\pi^-$ (solid histograms) (Ref. 4).
2. Schematic representation of tagged photon beam and detectors for the measurement of $\sigma_{tot}(\gamma A)$. The counters A_0 define incoming photon beam angles, S2 detect presence of outgoing hadrons and S1 determines absence of γ or e^+e^- pairs, in a given event (Ref. 5).
3. Measurements of $\sigma_{tot}(\gamma p)$, $\sigma_{tot}(\gamma d)$ and the deduced $\sigma_{tot}(\gamma n)$ using the experimental arrangement in the previous figure (Ref. 5).
4. $\sigma_{tot}(\gamma p)$ obtained from an extrapolation procedure (dark points) using $\theta = 1.5^o$ ep inelastic scattering cross-sectional measurements, as a function of q^2 and the final state hadronic mass W. K is the equivalent photon energy for a W c.m. (Ref. 7).
5. Measurements of $\sigma_{tot}(\gamma p)$ from $q^2 = 0$ extrapolation (dark points)of small angle ep inelastic scattering cross sections, as a function of K or W. Dashed lines, beyond $W \geq 2.3$ GeV, indicate the region of possible cross-sectional variation due to systematic errors (Ref. 7).
6. Subtracted proton yield curve in $\gamma p \rightarrow pX^o$, between photon end-point energy 14.5 and 13.0 GeV. The yield is measured by the 1.6 GeV/c spectrometer and given as counts/hodoscope element/10^{11} equivalent quanta. The solid curve is from a least square fit to the data, assuming π^o, ρ^o, ϕ^o and B^o (resonant shape) production over a smooth background (Ref. 8).

7. Momentum transfer distribution of $d\sigma(\gamma p \rightarrow \rho^0 p)/dt$ at incident photon energies, E_0. The solid curves drawn through the data points are from the quark-VMD relation, given on this figure, using $\pi^+ p$ and $\pi^- p$ measured differential cross sections and setting the parameter $C_\rho = 2.98 \times 10^{-3}$ (Ref. 8).

8. Momentum transfer distribution of $d\sigma(\gamma p \rightarrow \phi^0 p)/dt$ at the indicated incident photon energies. The solid curves drawn through the data points are from an equivalent quark-VMD relation, shown on this figure, using $K^+ p$, $K^- p$ and $\pi^- p$ measured differential cross sections with the adjustable parameter set at $C_\phi = 1.86 \times 10^{-4}$ (Ref. 8).

9. Compilation of forward ρ^0 photoproduction cross-sectional measurements at the indicated laboratories and given detection systems.

10. Compilation of forward ω^0 and ϕ^0 photoproduction cross sections, measured at the indicated laboratories.

11. Comparison of the Vector Meson Dominance relation (Eq. (3)), using the forward vector meson photoproduction cross sections from Figs. 9 and 10. The shaded area covers the extend of measurement errors. Agreement is found with the shown measurements of $\sigma_{tot}(\gamma p)$ using the indicated value of $\gamma_\rho^2/4\pi$. The level of ρ^0, ω^0 and ϕ^0 contributions is shown separately at ~ 6 GeV.

12. The $\pi^+\pi^-$ mass spectrum from $\gamma p \rightarrow p\,\pi^+\pi^-$ by the laser induced linearly polarized photon beam at (a) 2.8 GeV and (b) 4.7 GeV. The superimposed curves are from a maximum likelihood fit to the Dalitz plot distribution including ρ^0, Δ^{++} and phase space indicated contributions (Ref. 11).

13. The $\pi^+\pi^-$ mass spectrum, from a bremsstrahlung photon beam with a streamer chamber experiment (Ref. 14); (a) the $\pi^+\pi^-$ mass distribution fit to ρ^0 production and an interfering $\pi\pi$ background, (b) the variation in the slope parameter B as a function of dipion mass. The curve is from an interference model (Ref. 13).

14. Vector meson decay analysis coordinate system in linearly polarized photoproduction.

15. Correlation between ρ^o decay plane and photon polarization — the ψ distribution and, distributions in the polar and azimuthal ρ^o helicity frame angles; data from the laser induced linearly polarized photon beam (Ref. 11).

16. ρ^o photoproduction polarization asymmetry measurements (a) at 2.8 GeV (Ref. 11) in comparison with the data of (Ref. 16) at 2.25 GeV and (b) at 4.7 GeV, photon energies.

17. Parity exchange asymmetry distribution as a function of t, in ρ^o photoproduction at (a) 2.8 GeV and (b) 4.7 GeV (Ref. 11).

18. Behavior of the statistical tensor in $\gamma p \rightarrow \rho^o p$ as compared with a quark model prediction of Ref. 17, in the helicity, Jackson and Adair reference systems (Ref. 11).

19. The $\pi^+\pi^-\pi^o$ mass spectra from $\gamma p \rightarrow p\pi^+\pi^-\pi^o$ (a) at 2.8 GeV average energy and (b) with a restricted selection on the reconstructed photon energy, (c) at 4.7 GeV average energy with a similar selection in (d) (Ref. 11).

20. Measurement of the parity exchange asymmetry in ω^o photoproduction (Ref. 11).

21. Compilation of differential angular distribution measurements at 5 GeV, in single pion photoproduction channels.

22. Measurement of $\gamma p \rightarrow \pi^+ n$ differential cross sections at photon energies 3.4, 5, 8, 11 and 16 GeV, the curves drawn are merely to guide the eye (Refs. 19 and 20).

23. The ratio of π^- to π^+, single pion photoproduction on deuterium at the indicated photon energies (Refs. 19, 21 and 22); the curves are from a theoretical calculation (Ref. 29).

24. (a) ρ^o spin density matrix element ratio ρ_{1-1}/ρ_{11}, evaluated in the helicity reference system (Ref. 26). (b) VMD prediction of the π^+, π^- averaged photoproduction's polarization asymmetry. ρ_{1-1}/ρ_{11} ratios from 4.0 GeV $\pi^- p \to \rho^o n$, evaluated in the proposed transversality system (Ref. 26), for VMD comparison with current experiments (Refs. 27 and 28) and theoretical calculation (Ref. 29).

25. VMD predictions from Eq. (10) and ρ^o spin density matrix element evaluation in the transversality system, in comparison with π^+, π^- averaged photoproduction cross sections (Refs. 19 - 22). (a) at 3.4 GeV, by photons linearly polarized perpendicular to the production plane, (b) at 3.4 GeV and (c) at 5 GeV both by unpolarized photons (Ref. 26).

26. Measurement of u-channel $\gamma p \to \pi^+ n$ differential cross sections at the indicated photon energies, E (Ref. 32); the curves are from a phenomenological description where Regge poles for Δ, N_α and N_γ trajectory exchanges are fitted (Ref. 35).

27. Measurement of u-channel $\gamma p \to \pi^o p$ cross sections (Ref. 33) and fits to the data in a Regge trajectories exchange calculation (Ref. 35).

28. (a) u-channel cross section of 4.0 GeV $\pi^- p \to \rho^o n$, obtained by maximum likelihood fits to processes in the $\pi^- p \to \pi^+ \pi^- n$ data. (b) Evaluations of the transversality condition's dynamical rotation angle ψ, to suppress the ρ^o polarizations admixture due to the spin density element ρ_{10}, in $\pi^- p \to \rho^o n$. (c) Measurement of the ρ^o spin density matrix eigenvalue $\rho_{11} + \rho_{1-1}$. ϵ is the eigenvalue ratio as evaluated in the transversality over the helicity systems. (d) Vector Dominance Model representations of the polarization asymmetry in the isovector part of u-channel $\gamma p \to \pi^+ n$, as determined by 4.0 GeV $\pi^- p \to \rho^o n$ data. The ratio ρ_{1-1}/ρ_{11} is measured in the transversality system of ρ^o's (Ref. 34).

29. (a) u-channel differential cross section of 4.16 - 5.23 GeV $\gamma p \rightarrow \pi^+ n$ (Ref. 32) data, energy extrapolated to 4.0 GeV. (b) Percentage contributions in the cross section of u-channel $\gamma p \rightarrow \pi^+ n$ at 4.0 GeV of amounts due to Δ-exchange, N-exchange (N_α and N_γ) and their interference, as parameterized in Regge pole fit from Ref. 35.

30. (a) VMD prediction, on the isovector part of u-channel $\gamma p \rightarrow \pi^+ n$ by photons linearly polarized perpendicular to the production plane, at 4.0 GeV. (b) Behavior in the isovector part of u-channel $\gamma p \rightarrow \pi^+ n$ by unpolarized photons at 4.0 GeV from VMD application to transversely polarized ρ^o's in $\pi^- p \rightarrow \rho^o n$ (Ref. 34). The solid curve is abstracted from the isovector part of Δ, N_α and N_γ Regge pole fits (Ref. 35) to $\gamma p \rightarrow \pi^+ n$ and $\gamma p \rightarrow \pi^o p$ data, using Eq. (13).

31. Compilation of $\sigma_{tot}(\gamma p)$ measurements (Refs. 4, 5, 7) in comparison with a VMD-quark model relation, shown on the figure, using measurements of $\pi^+ p$ and $\pi^- p$ total cross sections.

32. Relative comparison of two-body photoproduction channels' differential cross sections.

33. Measurements of $\gamma p \rightarrow \pi^- \Delta^{++}$ differential cross sections at the indicated photon energies (Ref. 38), in comparison with the behavior in $\gamma p \rightarrow \pi^+ n$ (dashed lines).

34. Δ-photoproduction differential cross sections at 16 GeV. The γn values are obtained from deuterium and hydrogen target subtractions (Ref. 39).

35. The deuterium to hydrogen ratio in Δ-photoproduction at 16 GeV (Ref. 39). The lines indicate expected behavior in isospin 1 exchange for these processes.

36. Behavior of the π^- to π^+ ratio in Δ-photoproduction at 16 GeV (Ref. 39). The solid line, shows for comparison, the π^- to π^+ ratio in single pion photoproduction.

37. The average of Δ^- and Δ^{++} photoproduction differential cross sections (Ref. 39). Cross points are VMD predictions from $\pi^+ p \rightarrow \rho^o \Delta^{++}$ data (Ref. 41), neglecting s-to-u channel crossing effects. The smooth curve is the VMD prediction from the same data, taking into consideration interference effects in such channel crossings (Ref. 40).

38. The momentum transfer dependence of $Z_{eff} = \sigma(\gamma A \rightarrow \pi^+ A^*)/\sigma(\gamma p \rightarrow \pi^+ n)$ at 8 and 16 GeV, in comparison with the Fermi gas model with a 260 MeV/c cutoff (Ref. 46).

39. Predicted energy dependence of Z_{eff} as a function of target elements according to a two-step absorption process (Ref. 43a).

40. Measurement of the Z-dependence of Z_{eff} at 8 and 16 GeV and the indicated momentum transfer values (Ref. 46). The curves are calculated according to Ref. 43a and normalized at each t-value to the carbon data.

41. Behavior of the A-dependence of $[\sigma(\gamma A \rightarrow \pi^- A^*)/N]/[\sigma(\gamma A \rightarrow \pi^+ A^*)/Z]$ where N and Z are the neutron and proton numbers in a nucleus (Ref. 46).

42. Measurements of the ratio $\sigma_{tot}(\gamma A)/A\,\sigma_{tot}(\gamma p)$ (Ref. 5), in comparison with an optical model calculation (Ref. 43c) for the given values of $\sigma_{tot}(\rho^o p)$.

43. Measurements of the ratio $\sigma_{tot}(\gamma A)/\sigma_{tot}(\gamma p)$ (Ref. 5). The solid line is the expected behavior if photoabsorption proceeds entirely by nuclear volume effects.

44. Single and two-step amplitudes, M_1 and M_2, representing several nuclear photoabsorption processes. $M_i(\text{VMD})$ are the VMD amplitudes neglecting q^2 dependences; these effects are considered by the factors C_{ik}, discussed in Ref. 44.

45. Isobar electroproduction cross sections normalized by ep elastic scattering cross sections at the same q^2 values (Ref. 51). The curves are from a relativistic gauge-invariant model (Ref. 55).

46. Inelastic ep scattering cross sections as a function of the final state hadronic mass W, at $\theta = 6^{\circ}$ and E = 10 GeV; (a) before and (b) after radiative corrections. In (a) the elastic ep scattering peak is shown, reduced by a factor of 6 and the dashed curve represents the radiative tail due to elastic scattering; (c) the cross-sectional ratio radiatively corrected to that uncorrected (Refs. 50 and 54).

47. Radiatively corrected, inelastic ep scattering cross sections as a function of W, at the indicated laboratory scattering angles and incident electron energies, covering the q^2 range of (a) $0.2 \leq q^2 \leq 0.5$, (b) $0.7 \leq q^2 \leq 2.6$ and (c) $1.6 \leq q^2 \leq 7.3$ $(GeV/c)^2$ (Ref. 50).

48. Inelastic ep scattering cross sections at E = 13.51 GeV and $\theta = 6^{\circ}$ ($0.7 \leq q^2 \leq 2.6$ $(GeV/c)^2$) (Ref. 50), in comparison with VMD predictions of Ref. 52.

49. Inelastic ep scattering cross sections at E = 17.65 GeV and $\theta = 10$ ($1.6 \leq q^2 \leq 7.3$ $(GeV/c)^2$) (Ref. 50). The curve drawn is the VMD prediction from Ref. 52.

50. The functional behavior of νW_2 vs. the scaling variable $\omega = 2M\nu/q^2$ at $\theta = 6^{\circ}$ (Ref. 51). (a) For $q^2 > 0.5$ $(GeV/c)^2$ and assuming $R = \sigma_L/\sigma_T = 0$; (c) assuming $R = \infty$; (e) for $q^2 \leq 0.5$ $(GeV/c)^2$.

51. The behavior of νW_2 as a function of ω at $\theta = 10^{\circ}$ and $q^2 > 0.5$ $(GeV/c)^2$ (Ref. 51); (b) assuming R = 0 and (d) for $R = \infty$.

52. Examination of q^2 dependence in the VMD parameter $\xi(K)$, the vector-meson-nucleon cross-sectional polarization ratio at ep deep inelastic scattering regions (Ref. 51).

53. $(d^2\sigma/dE'd\Omega)/(d\sigma/d\Omega)_{Mott}$ q^2 dependence for fixed W values. The curves drawn through the ep inelastic scattering data are merely to guide the eye.

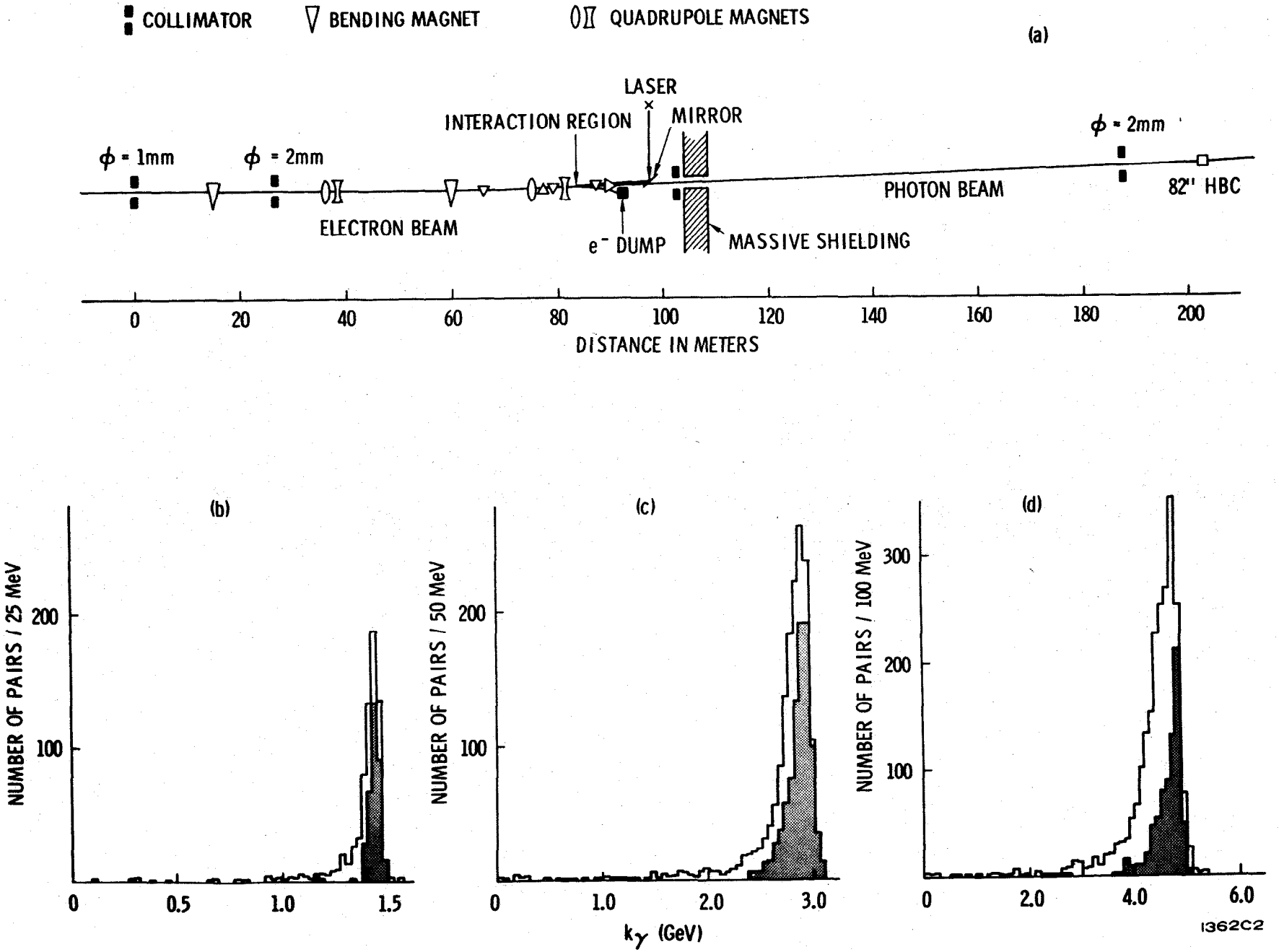
COLLIMATOR
BENDING MAGNET
QUADRUPOLE MAGNETS
(a)
LASER
INTERACTION REGION
MIRROR
ϕ = 1mm
ϕ = 2mm
ϕ = 2mm
PHOTON BEAM
82" HBC
ELECTRON BEAM
e⁻ DUMP
MASSIVE SHIELDING
0
20
40
60
80
100
120
140
160
180
200
DISTANCE IN METERS
(b)
NUMBER OF PAIRS / 25 MeV
200
100
0
0.5
1.0
1.5
(c)
NUMBER OF PAIRS / 50 MeV
200
100
0
1.0
2.0
3.0
kγ (GeV)
(d)
NUMBER OF PAIRS / 100 MeV
300
200
100
0
2.0
4.0
6.0
1362C2

Fig. 1

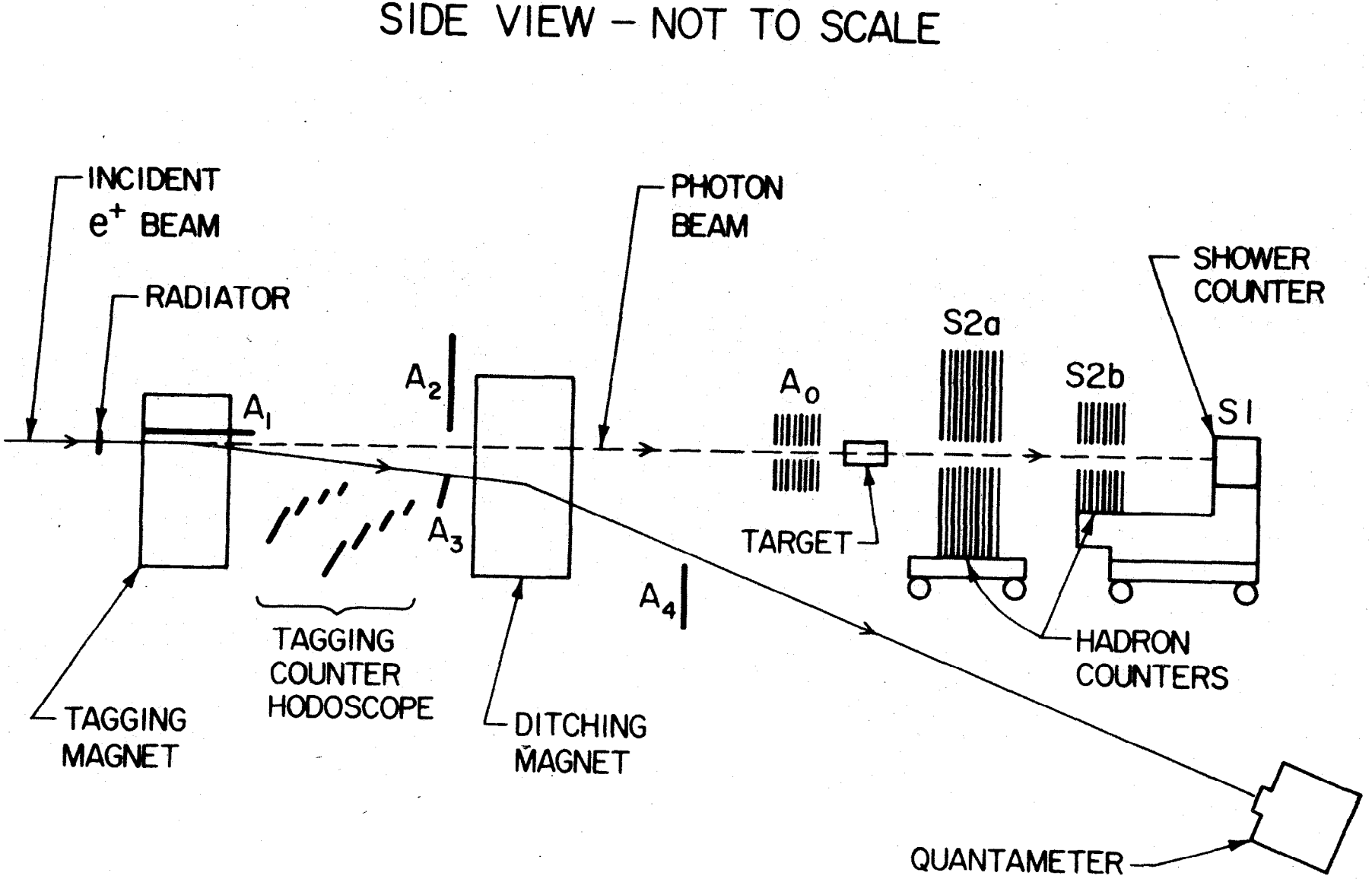
SIDE VIEW – NOT TO SCALE
INCIDENT
e+ BEAM
RADIATOR
PHOTON
BEAM
SHOWER
COUNTER
S2a
S2b
S1
A1
A2
A0
A3
A4
TARGET
TAGGING
COUNTER
HODOSCOPE
TAGGING
MAGNET
DITCHING
MAGNET
HADRON
COUNTERS
QUANTAMETER

Fig. 2

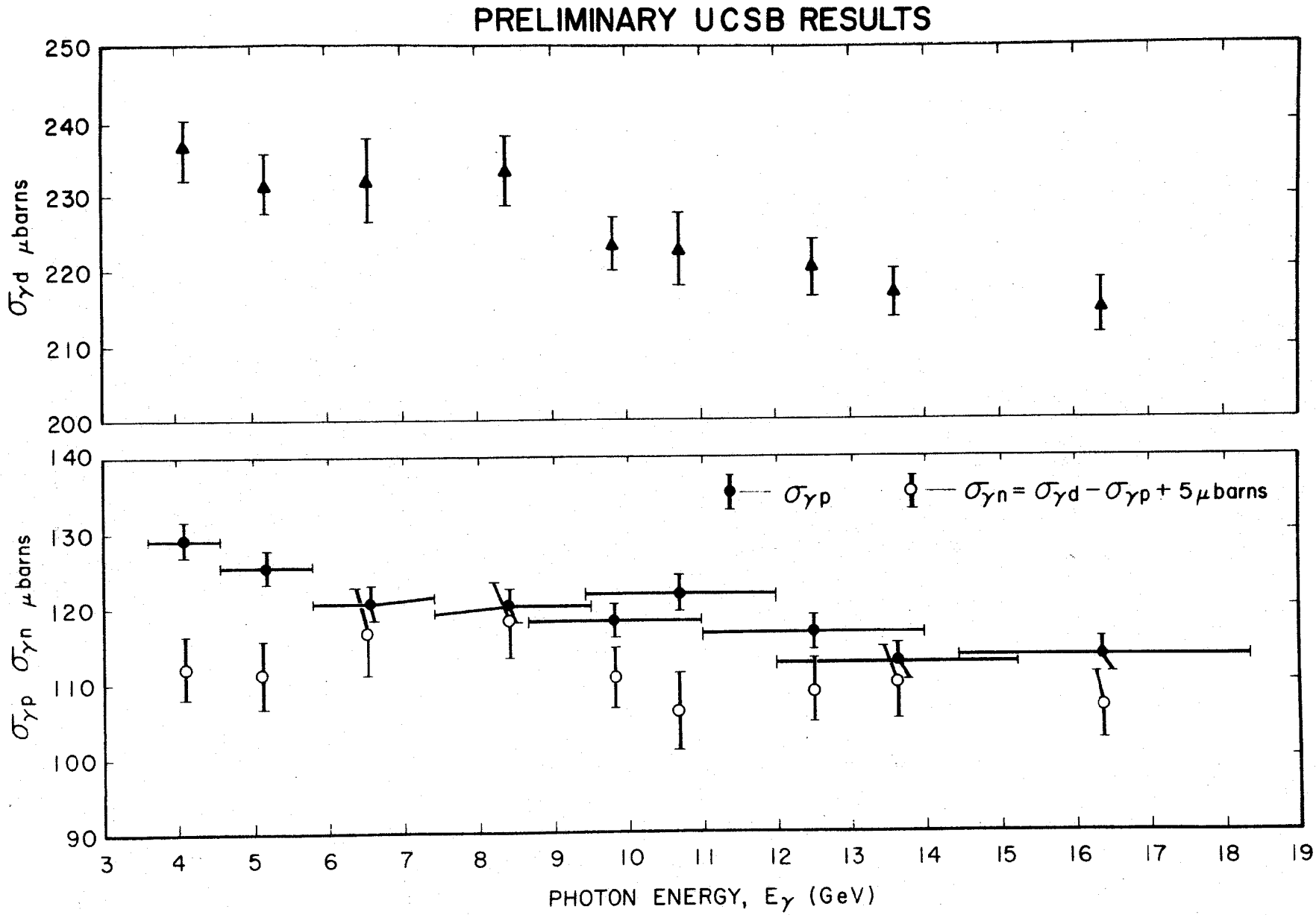
PRELIMINARY UCSB RESULTS
250
240
230
220
210
200
$\sigma_{\gamma d}$ μbarns
140
130
120
110
100
90
$\sigma_{\gamma p}$ $\sigma_{\gamma n}$ μbarns
$\sigma_{\gamma p}$
$\sigma_{\gamma n} = \sigma_{\gamma d} - \sigma_{\gamma p} + 5\,\mu$barns
3
4
5
6
7
8
9
10
11
12
13
14
15
16
17
18
19
PHOTON ENERGY, E_γ (GeV)

Fig. 3

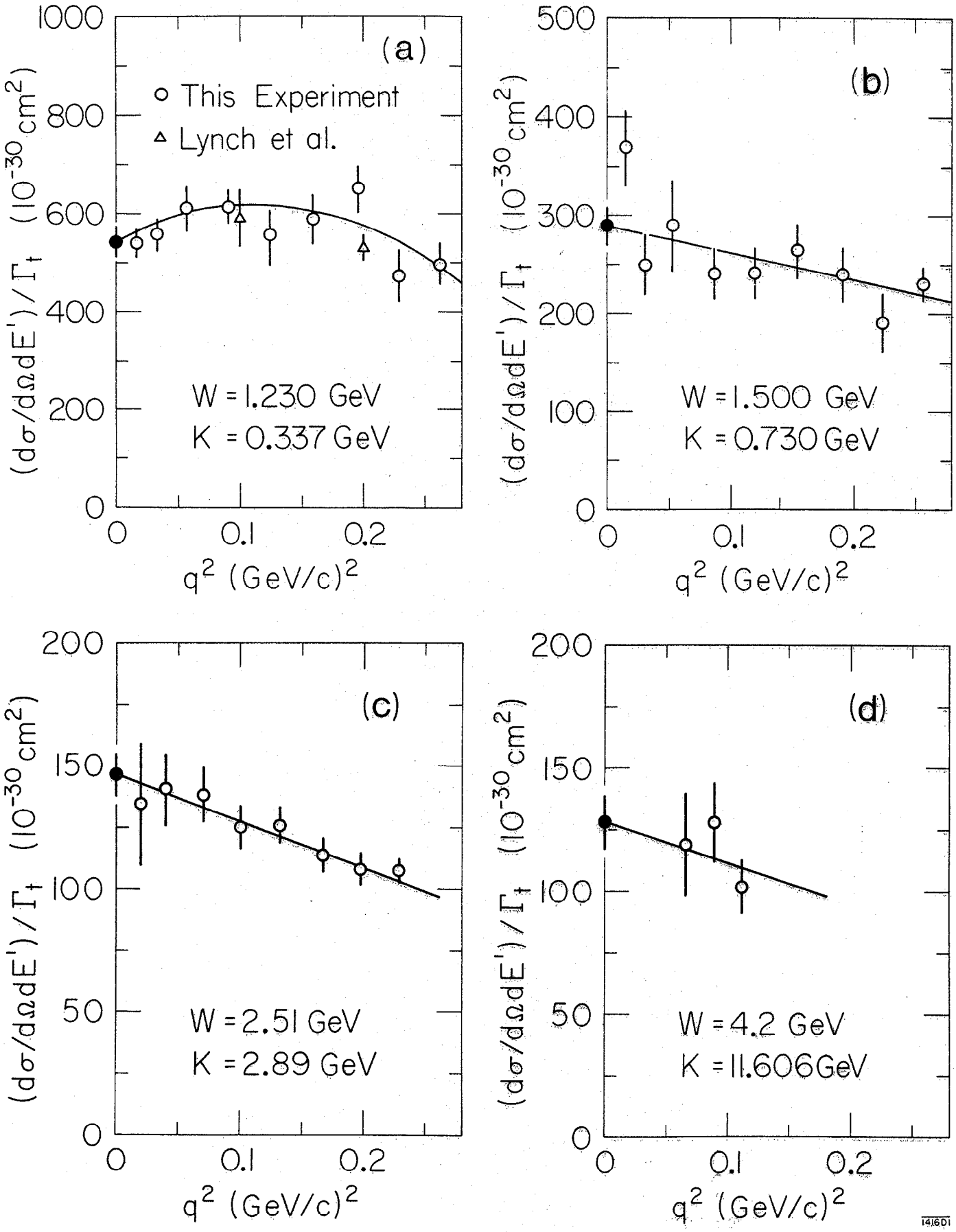
(a)
This Experiment
Lynch et al.
W = 1.230 GeV
K = 0.337 GeV
(b)
W = 1.500 GeV
K = 0.730 GeV
(c)
W = 2.51 GeV
K = 2.89 GeV
(d)
W = 4.2 GeV
K = 11.606 GeV
$(d\sigma/d\Omega dE')/\Gamma_t$ $(10^{-30}cm^2)$
q^2 (GeV/c)^2
14160 1

Fig. 4

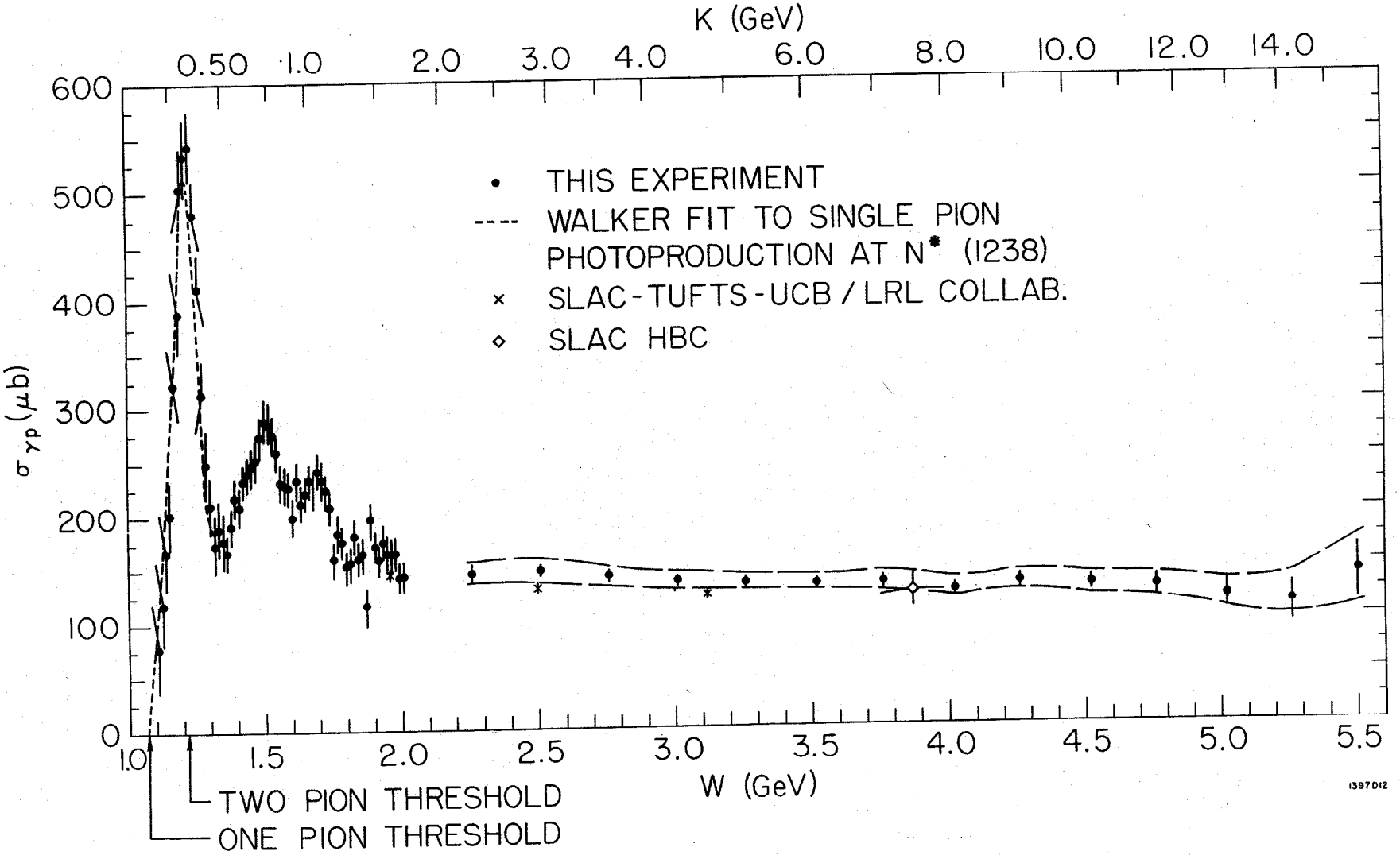
K (GeV)
0.50
1.0
2.0
3.0
4.0
6.0
8.0
10.0
12.0
14.0
600
500
400
300
200
100
0
$\sigma_{\gamma p}$ (μb)
THIS EXPERIMENT
WALKER FIT TO SINGLE PION PHOTOPRODUCTION AT N* (1238)
SLAC-TUFTS-UCB / LRL COLLAB.
SLAC HBC
1.0
1.5
2.0
2.5
3.0
3.5
4.0
4.5
5.0
5.5
W (GeV)
TWO PION THRESHOLD
ONE PION THRESHOLD
1397012

Fig. 5

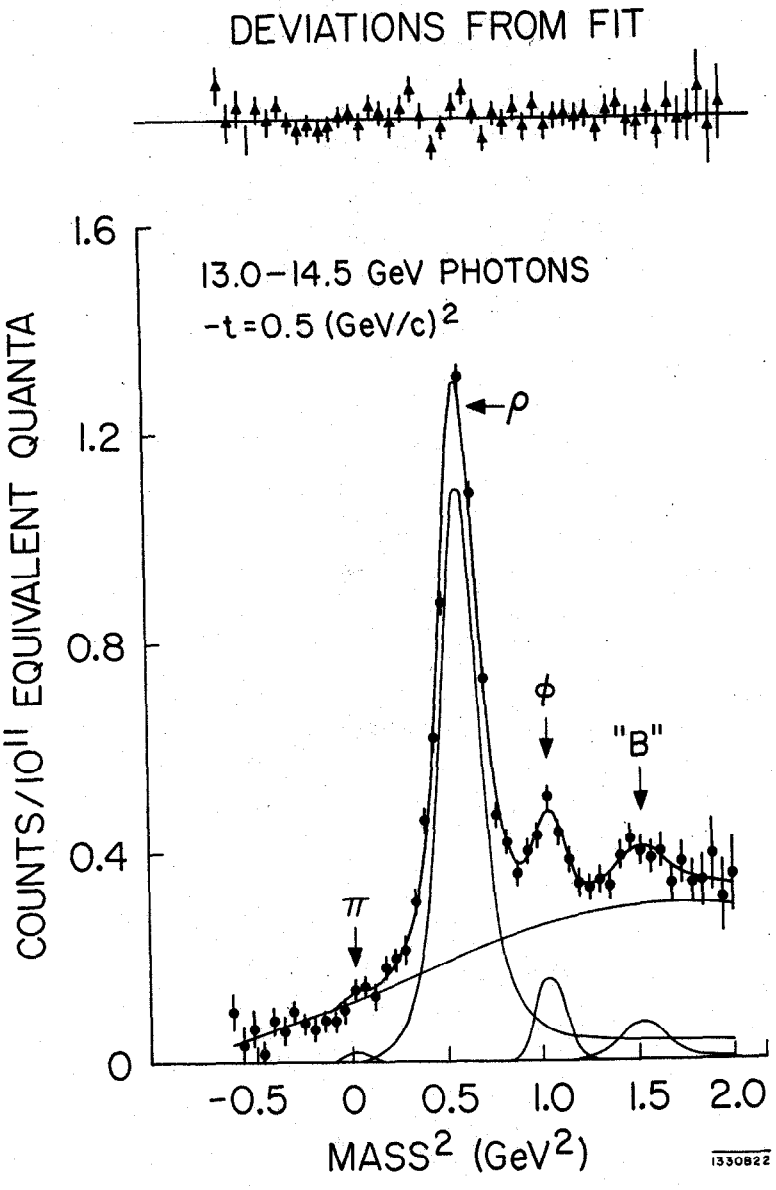
DEVIATIONS FROM FIT
13.0–14.5 GeV PHOTONS
-t=0.5 (GeV/c)²
ρ
φ
"B"
π
COUNTS/10¹¹ EQUIVALENT QUANTA
1.6
1.2
0.8
0.4
0
-0.5
0
0.5
1.0
1.5
2.0
MASS² (GeV²)
1330822

Fig. 6

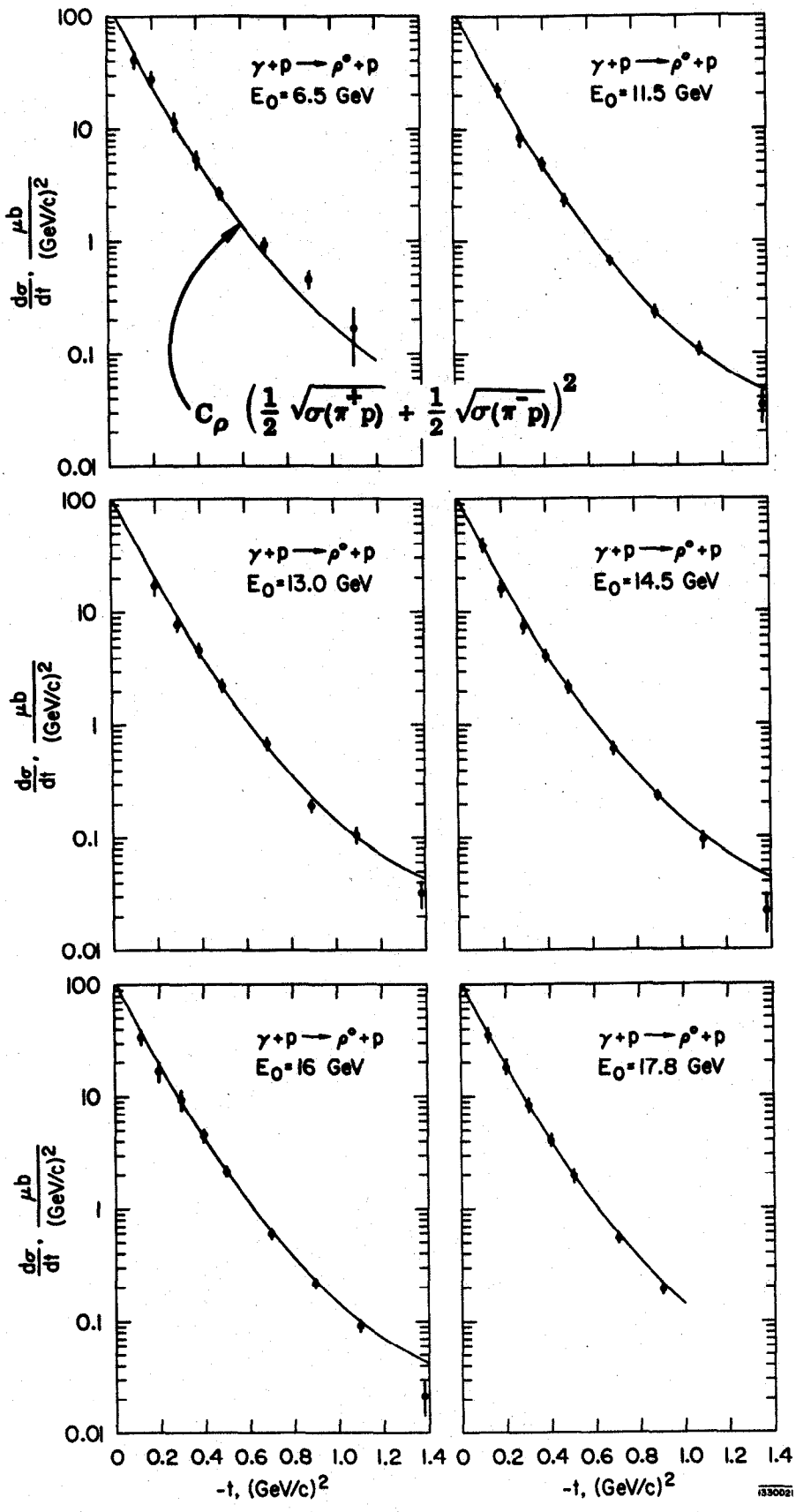
γ+p → ρ°+p
E0 = 6.5 GeV
γ+p → ρ°+p
E0 = 11.5 GeV
γ+p → ρ°+p
E0 = 13.0 GeV
γ+p → ρ°+p
E0 = 14.5 GeV
γ+p → ρ°+p
E0 = 16 GeV
γ+p → ρ°+p
E0 = 17.8 GeV
dσ/dt, μb/(GeV/c)²
100
10
1
0.1
0.01
$C_\rho \left(\frac{1}{2}\sqrt{\sigma(\pi^+ p)} + \frac{1}{2}\sqrt{\sigma(\pi^- p)}\right)^2$
0 0.2 0.4 0.6 0.8 1.0 1.2 1.4
-t, (GeV/c)²
133021

Fig. 7

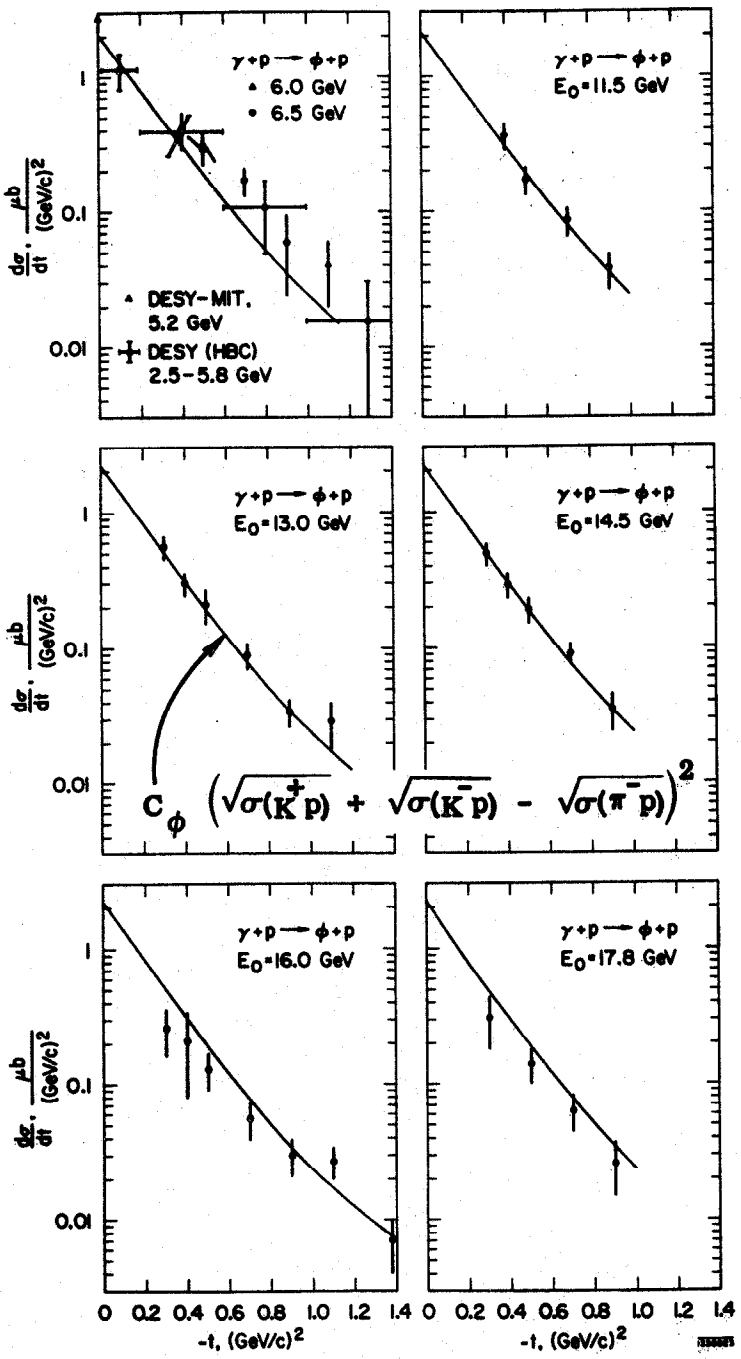
γ+p → φ+p
▲ 6.0 GeV
• 6.5 GeV
▲ DESY-MIT, 5.2 GeV
DESY (HBC) 2.5-5.8 GeV
γ+p → φ+p
E0=11.5 GeV
γ+p → φ+p
E0=13.0 GeV
γ+p → φ+p
E0=14.5 GeV
γ+p → φ+p
E0=16.0 GeV
γ+p → φ+p
E0=17.8 GeV
dσ/dt, μb/(GeV/c)²
1
0.1
0.01
0 0.2 0.4 0.6 0.8 1.0 1.2 1.4
-t, (GeV/c)²
$C_\phi \left(\sqrt{\sigma(K^+p)} + \sqrt{\sigma(K^-p)} - \sqrt{\sigma(\pi^-p)}\right)^2$

Fig. 8

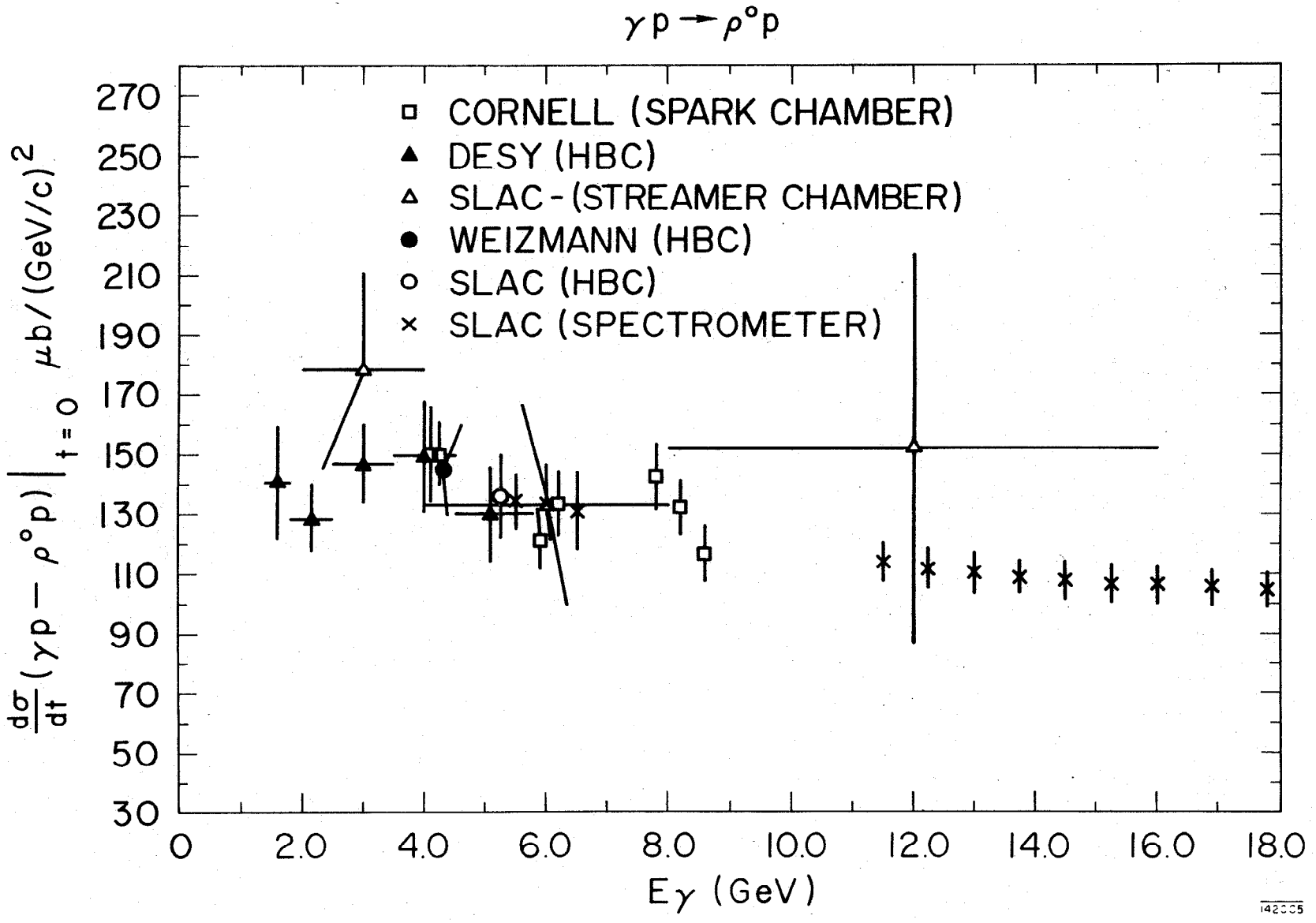
γp → ρ°p
CORNELL (SPARK CHAMBER)
DESY (HBC)
SLAC - (STREAMER CHAMBER)
WEIZMANN (HBC)
SLAC (HBC)
SLAC (SPECTROMETER)
dσ/dt (γp → ρ°p)|t=0 μb/(GeV/c)²
270
250
230
210
190
170
150
130
110
90
70
50
30
0
2.0
4.0
6.0
8.0
10.0
12.0
14.0
16.0
18.0
Eγ (GeV)
142005

Fig. 9

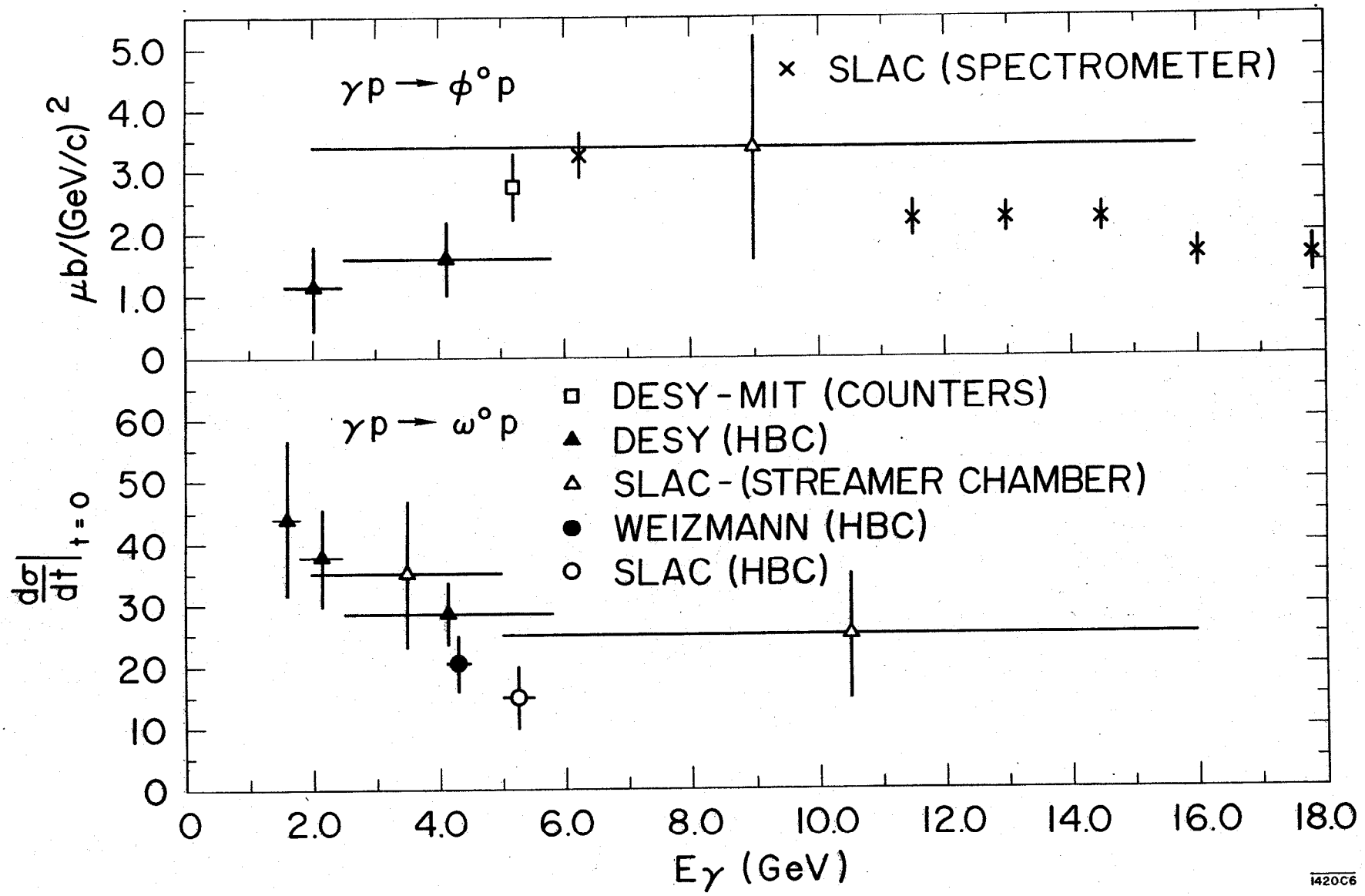
$\gamma p \rightarrow \phi^\circ p$
× SLAC (SPECTROMETER)
$\mu b/(GeV/c)^2$
5.0
4.0
3.0
2.0
1.0
0
$\gamma p \rightarrow \omega^\circ p$
□ DESY-MIT (COUNTERS)
▲ DESY (HBC)
△ SLAC-(STREAMER CHAMBER)
● WEIZMANN (HBC)
○ SLAC (HBC)
$\frac{d\sigma}{dt}\Big|_{t=0}$
60
50
40
30
20
10
0
0
2.0
4.0
6.0
8.0
10.0
12.0
14.0
16.0
18.0
$E\gamma$ (GeV)
1420C6

Fig. 10

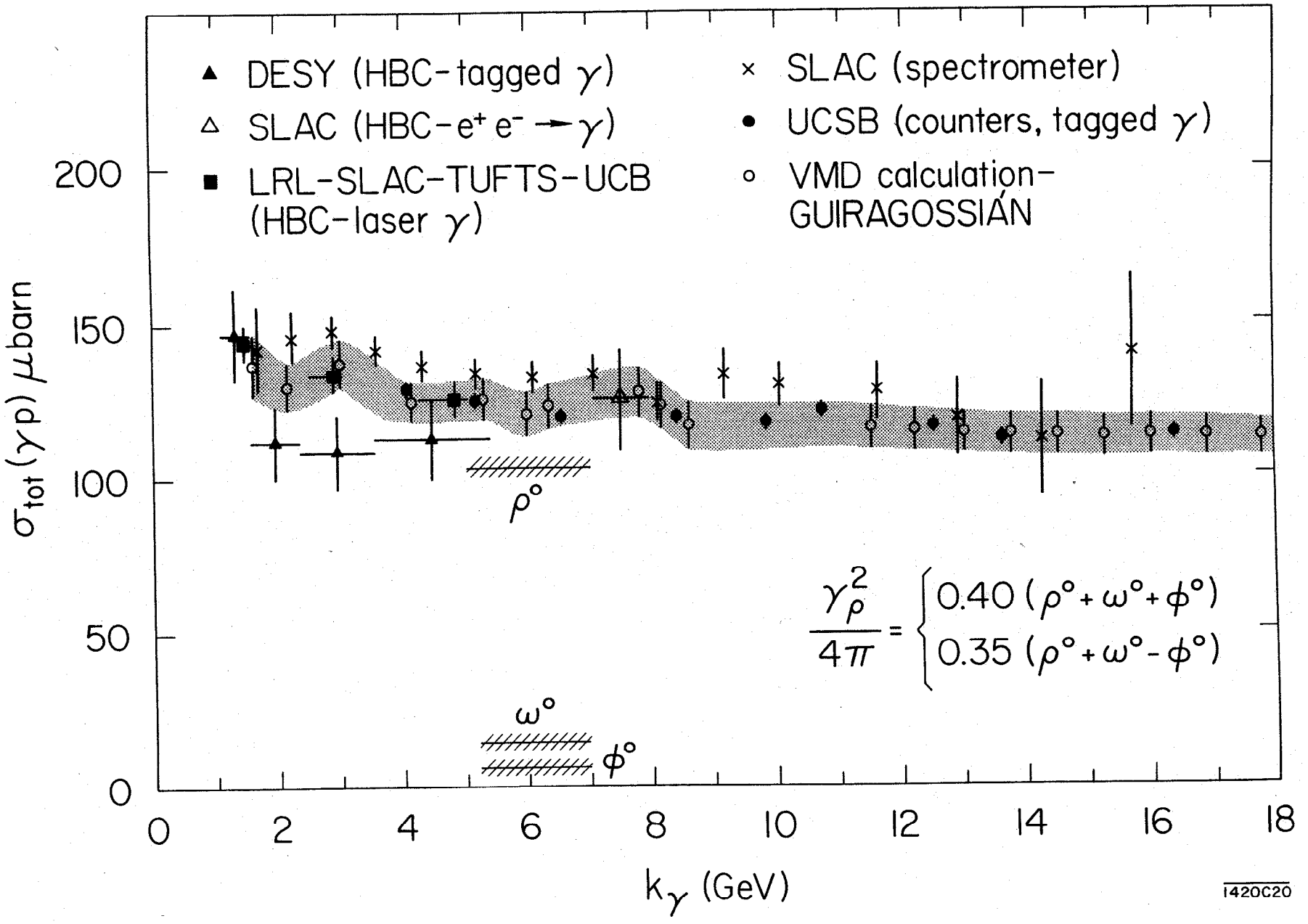
▲ DESY (HBC-tagged γ)
△ SLAC (HBC-e⁺e⁻ → γ)
■ LRL-SLAC-TUFTS-UCB (HBC-laser γ)
× SLAC (spectrometer)
● UCSB (counters, tagged γ)
○ VMD calculation-GUIRAGOSSIÁN
σtot (γp) μbarn
200
150
100
50
0
ρ°
ω°
φ°
γ²ρ/4π = 0.40 (ρ° + ω° + φ°)
0.35 (ρ° + ω° - φ°)
0
2
4
6
8
10
12
14
16
18
kγ (GeV)
1420C20

Fig. 11

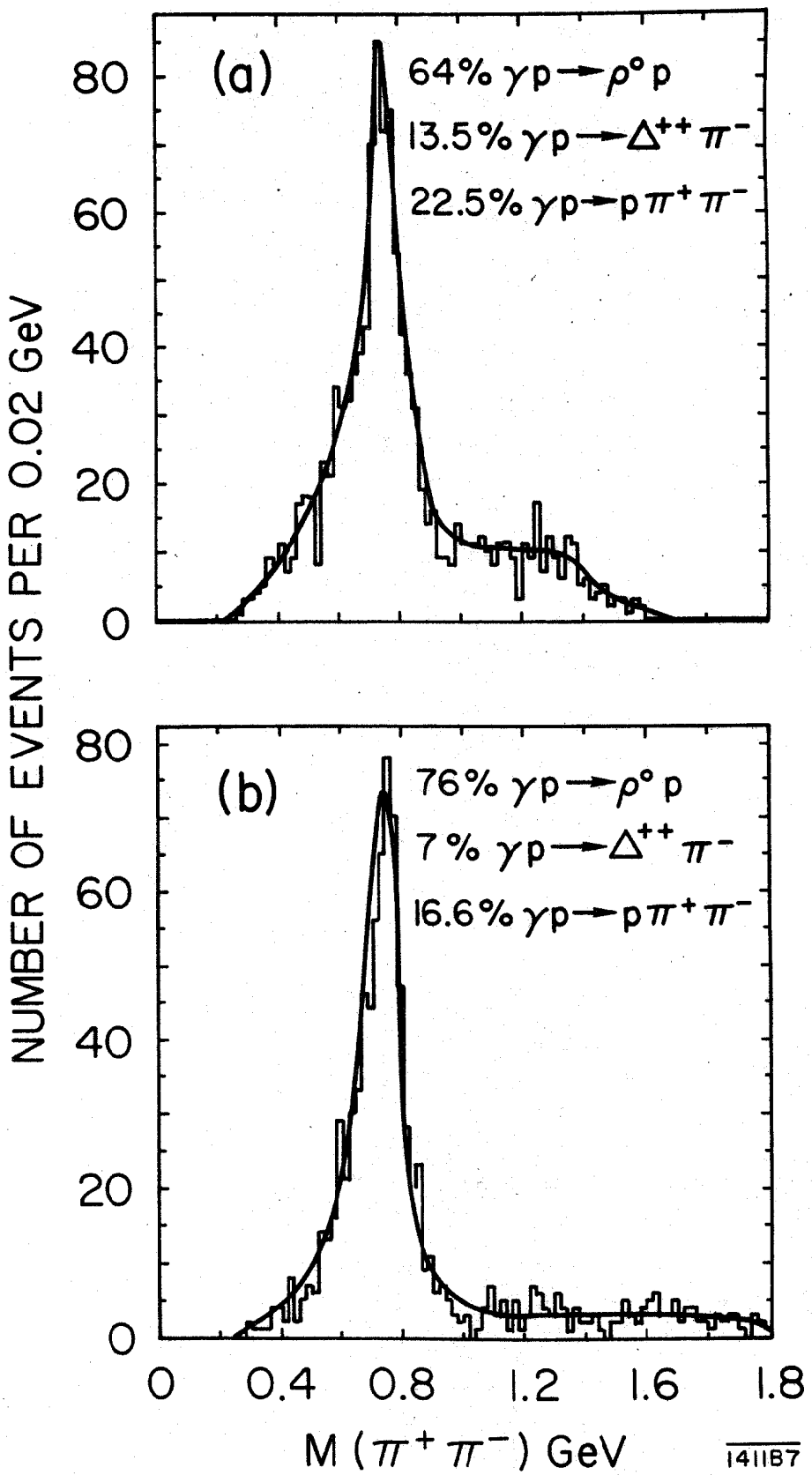
(a)
64% γp → ρ°p
13.5% γp → Δ++π−
22.5% γp → pπ+π−
(b)
76% γp → ρ°p
7% γp → Δ++π−
16.6% γp → pπ+π−
NUMBER OF EVENTS PER 0.02 GeV
0
20
40
60
80
0
0.4
0.8
1.2
1.6
1.8
M (π+π−) GeV
141187

Fig. 12

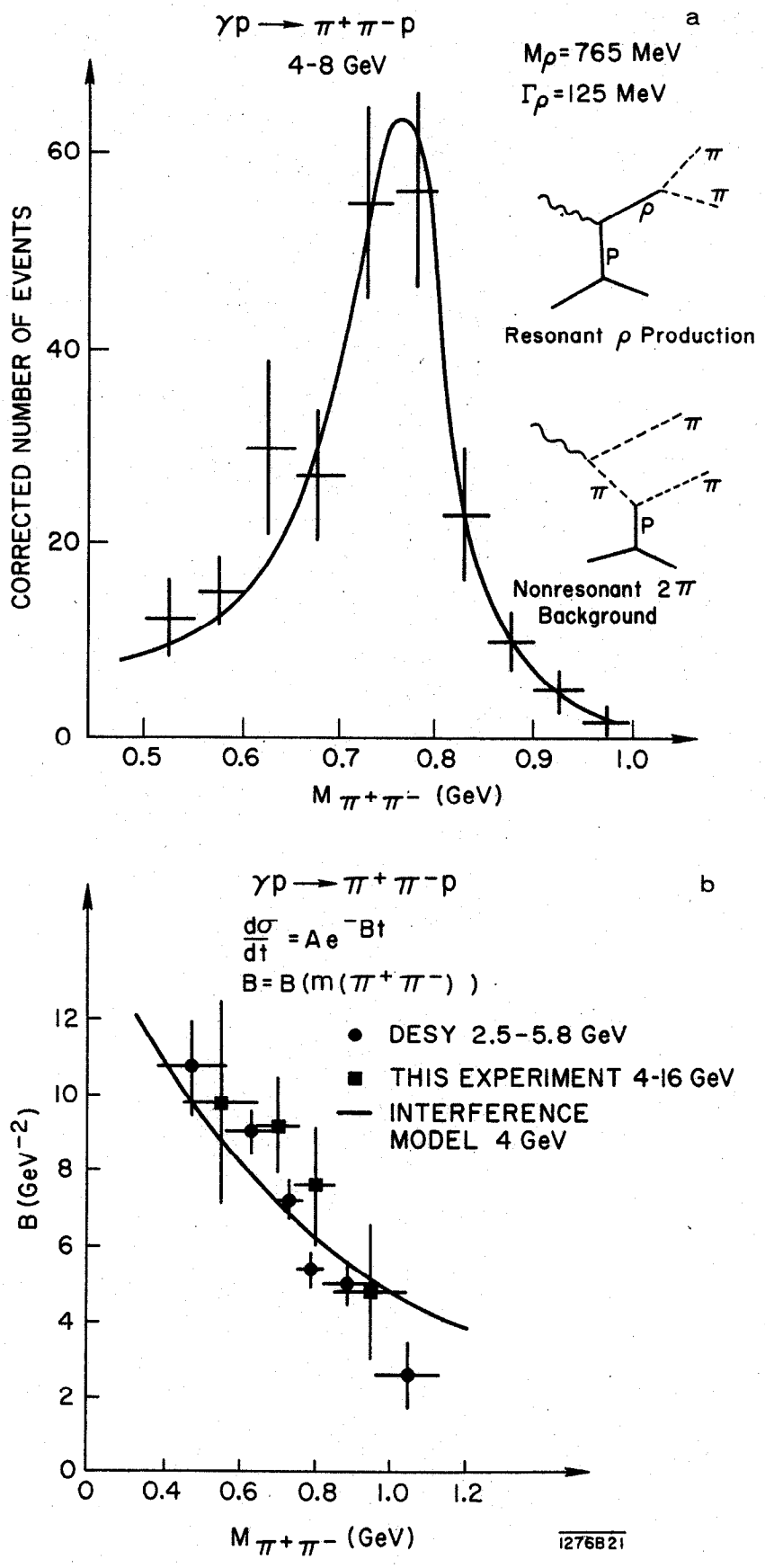
γp → π+π−p
4-8 GeV
a
Mρ=765 MeV
Γρ=125 MeV
π
π
ρ
P
Resonant ρ Production
π
π
π
P
Nonresonant 2π
Background
CORRECTED NUMBER OF EVENTS
0
20
40
60
0.5
0.6
0.7
0.8
0.9
1.0
M π+π− (GeV)
γp → π+π−p
b
dσ/dt = A e^−Bt
B = B(m(π+π−))
DESY 2.5-5.8 GeV
THIS EXPERIMENT 4-16 GeV
INTERFERENCE
MODEL 4 GeV
B (GeV^−2)
0
2
4
6
8
10
12
0
0.4
0.6
0.8
1.0
1.2
M π+π− (GeV)
1276B21

Fig. 13

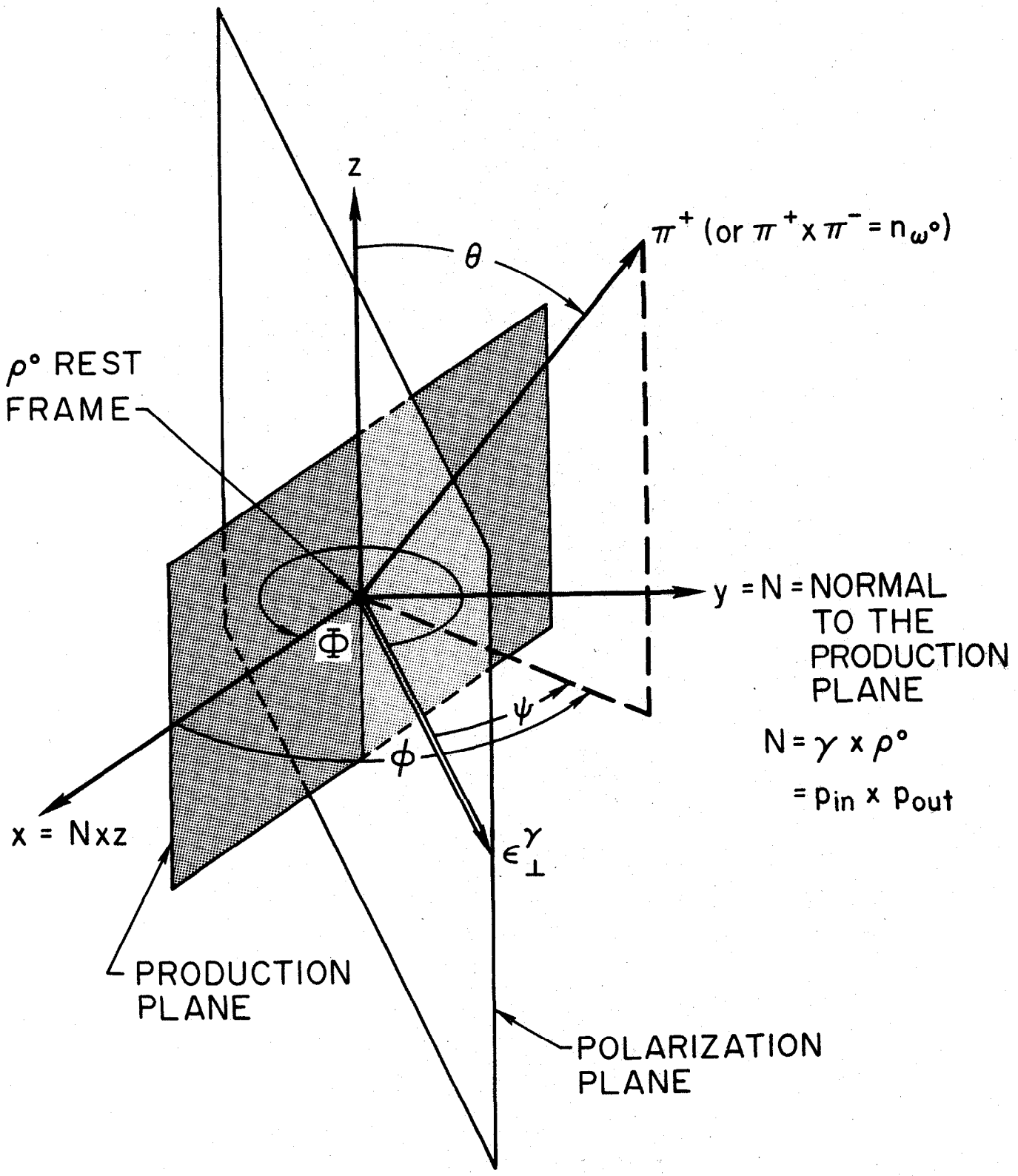

Fig. 14

14111A4

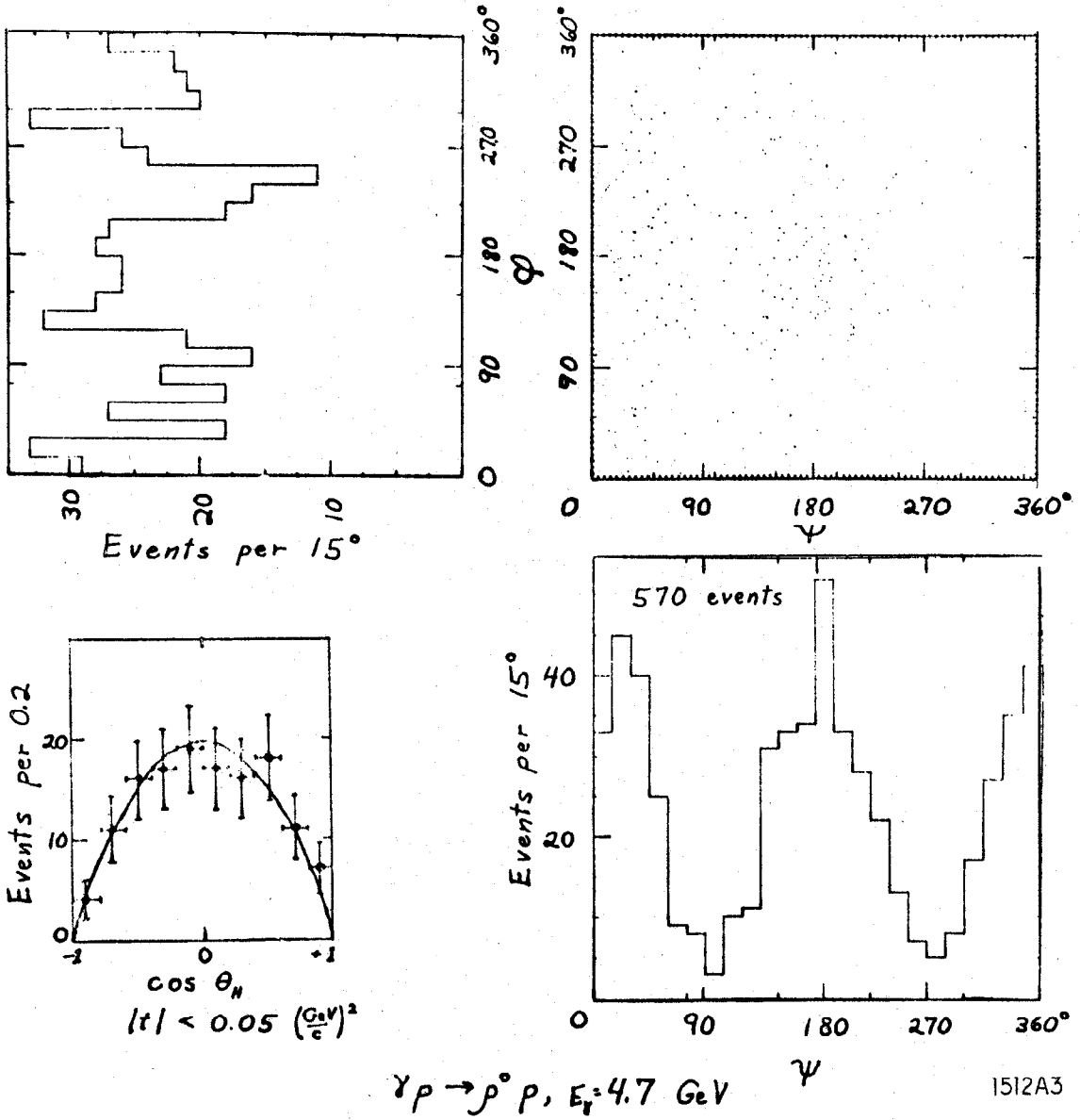
Events per 15°
φ
ψ
570 events
Events per 15°
Events per 0.2
cos θ_H
|t| < 0.05 (GeV/c)²
γp → ρ°p, E_γ = 4.7 GeV
1512A3

Fig. 15

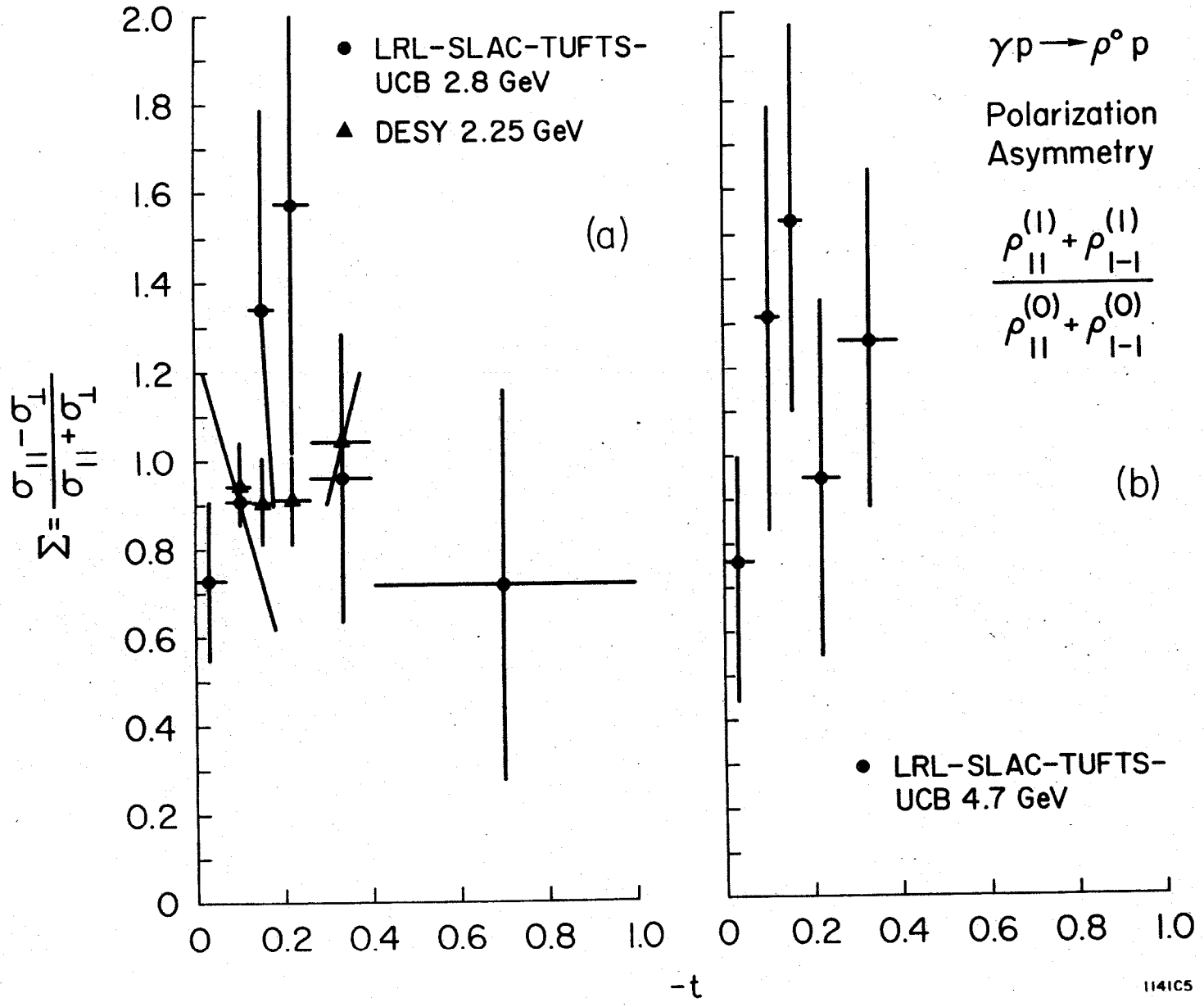
2.0
1.8
1.6
1.4
1.2
1.0
0.8
0.6
0.4
0.2
0
0
0.2
0.4
0.6
0.8
1.0
-t
LRL-SLAC-TUFTS-
UCB 2.8 GeV
DESY 2.25 GeV
(a)
$\gamma p \rightarrow \rho^0 p$
Polarization
Asymmetry
$\frac{\rho_{11}^{(1)} + \rho_{1-1}^{(1)}}{\rho_{11}^{(0)} + \rho_{1-1}^{(0)}}$
(b)
LRL-SLAC-TUFTS-
UCB 4.7 GeV
$\Sigma = \frac{\sigma_T^+ - \sigma_T^-}{\sigma_T^+ + \sigma_T^-}$
1141C5

Fig. 16

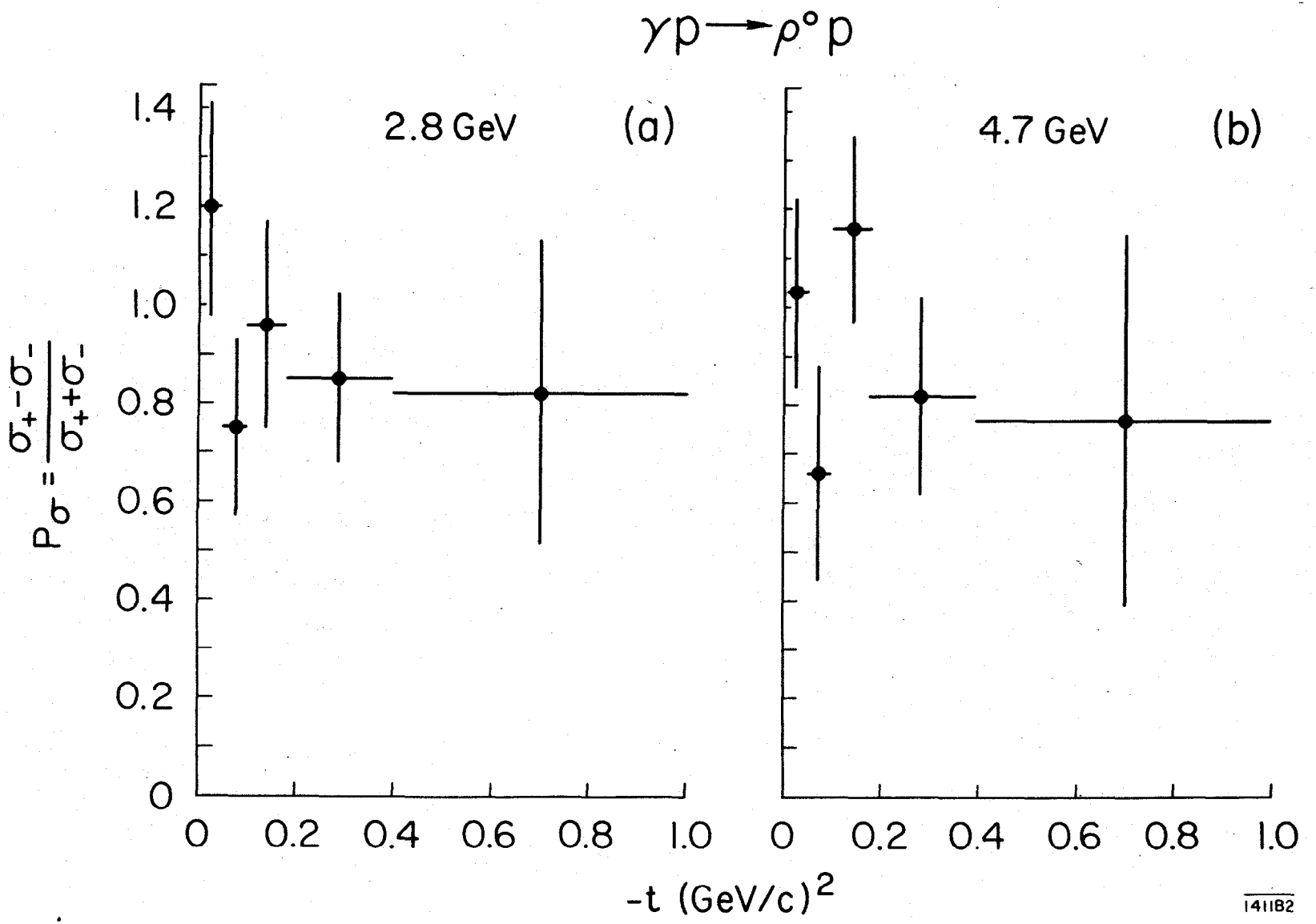
γp → ρ°p
2.8 GeV
(a)
4.7 GeV
(b)
$P_b = \frac{\sigma_+ - \sigma_-}{\sigma_+ + \sigma_-}$
1.4
1.2
1.0
0.8
0.6
0.4
0.2
0
0
0.2
0.4
0.6
0.8
1.0
-t (GeV/c)²
141182

Fig. 17

ϕ (FOLDED) DISTRIBUTION FOR STATISTICAL TENSOR Im T_2^2

(X) QUARK MODEL PREDICTION

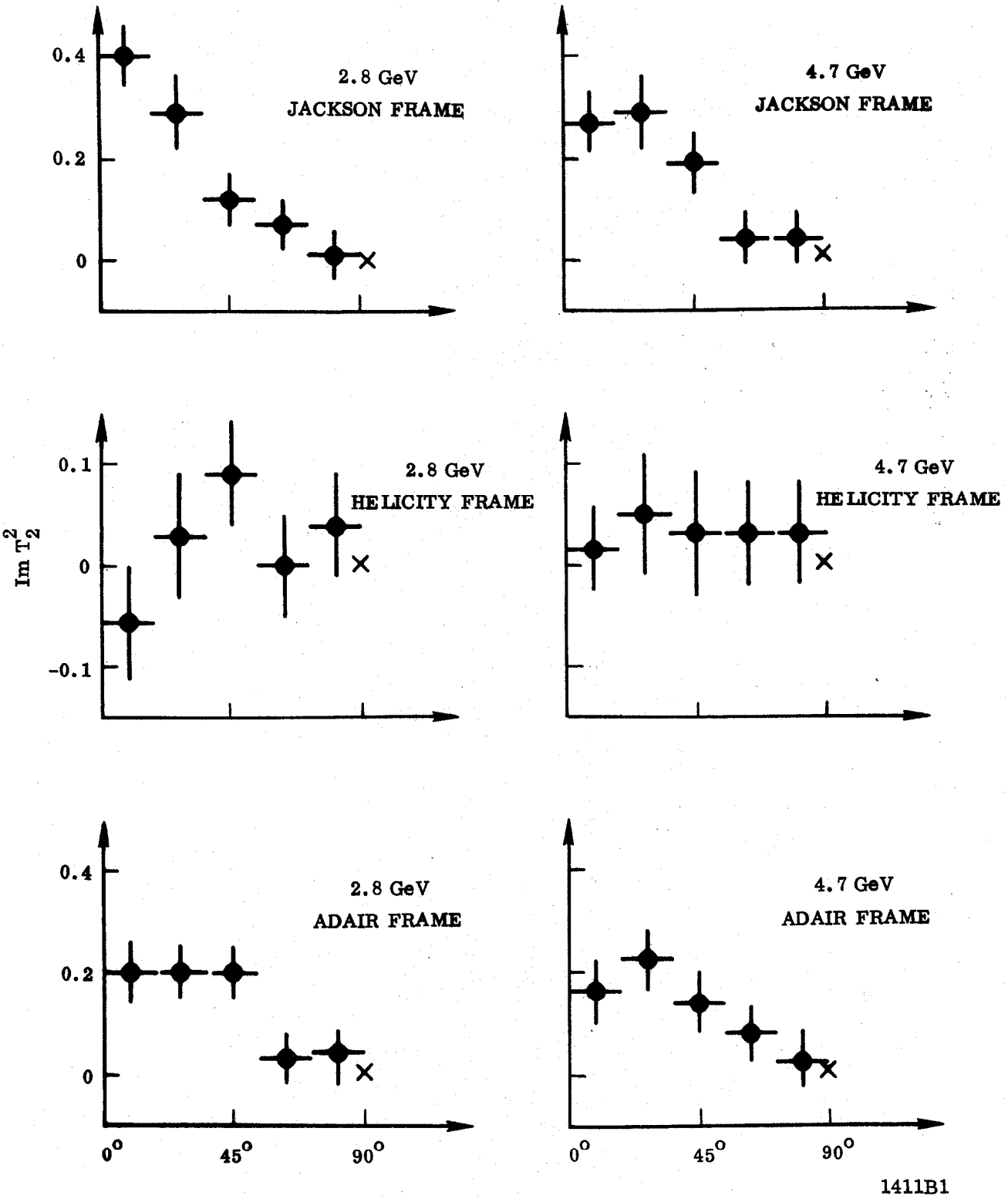

Fig. 18

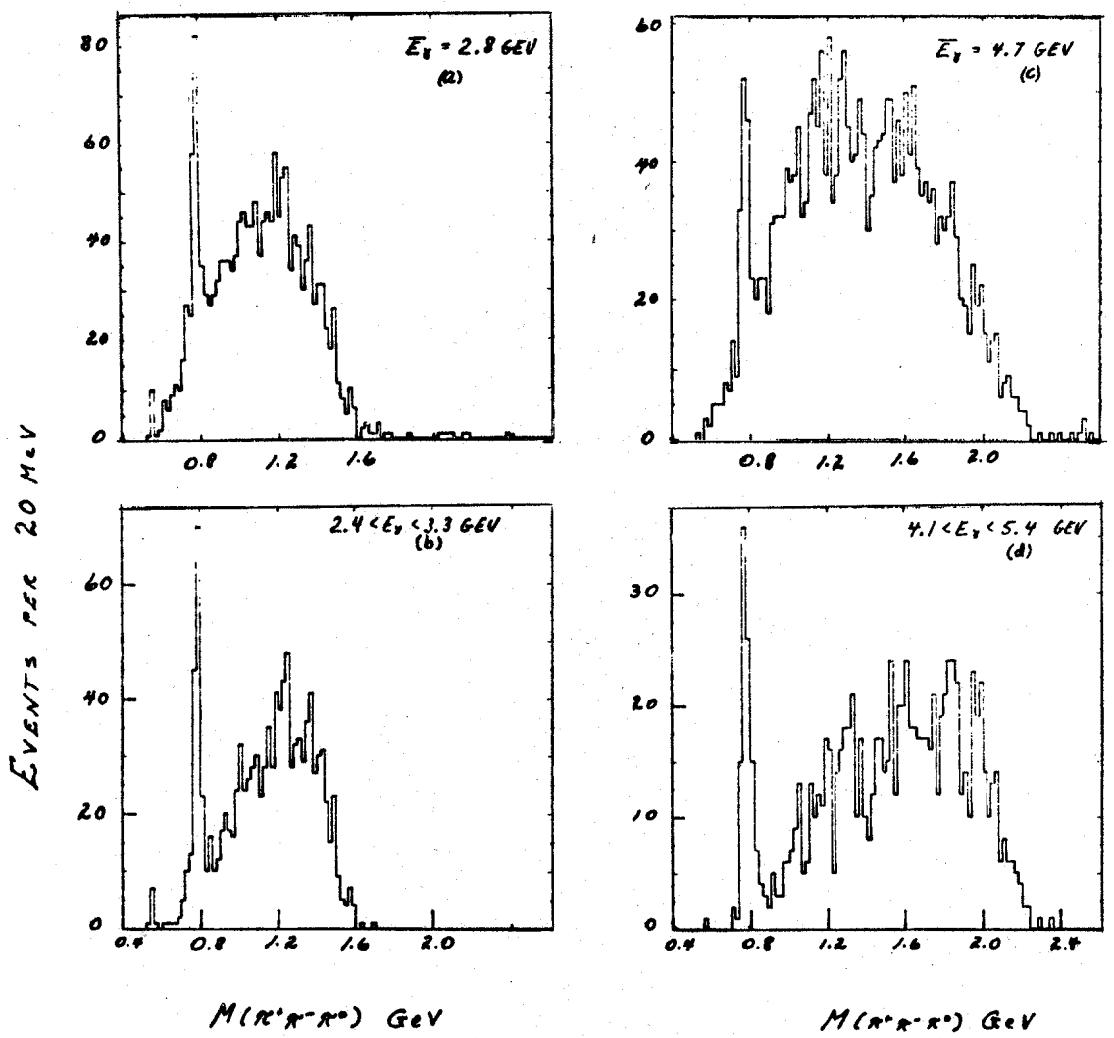
$\bar{E}_\gamma$ = 2.8 GEV
(a)
$\bar{E}_\gamma$ = 4.7 GEV
(c)
2.4 < E_γ < 3.3 GEV
(b)
4.1 < E_γ < 5.4 GEV
(d)
EVENTS PER 20 MeV
M(π⁺π⁻π⁰) GeV
M(π⁺π⁻π⁰) GeV
1512A2

Fig. 19

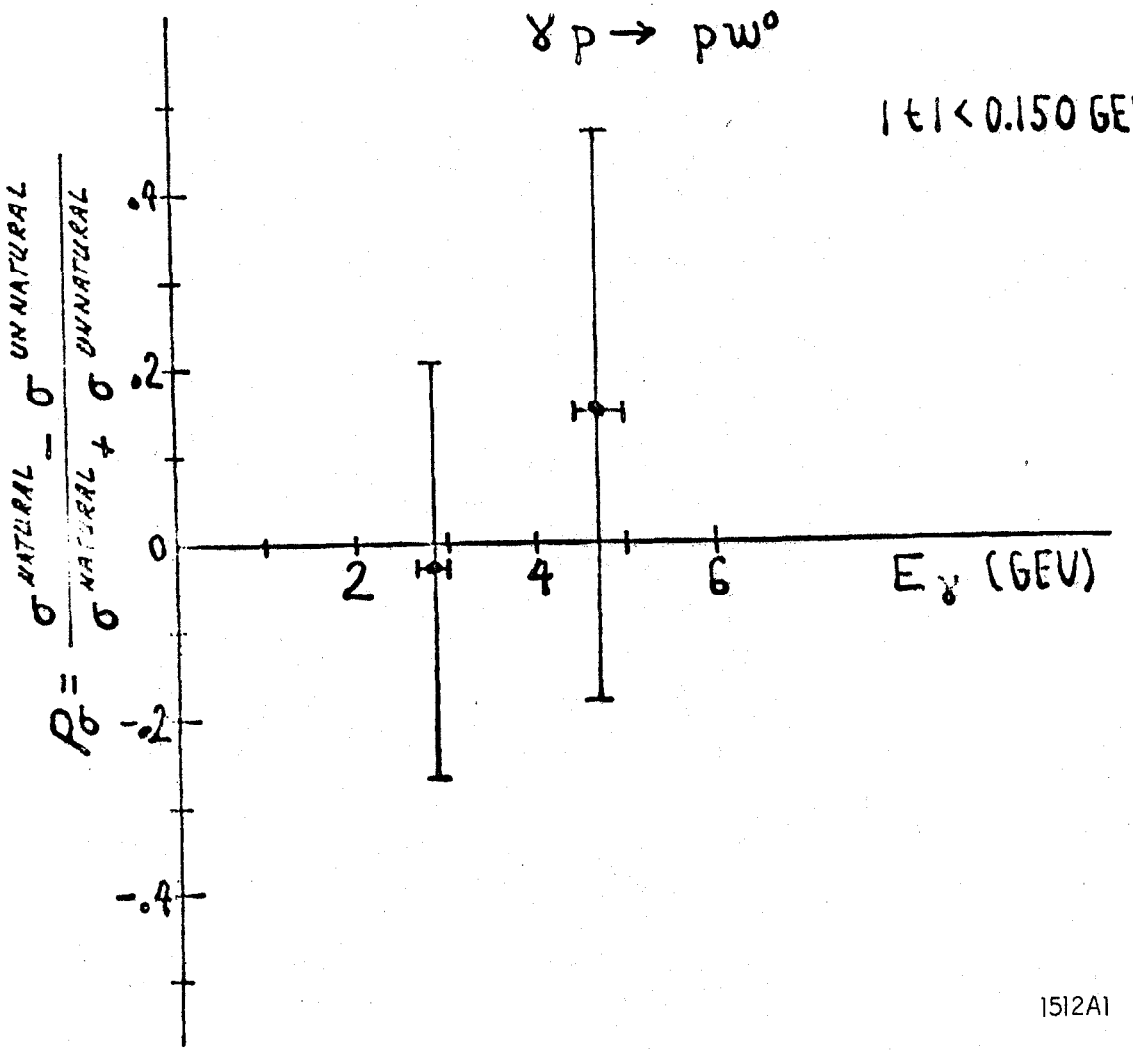
γ p → p ω°
|t| < 0.150 GEV
$\rho_\sigma = \frac{\sigma^{NATURAL} - \sigma^{UNNATURAL}}{\sigma^{NATURAL} + \sigma^{UNNATURAL}}$
.4
.2
0
-.2
-.4
2
4
6
E_γ (GEV)
1512A1

Fig. 20

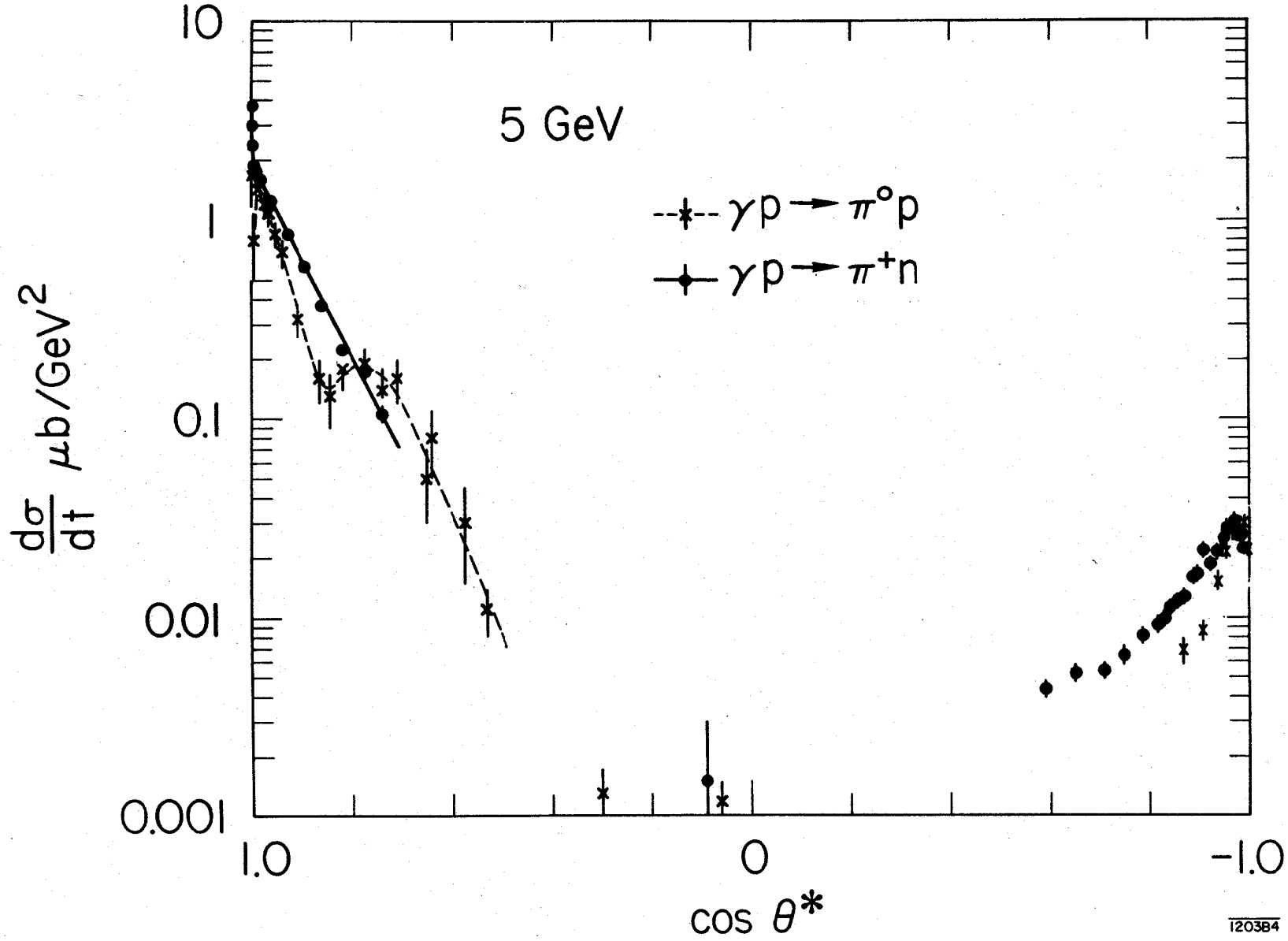

Fig. 21

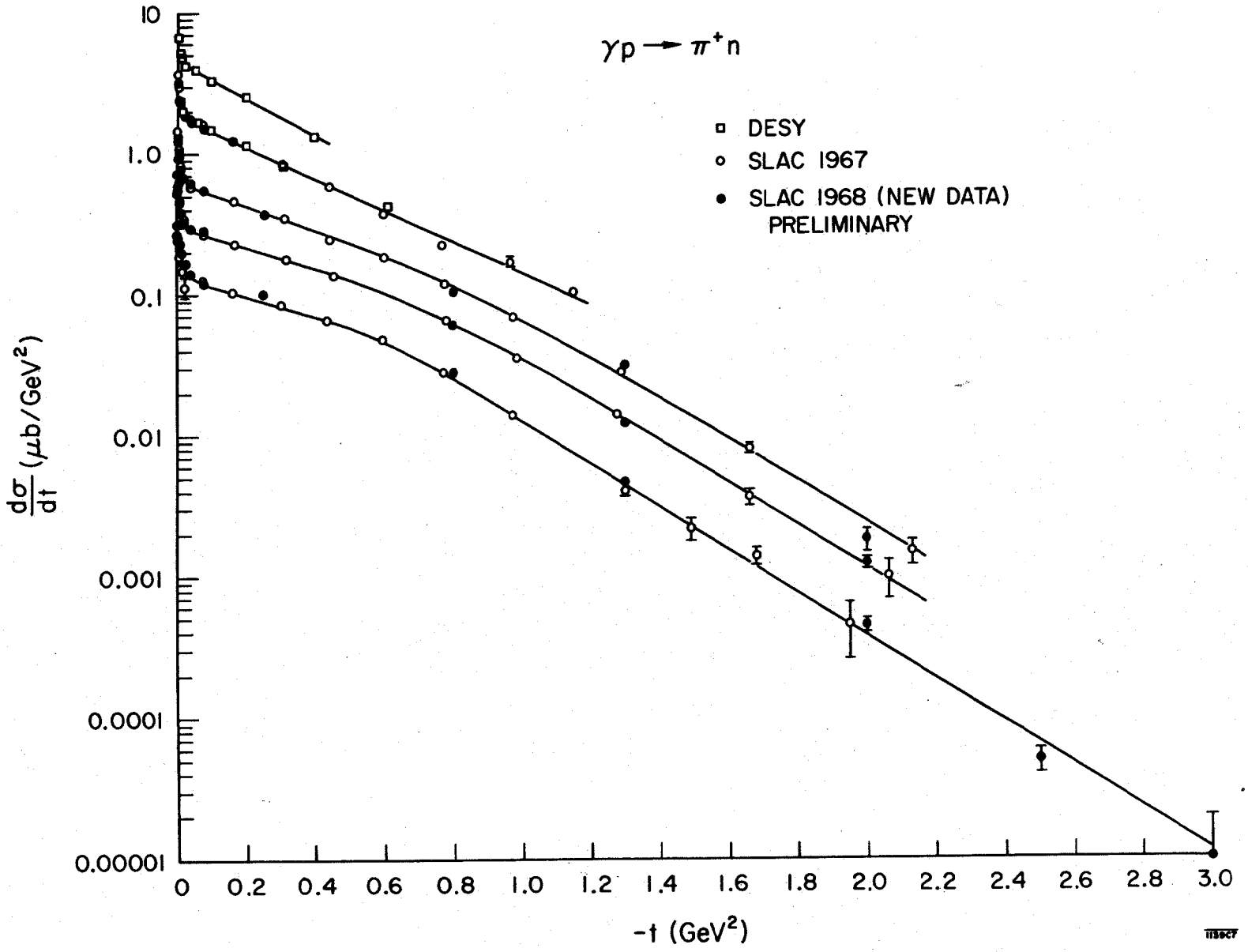
$\gamma p \rightarrow \pi^+ n$
DESY
SLAC 1967
SLAC 1968 (NEW DATA)
PRELIMINARY
$\frac{d\sigma}{dt}$ (μb/GeV^2)
10
1.0
0.1
0.01
0.001
0.0001
0.00001
0
0.2
0.4
0.6
0.8
1.0
1.2
1.4
1.6
1.8
2.0
2.2
2.4
2.6
2.8
3.0
-t (GeV^2)

Fig. 22

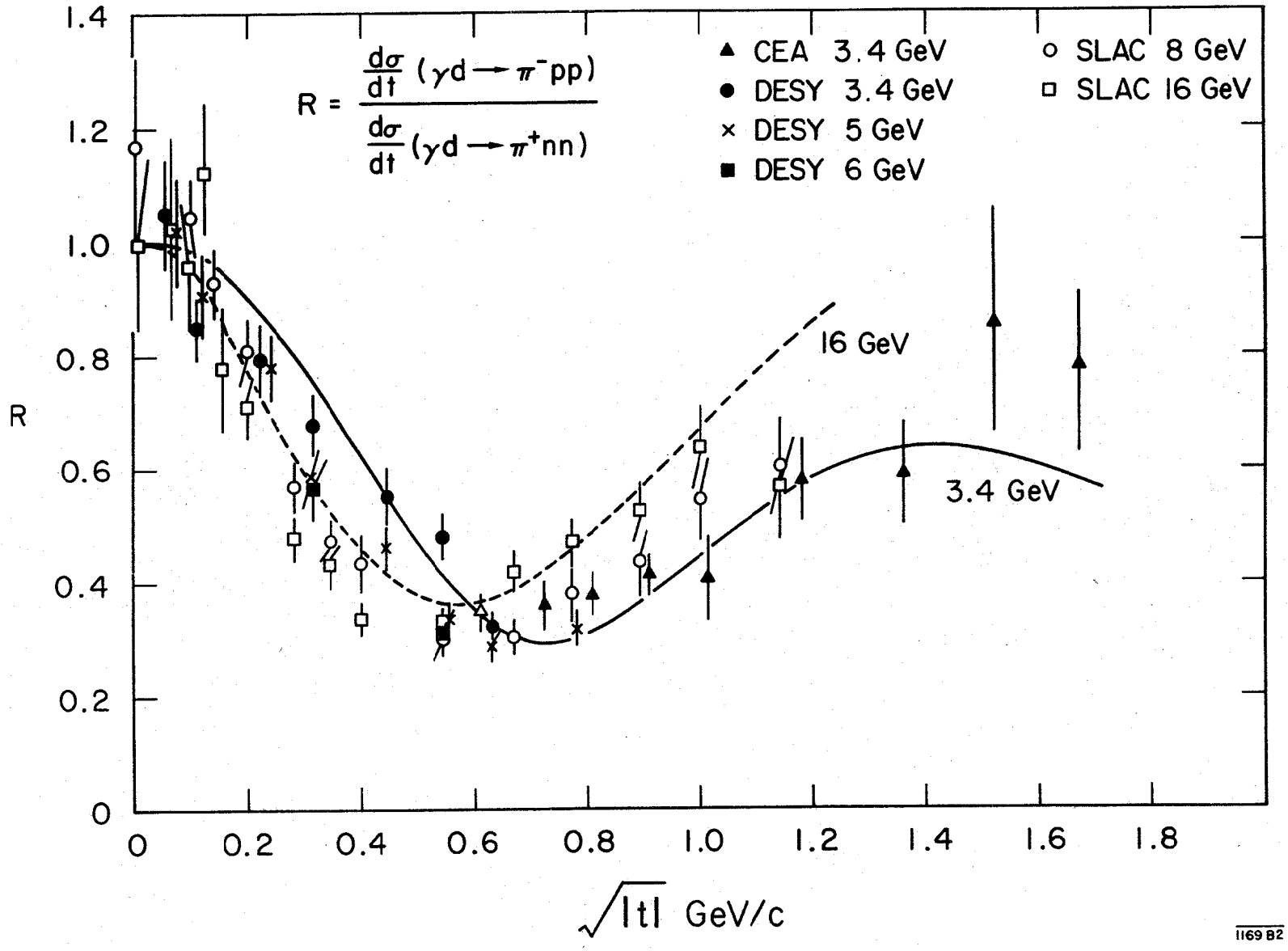
R = dσ/dt (γd → π⁻pp) / dσ/dt (γd → π⁺nn)
CEA 3.4 GeV
DESY 3.4 GeV
DESY 5 GeV
DESY 6 GeV
SLAC 8 GeV
SLAC 16 GeV
16 GeV
3.4 GeV
R
√|t| GeV/c
1169 B2

Fig. 23

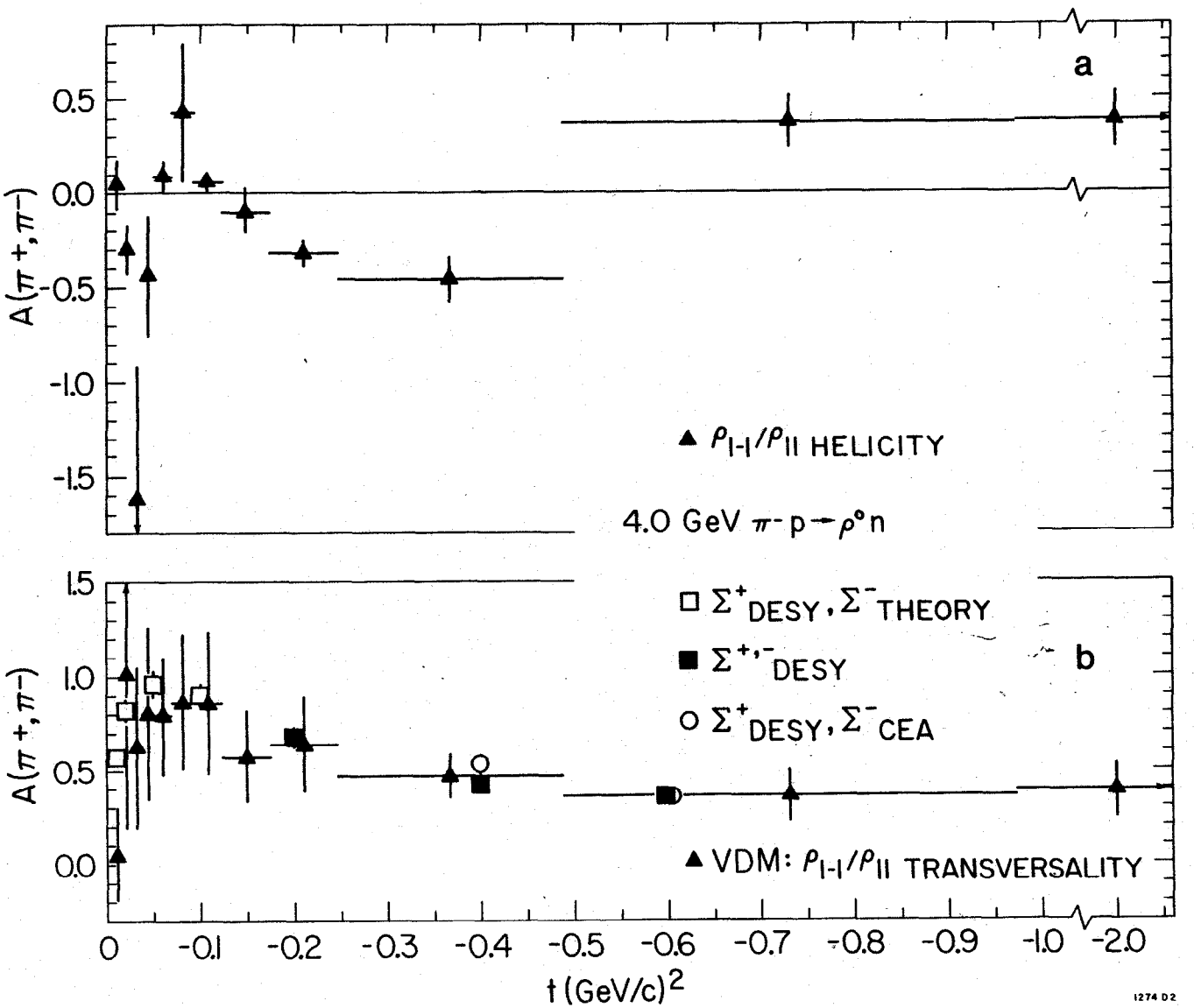
a
0.5
0.0
-0.5
-1.0
-1.5
A(π+,π−)
▲ ρ1-1/ρ11 HELICITY
4.0 GeV π⁻p→ρ°n
b
1.5
1.0
0.5
0.0
□ Σ+DESY, Σ−THEORY
■ Σ+,−DESY
○ Σ+DESY, Σ−CEA
▲ VDM: ρ1-1/ρ11 TRANSVERSALITY
0
-0.1
-0.2
-0.3
-0.4
-0.5
-0.6
-0.7
-0.8
-0.9
-1.0
-2.0
t (GeV/c)²
1274 D2

Fig. 24

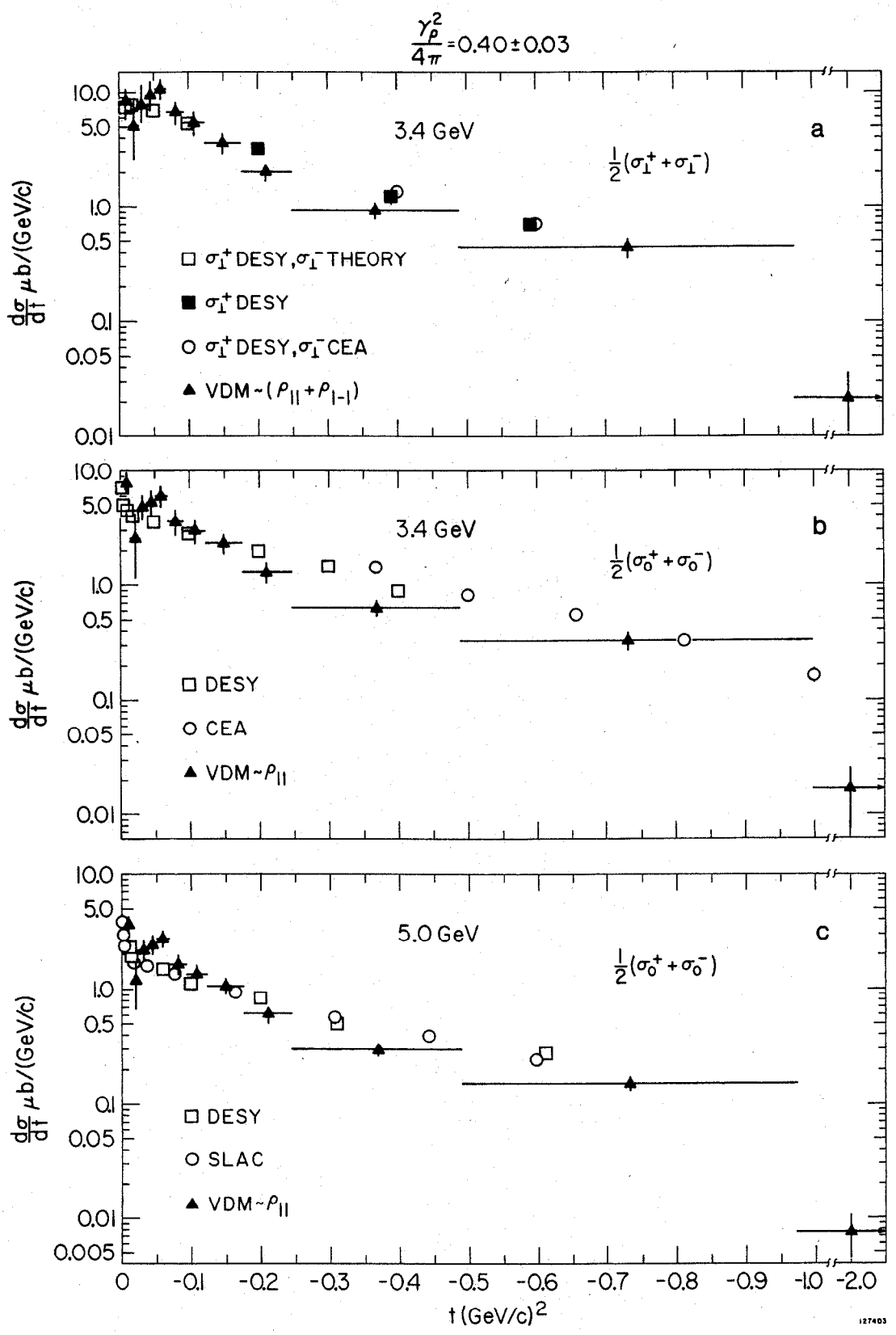
$\frac{\gamma_\rho^2}{4\pi}$=0.40±0.03
3.4 GeV
a
$\frac{1}{2}(\sigma_1^+ + \sigma_1^-)$
$\frac{d\sigma}{dt}$ μb/(GeV/c)
□ σ_1^+ DESY, σ_1^- THEORY
■ σ_1^+ DESY
○ σ_1^+ DESY, σ_1^- CEA
▲ VDM~($\rho_{11}+\rho_{1-1}$)
3.4 GeV
b
$\frac{1}{2}(\sigma_0^+ + \sigma_0^-)$
□ DESY
○ CEA
▲ VDM~ρ_{11}
5.0 GeV
c
$\frac{1}{2}(\sigma_0^+ + \sigma_0^-)$
□ DESY
○ SLAC
▲ VDM~ρ_{11}
t (GeV/c)^2
127403

Fig. 25

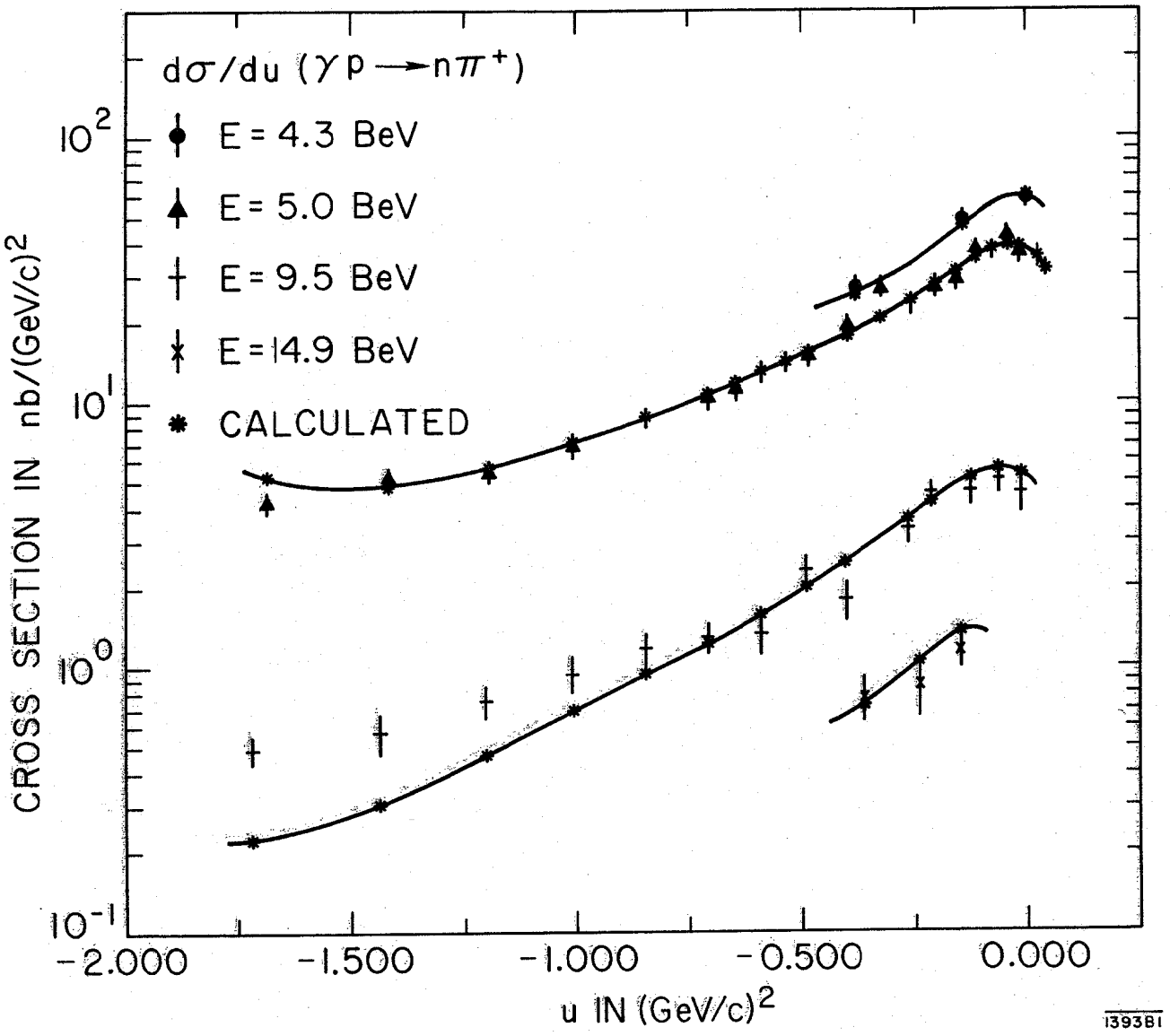
dσ/du (γp → nπ⁺)
E = 4.3 BeV
E = 5.0 BeV
E = 9.5 BeV
E = 14.9 BeV
CALCULATED
CROSS SECTION IN nb/(GeV/c)²
10²
10¹
10⁰
10⁻¹
-2.000
-1.500
-1.000
-0.500
0.000
u IN (GeV/c)²
139381

Fig. 26

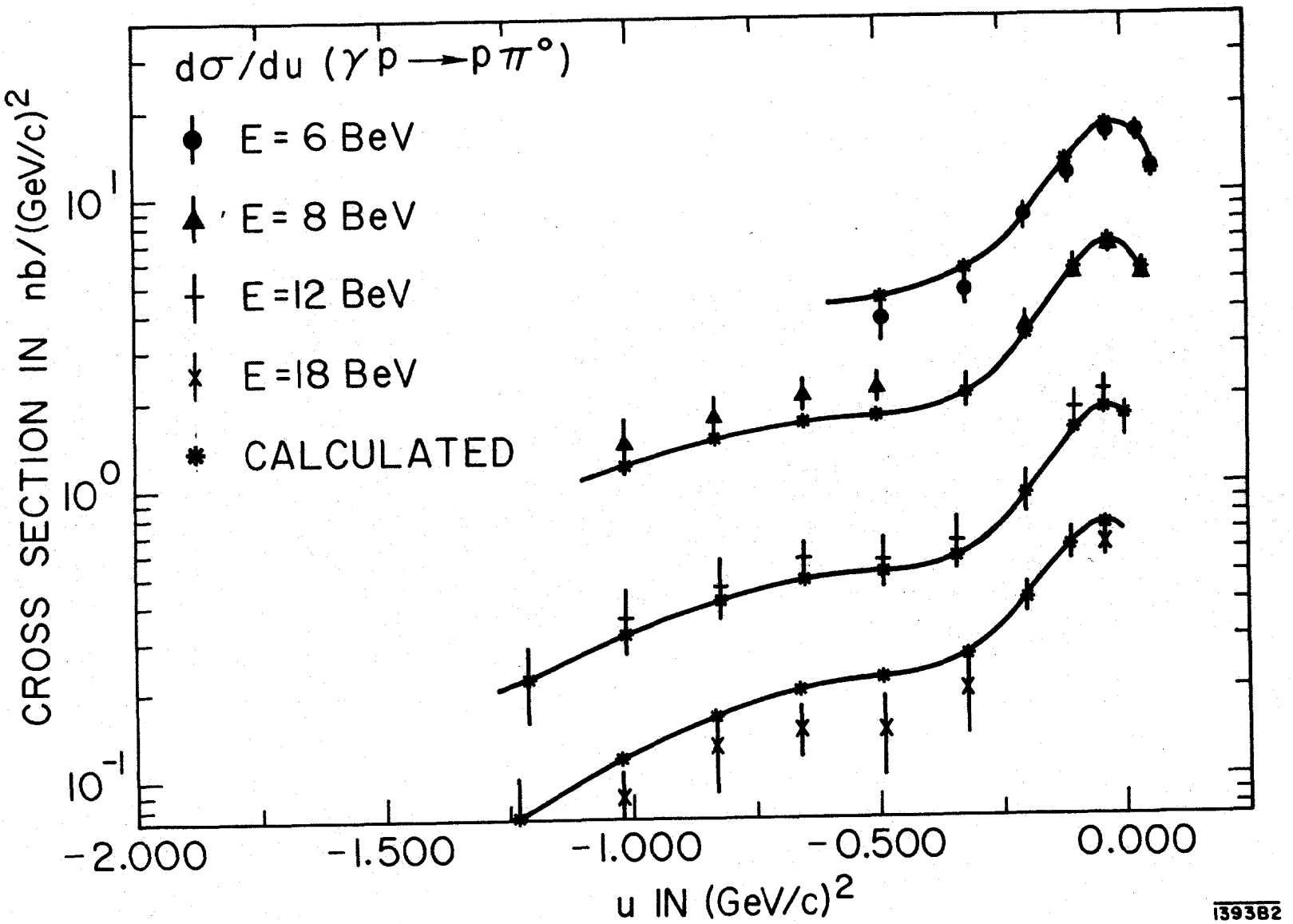
dσ/du (γ p → p π°)
E = 6 BeV
E = 8 BeV
E = 12 BeV
E = 18 BeV
CALCULATED
CROSS SECTION IN nb/(GeV/c)²
10⁻
10⁰
10⁻¹
-2.000
-1.500
-1.000
-0.500
0.000
u IN (GeV/c)²
139382

Fig. 27

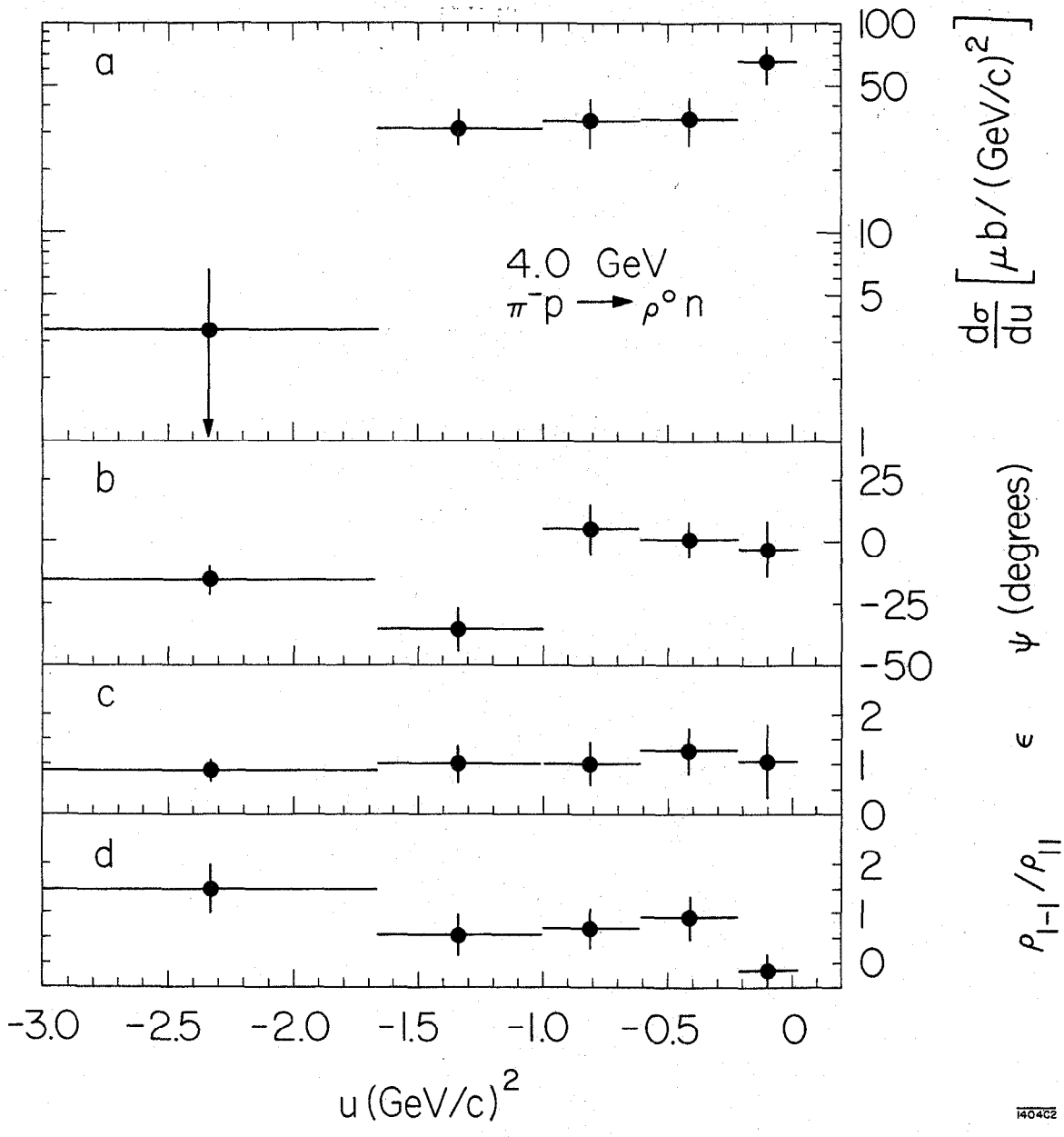
a
b
c
d
4.0 GeV
$\pi^- p \rightarrow \rho^0 n$
100
50
10
5
25
0
-25
-50
2
0
2
0
-3.0
-2.5
-2.0
-1.5
-1.0
-0.5
0
$u\,(\mathrm{GeV/c})^2$
$\frac{d\sigma}{du}\left[\mu b/(\mathrm{GeV/c})^2\right]$
ψ (degrees)
ϵ
ρ_{1-1}/ρ_{11}
140402

Fig. 28

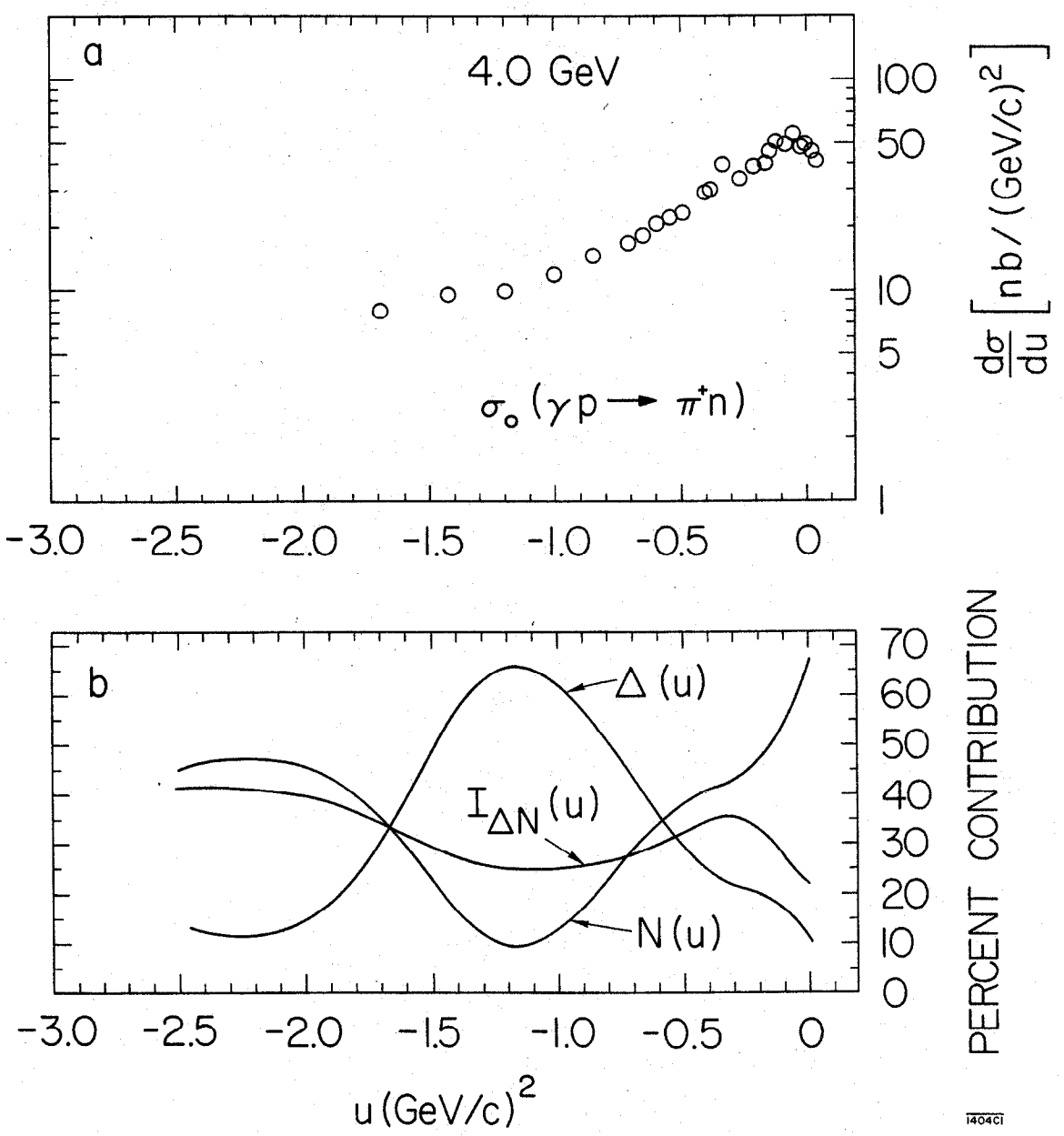
a
4.0 GeV
100
50
10
5
1
$\sigma_o(\gamma p \rightarrow \pi^+ n)$
$\frac{d\sigma}{du}\left[nb/(GeV/c)^2\right]$
-3.0
-2.5
-2.0
-1.5
-1.0
-0.5
0
b
$\Delta(u)$
$I_{\Delta N}(u)$
$N(u)$
70
60
50
40
30
20
10
0
PERCENT CONTRIBUTION
$u\,(GeV/c)^2$
1404C1

Fig. 29

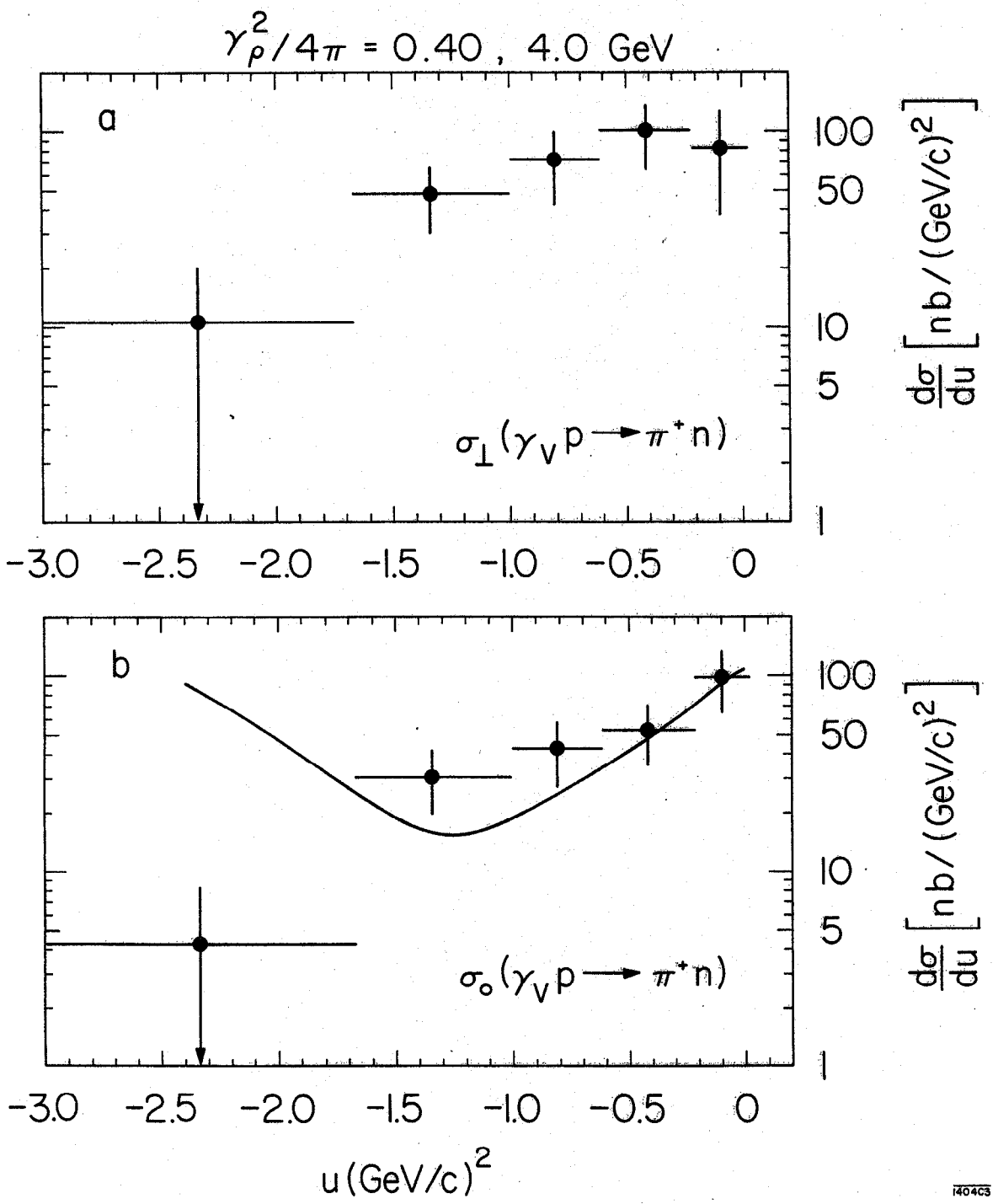
$\gamma_\rho^2/4\pi$ = 0.40 , 4.0 GeV
a
$\sigma_\perp(\gamma_V p \to \pi^+ n)$
b
$\sigma_o(\gamma_V p \to \pi^+ n)$
100
50
10
5
1
$\frac{d\sigma}{du}\left[nb/(GeV/c)^2\right]$
-3.0
-2.5
-2.0
-1.5
-1.0
-0.5
0
$u\,(GeV/c)^2$
I404C3

Fig. 30

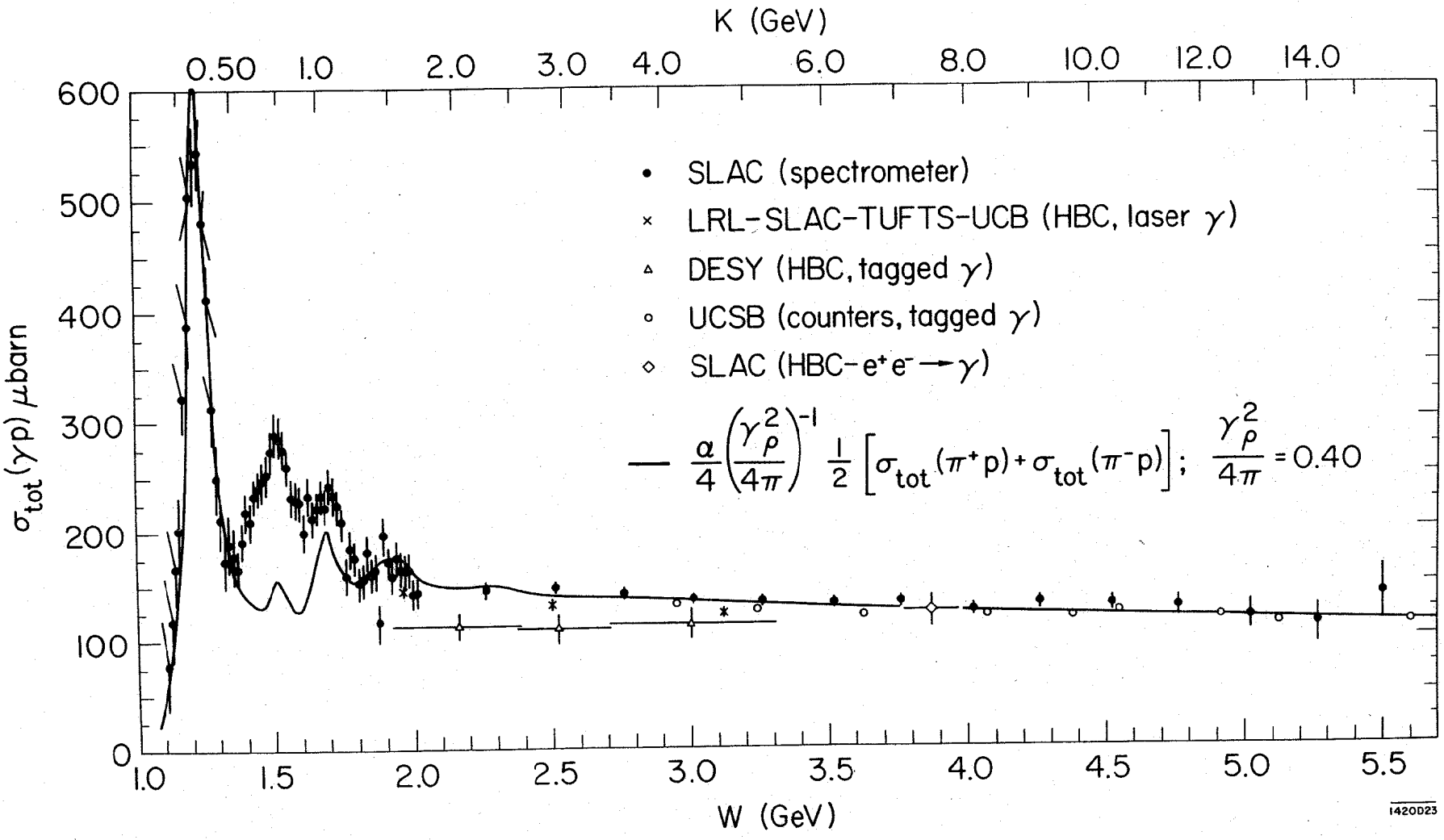
K (GeV)
0.50
1.0
2.0
3.0
4.0
6.0
8.0
10.0
12.0
14.0
600
500
400
300
200
100
0
$\sigma_{tot}(\gamma p)$ μbarn
SLAC (spectrometer)
LRL-SLAC-TUFTS-UCB (HBC, laser γ)
DESY (HBC, tagged γ)
UCSB (counters, tagged γ)
SLAC (HBC-$e^+e^- \rightarrow \gamma$)
$\frac{\alpha}{4}\left(\frac{\gamma_\rho^2}{4\pi}\right)^{-1}\frac{1}{2}\left[\sigma_{tot}(\pi^+p)+\sigma_{tot}(\pi^-p)\right]$; $\frac{\gamma_\rho^2}{4\pi}=0.40$
1.0
1.5
2.0
2.5
3.0
3.5
4.0
4.5
5.0
5.5
W (GeV)
1420D23

Fig. 31

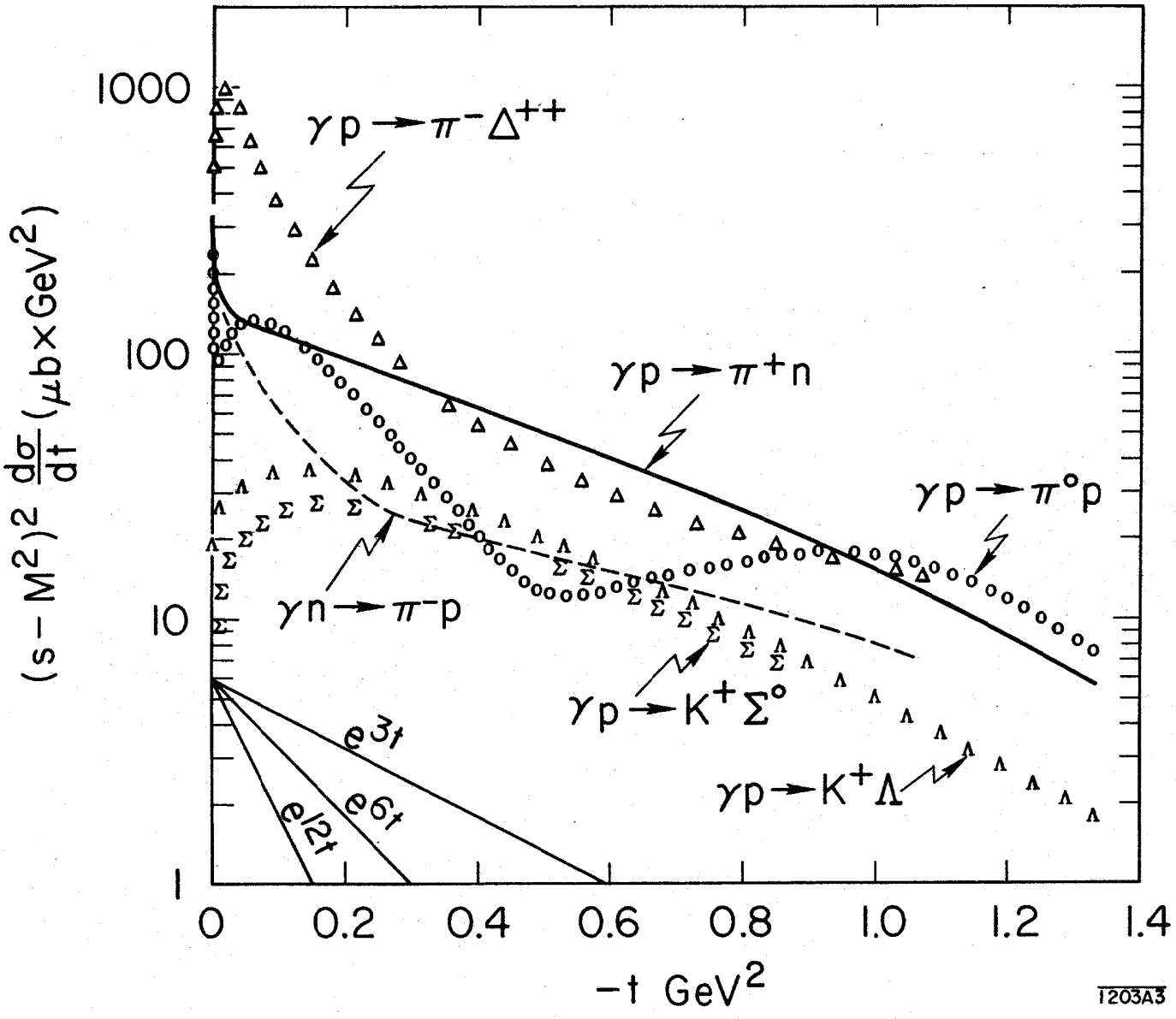
1000
100
10
1
$(s-M^2)^2 \frac{d\sigma}{dt}$ (μb×GeV^2)
$\gamma p \to \pi^- \Delta^{++}$
$\gamma p \to \pi^+ n$
$\gamma p \to \pi^\circ p$
$\gamma n \to \pi^- p$
$\gamma p \to K^+ \Sigma^\circ$
$\gamma p \to K^+ \Lambda$
e^{3t}
e^{6t}
e^{12t}
0
0.2
0.4
0.6
0.8
1.0
1.2
1.4
$-t$ GeV^2
1203A3

Fig. 32

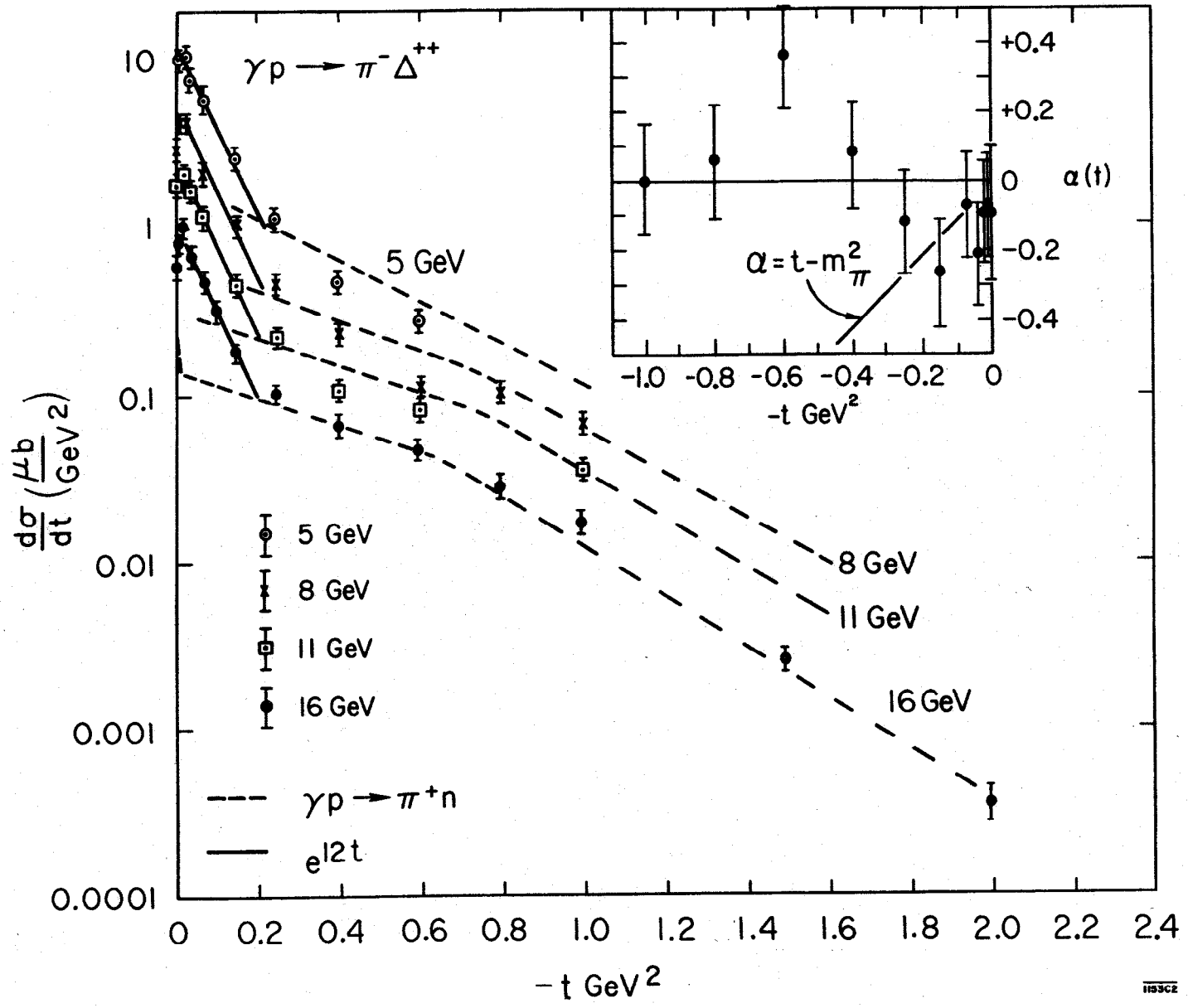
$\gamma p \rightarrow \pi^- \Delta^{++}$
5 GeV
8 GeV
11 GeV
16 GeV
$\frac{d\sigma}{dt}\left(\frac{\mu b}{GeV^2}\right)$
10
1
0.1
0.01
0.001
0.0001
0
0.2
0.4
0.6
0.8
1.0
1.2
1.4
1.6
1.8
2.0
2.2
2.4
$-t\ GeV^2$
5 GeV
8 GeV
11 GeV
16 GeV
$\gamma p \rightarrow \pi^+ n$
e^{12t}
+0.4
+0.2
0
-0.2
-0.4
$\alpha(t)$
$\alpha = t - m_\pi^2$
-1.0
-0.8
-0.6
-0.4
-0.2
0
$-t\ GeV^2$
1153C2

Fig. 33

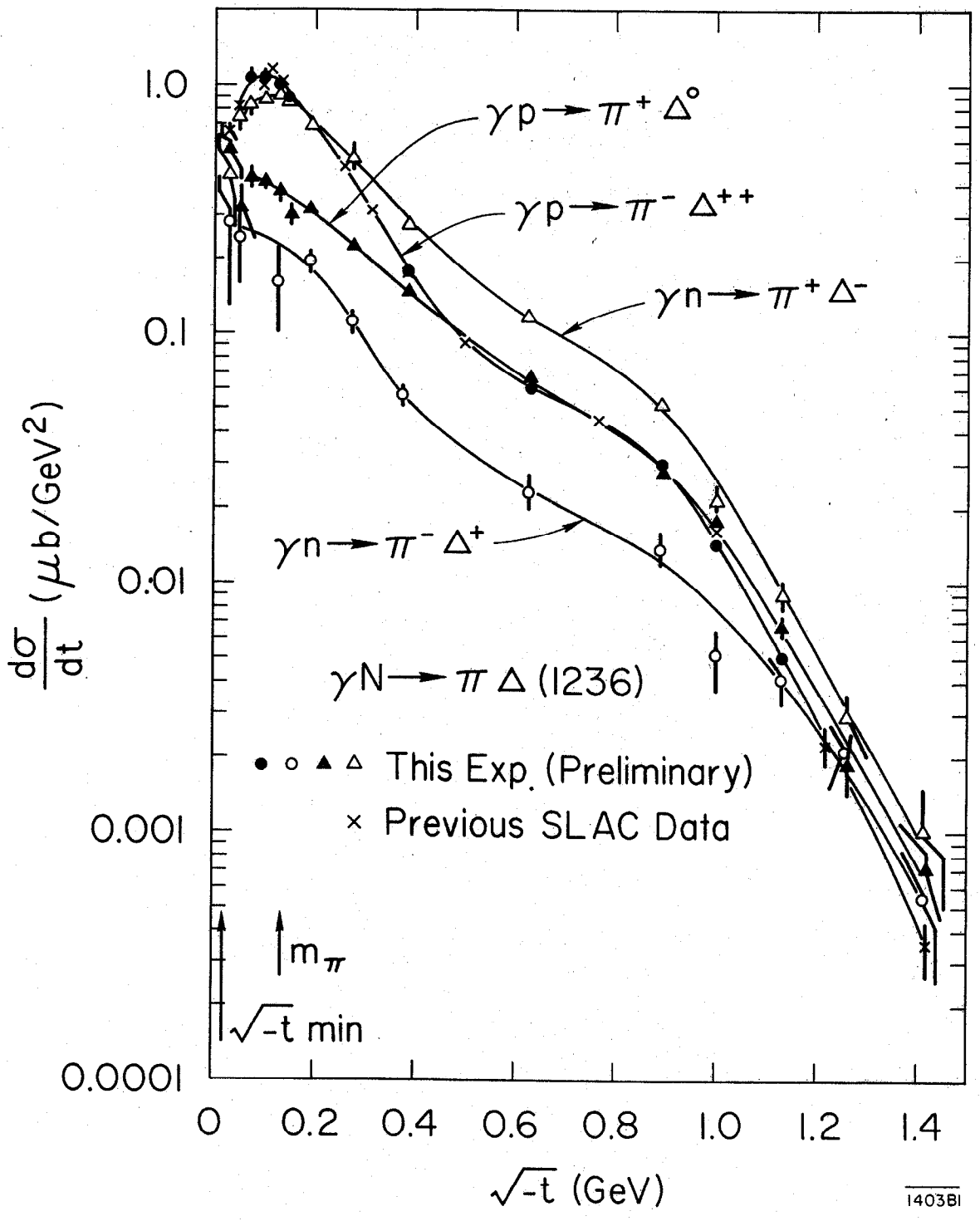
1.0
0.1
0.01
0.001
0.0001
$\frac{d\sigma}{dt}$ (μb/GeV^2)
$\gamma p \rightarrow \pi^+ \Delta^\circ$
$\gamma p \rightarrow \pi^- \Delta^{++}$
$\gamma n \rightarrow \pi^+ \Delta^-$
$\gamma n \rightarrow \pi^- \Delta^+$
$\gamma N \rightarrow \pi \Delta$ (1236)
This Exp. (Preliminary)
Previous SLAC Data
m_π
$\sqrt{-t}$ min
0
0.2
0.4
0.6
0.8
1.0
1.2
1.4
$\sqrt{-t}$ (GeV)
1403B1

Fig. 34

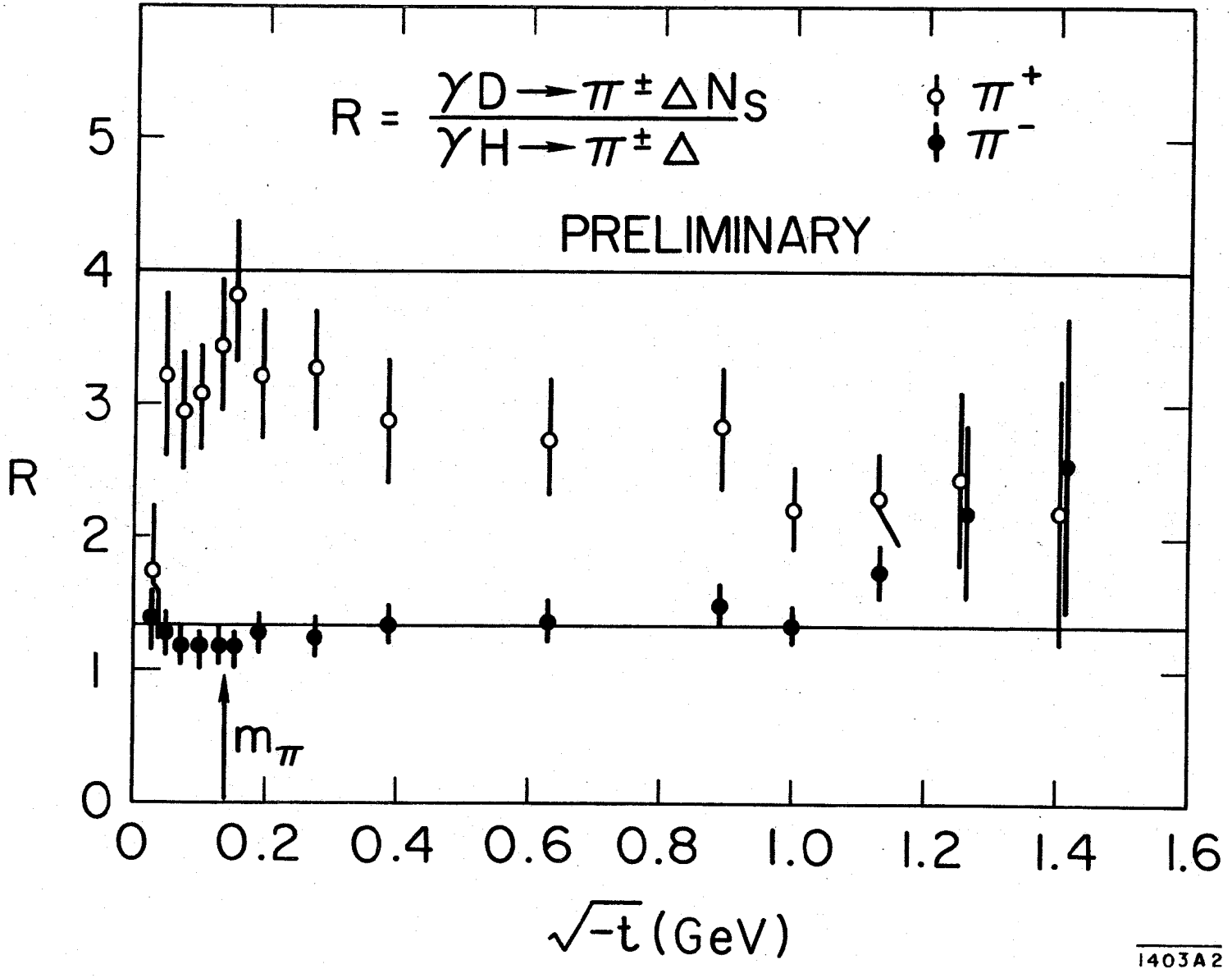
R = γD → π±ΔNs / γH → π±Δ
π+
π−
PRELIMINARY
R
m_π
√−t (GeV)
0
1
2
3
4
5
0
0.2
0.4
0.6
0.8
1.0
1.2
1.4
1.6
1403A2

Fig. 35

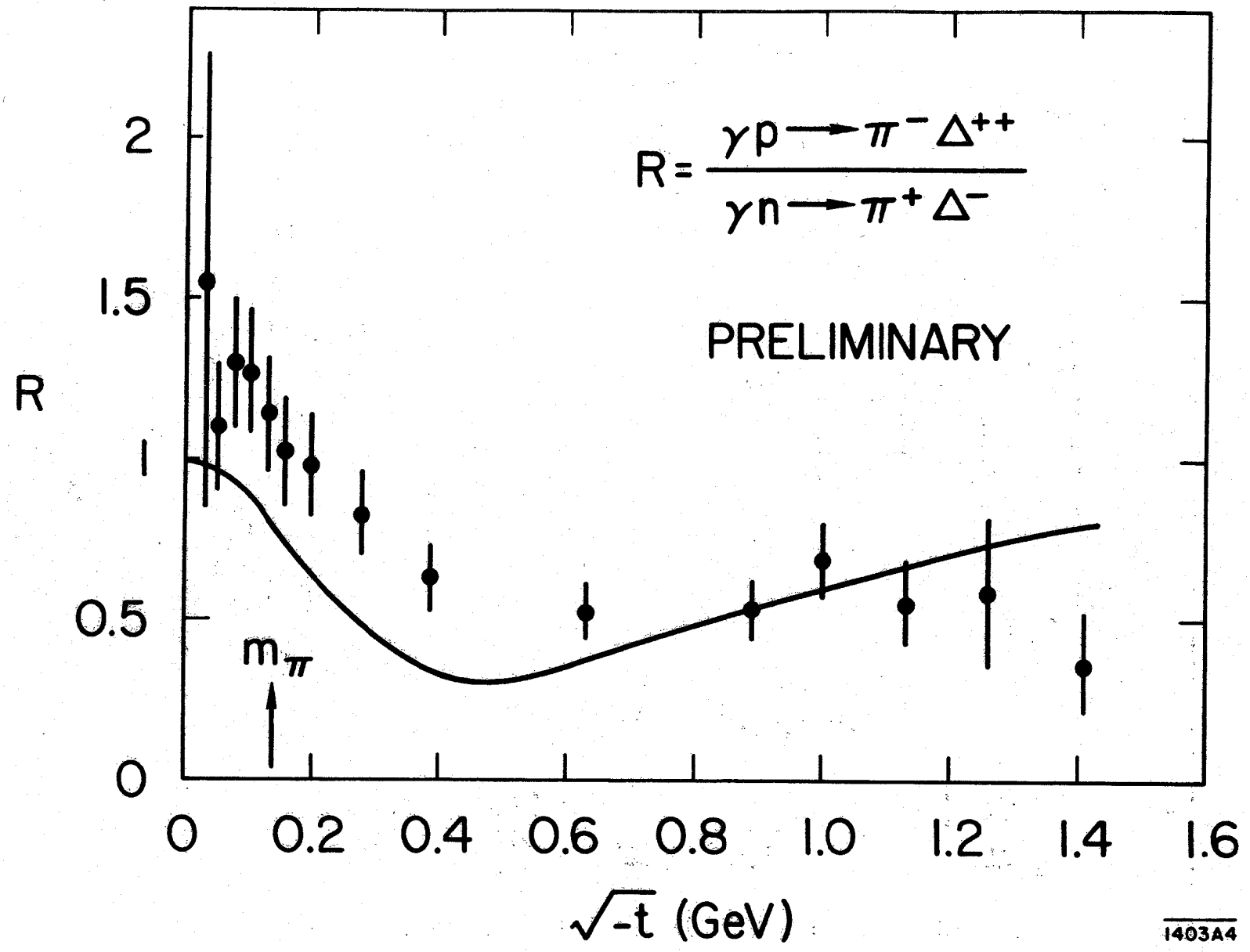
R = γp → π⁻Δ⁺⁺ / γn → π⁺Δ⁻
PRELIMINARY
R
2
1.5
1
0.5
0
m_π
0
0.2
0.4
0.6
0.8
1.0
1.2
1.4
1.6
√-t (GeV)
1403A4

Fig. 36

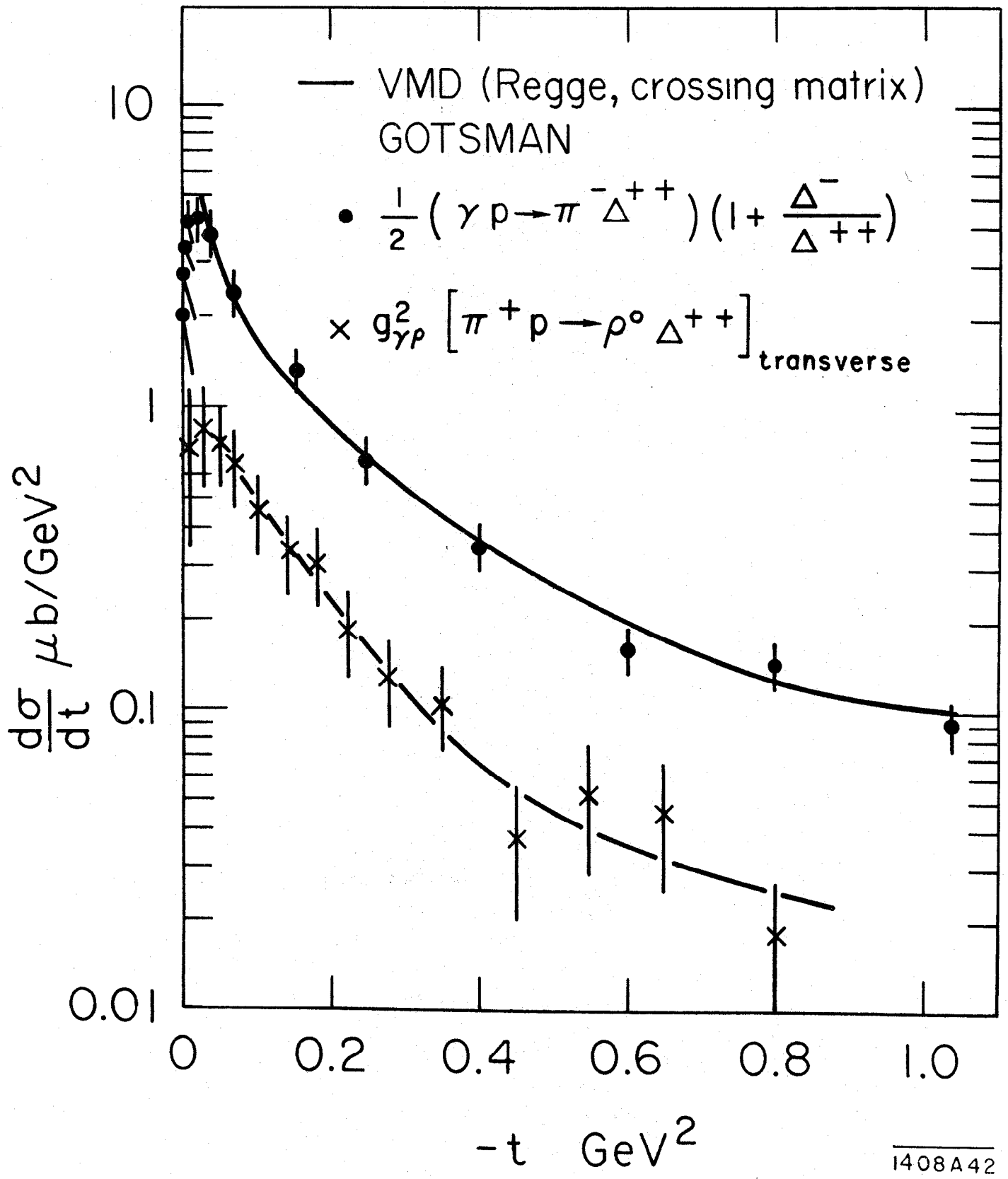
VMD (Regge, crossing matrix)
GOTSMAN
$\frac{1}{2}(\gamma p \to \pi^- \Delta^{++})(1+\frac{\Delta^-}{\Delta^{++}})$
$\times\ g^2_{\gamma\rho}\left[\pi^+ p \to \rho^0 \Delta^{++}\right]_{\text{transverse}}$
$\frac{d\sigma}{dt}$ μb/GeV^2
10
1
0.1
0.01
0
0.2
0.4
0.6
0.8
1.0
$-t$ GeV^2
1408A42

Fig. 37

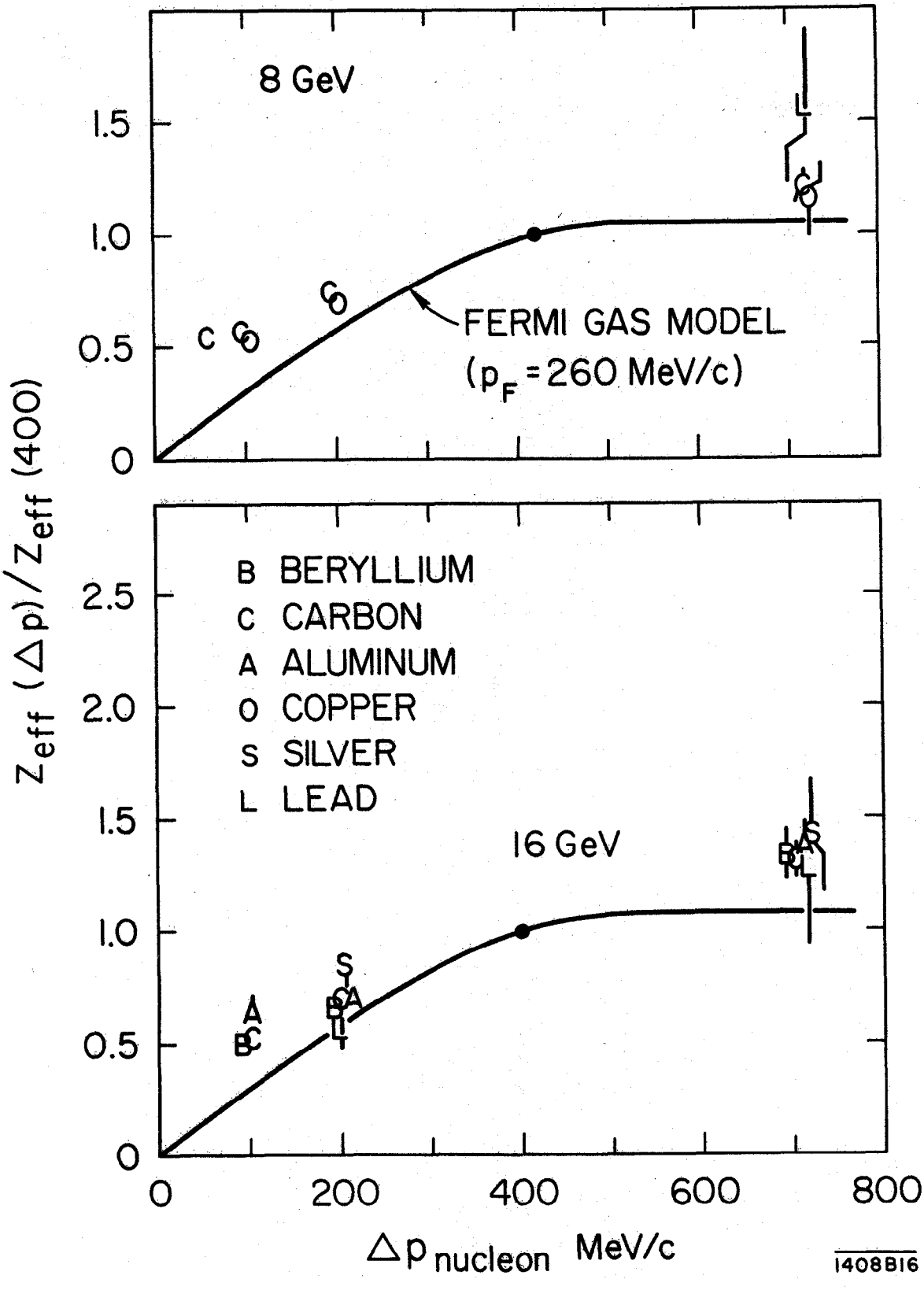
8 GeV
FERMI GAS MODEL
(p_F = 260 MeV/c)
B BERYLLIUM
C CARBON
A ALUMINUM
O COPPER
S SILVER
L LEAD
16 GeV
$Z_{eff}(\Delta p)/Z_{eff}(400)$
$\Delta p_{nucleon}$ MeV/c
1408B16

Fig. 38

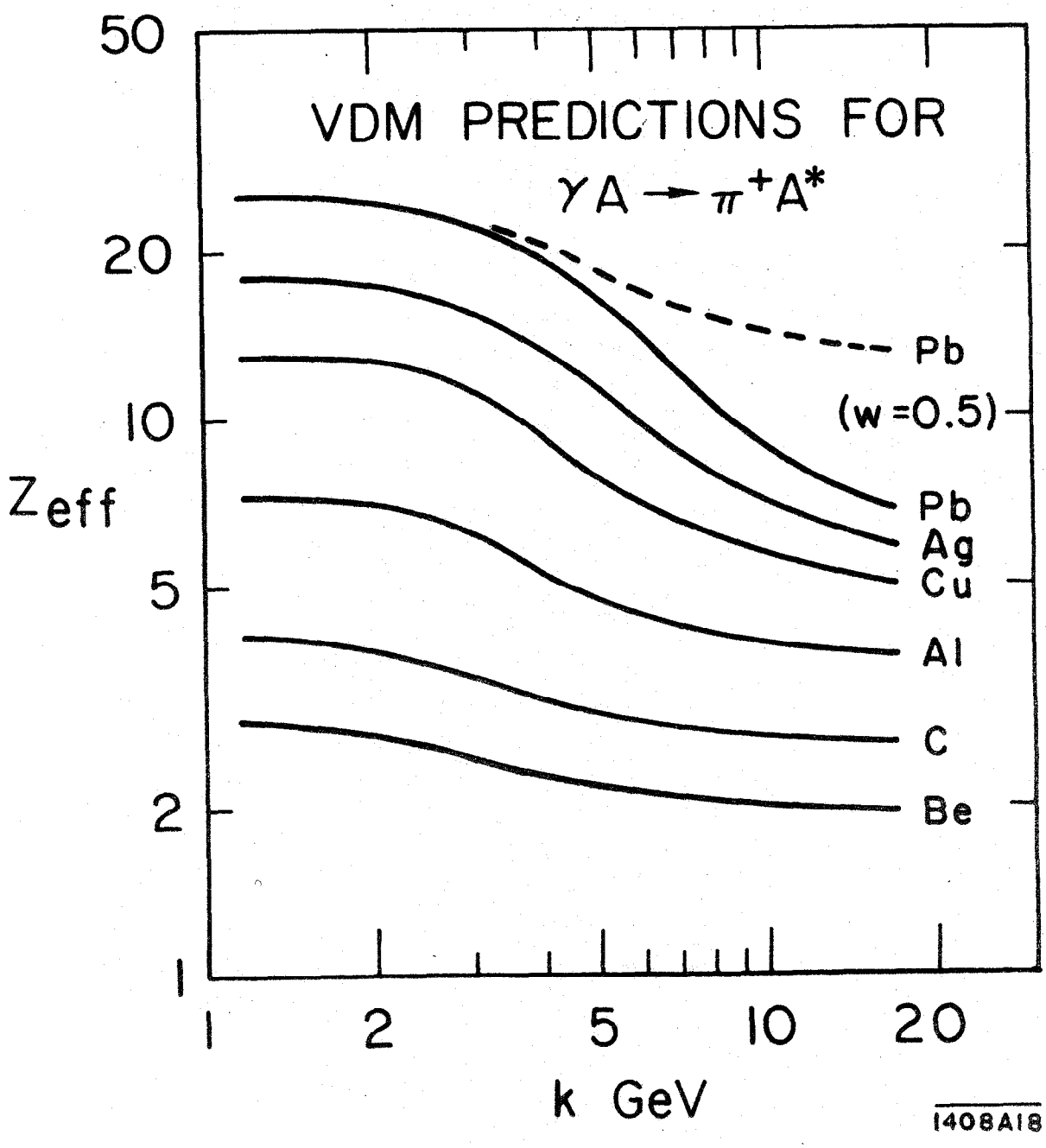
VDM PREDICTIONS FOR
$\gamma A \rightarrow \pi^+ A^*$
Pb
(w=0.5)
Pb
Ag
Cu
Al
C
Be
Z_{eff}
50
20
10
5
2
1
1
2
5
10
20
k GeV
1408A18

Fig. 39

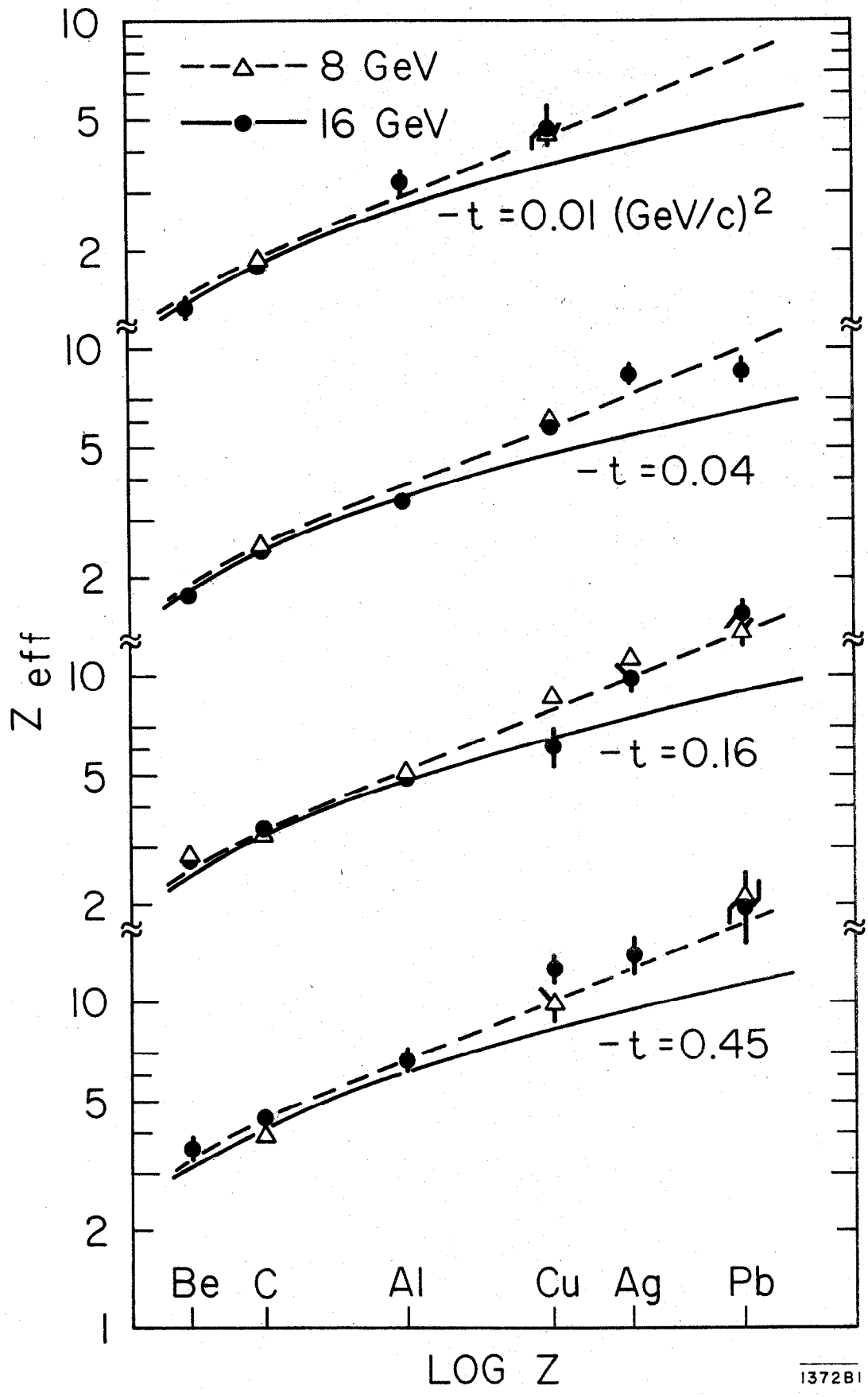
8 GeV
16 GeV
-t =0.01 (GeV/c)²
-t =0.04
-t =0.16
-t =0.45
Z eff
LOG Z
Be
C
Al
Cu
Ag
Pb
137281

Fig. 40

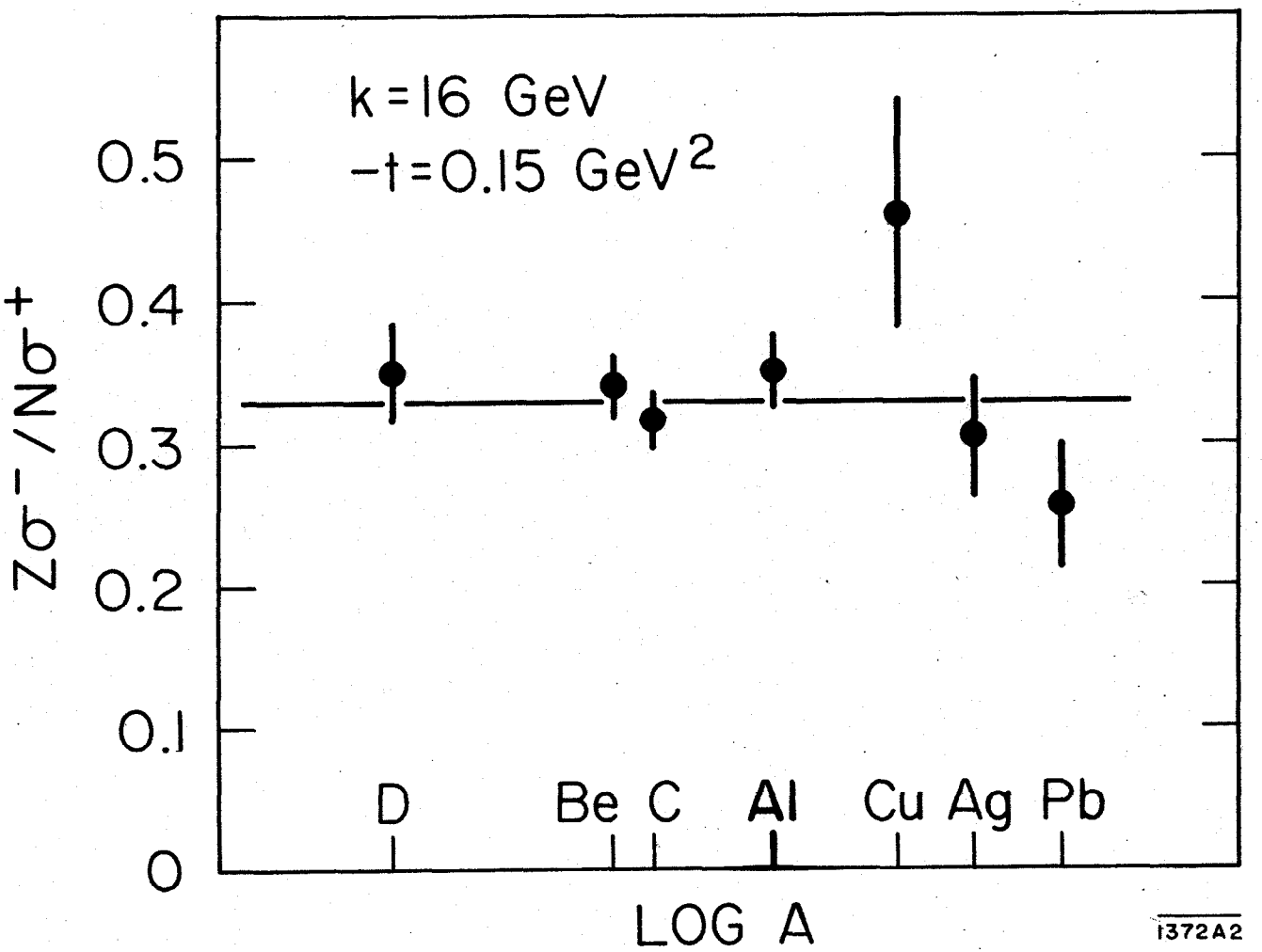
k = 16 GeV
-t = 0.15 GeV²
0.5
0.4
0.3
0.2
0.1
0
Zσ⁻/Nσ⁺
D
Be
C
Al
Cu
Ag
Pb
LOG A
1372A2

Fig. 41

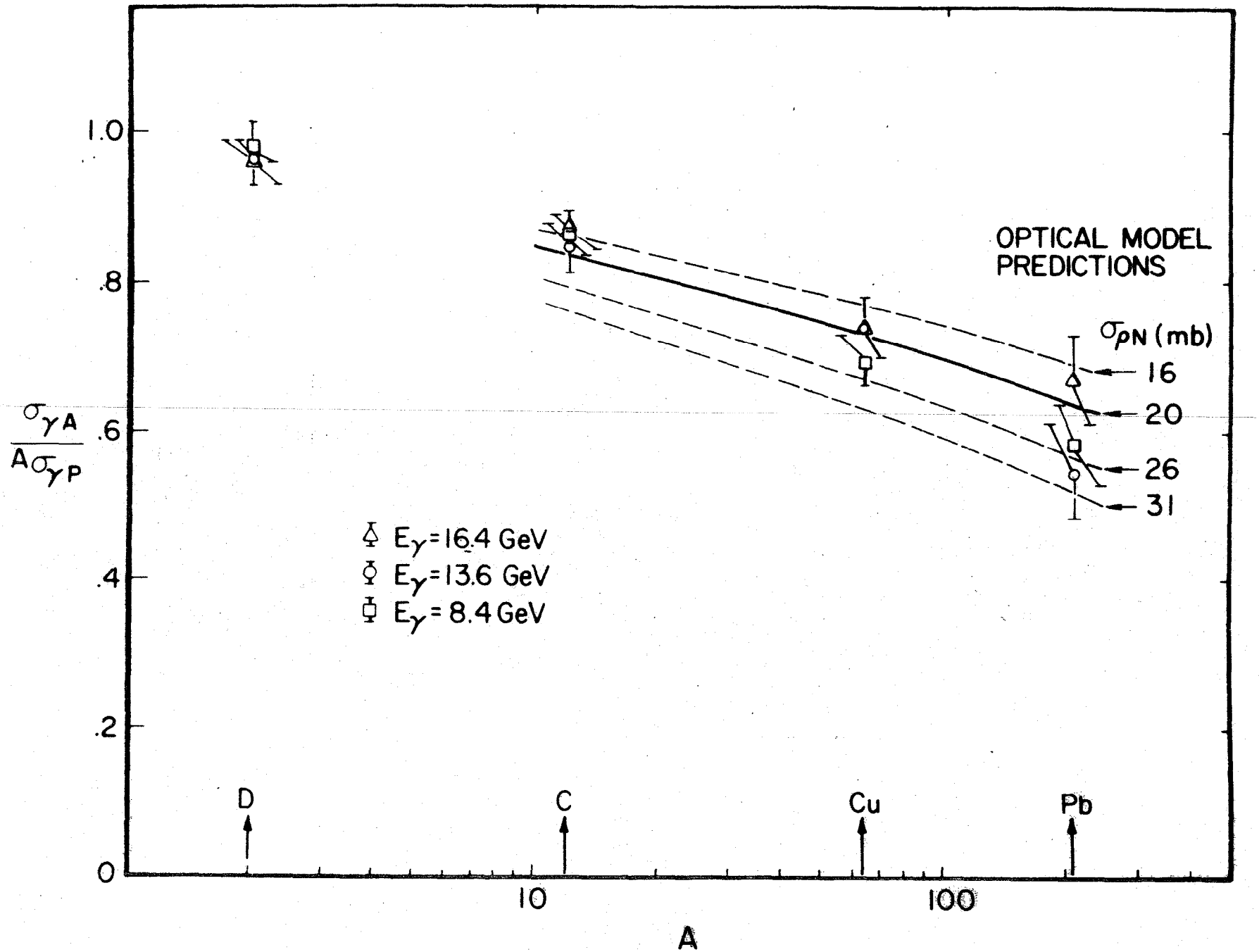
1.0
.8
.6
.4
.2
0
$\frac{\sigma_{\gamma A}}{A\sigma_{\gamma P}}$
OPTICAL MODEL
PREDICTIONS
σ_{pN} (mb)
16
20
26
31
E_γ = 16.4 GeV
E_γ = 13.6 GeV
E_γ = 8.4 GeV
D
C
Cu
Pb
10
100
A

Fig. 42

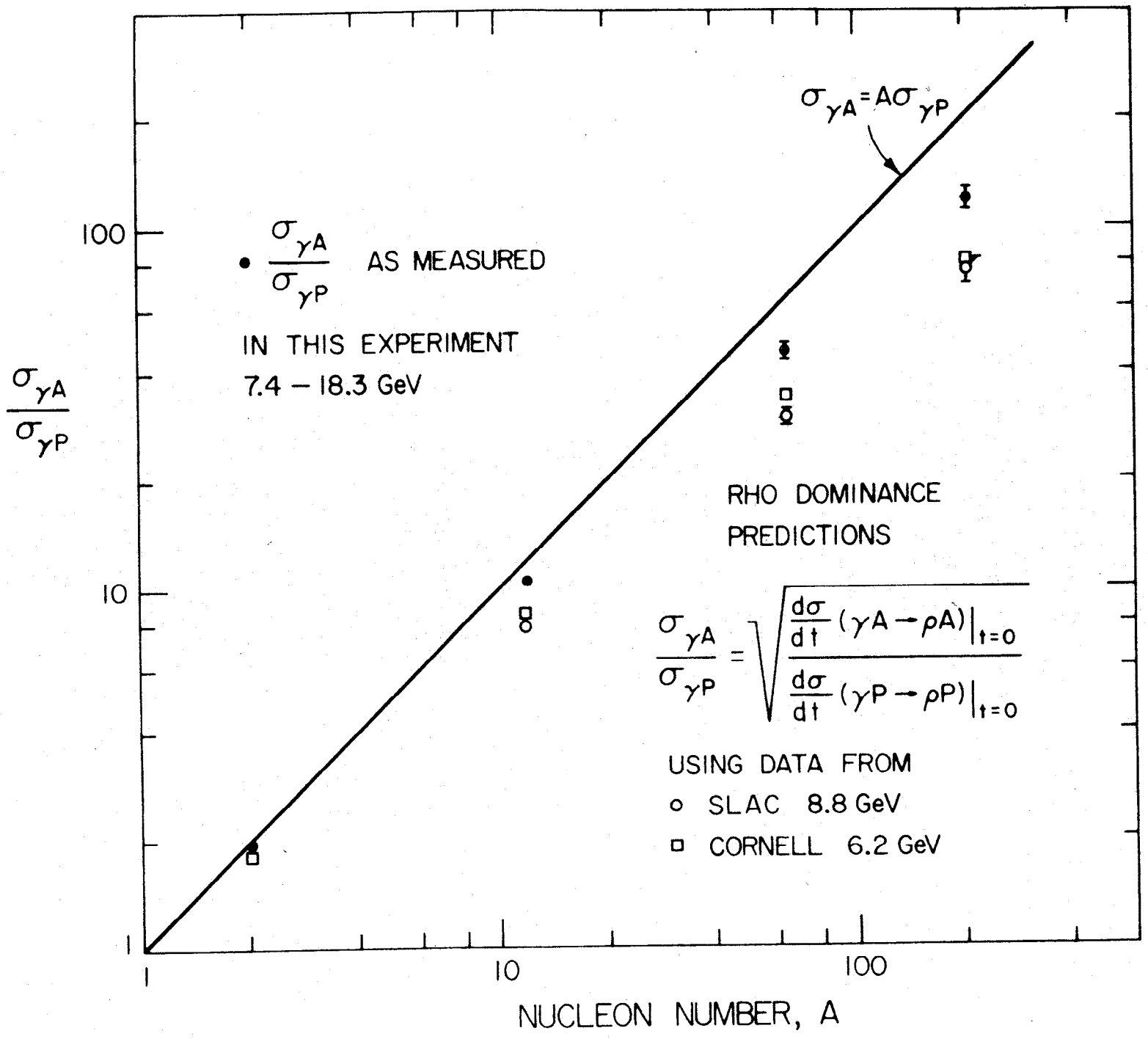
$\sigma_{\gamma A} = A\sigma_{\gamma P}$
$\frac{\sigma_{\gamma A}}{\sigma_{\gamma P}}$ AS MEASURED
IN THIS EXPERIMENT
7.4 – 18.3 GeV
RHO DOMINANCE
PREDICTIONS
$\frac{\sigma_{\gamma A}}{\sigma_{\gamma P}} = \sqrt{\frac{\frac{d\sigma}{dt}(\gamma A \to \rho A)\big|_{t=0}}{\frac{d\sigma}{dt}(\gamma P \to \rho P)\big|_{t=0}}}$
USING DATA FROM
SLAC 8.8 GeV
CORNELL 6.2 GeV
$\frac{\sigma_{\gamma A}}{\sigma_{\gamma P}}$
100
10
1
1
10
100
NUCLEON NUMBER, A

Fig. 43

a.) $\gamma N \longrightarrow \rho^{\circ} N$ (Forward)

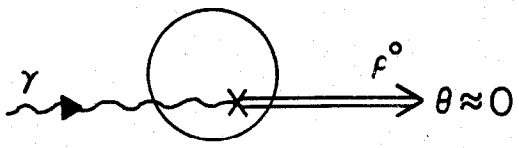

---

b.) $\gamma N \longrightarrow \gamma N$

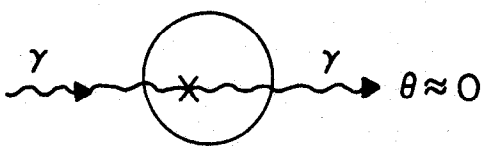

$$M_1 = C_{\rho\gamma}(0)\, C_{\rho\rho}(0)\, M_1^{VMD}$$

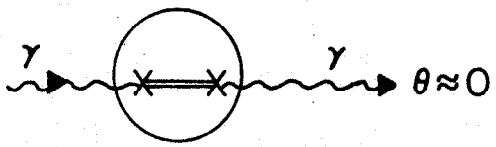

$$M_2 = \left[C_{\rho\rho}(0)\right]^2 M_2^{VMD}$$

---

c.) $\gamma N \longrightarrow N\pi$

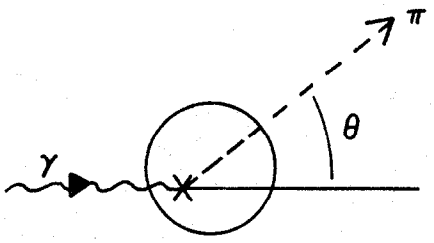

$$M_1^{\perp,\parallel}(t) = C_{\rho\pi}^{\perp,\parallel}(t)\, M_1^{VMD;\perp,\parallel}(t)$$

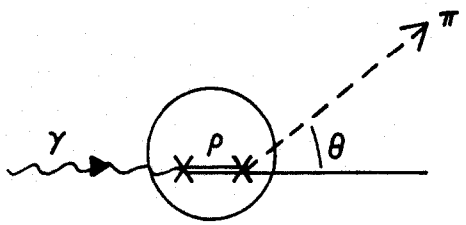

$$M_2^{\perp,\parallel}(t) = C_{\rho\rho}(0)\, M_2^{VMD;\perp,\parallel}(t)$$

---

d.) $\gamma N \longrightarrow N\rho^{\circ}$ (Incoherent)

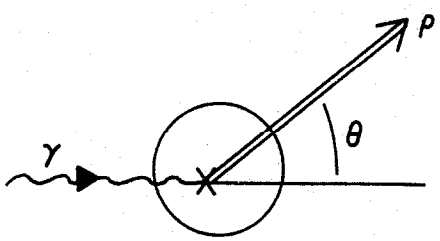

$$M_1(t) = C_{\rho\rho}(t)\, M_1^{VMD}$$

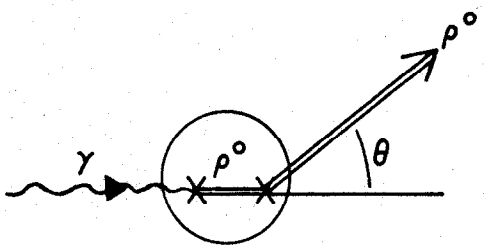

$$M_2(t) = C_{\rho\rho}(0)\, M_2^{VMD}$$

Fig. 44

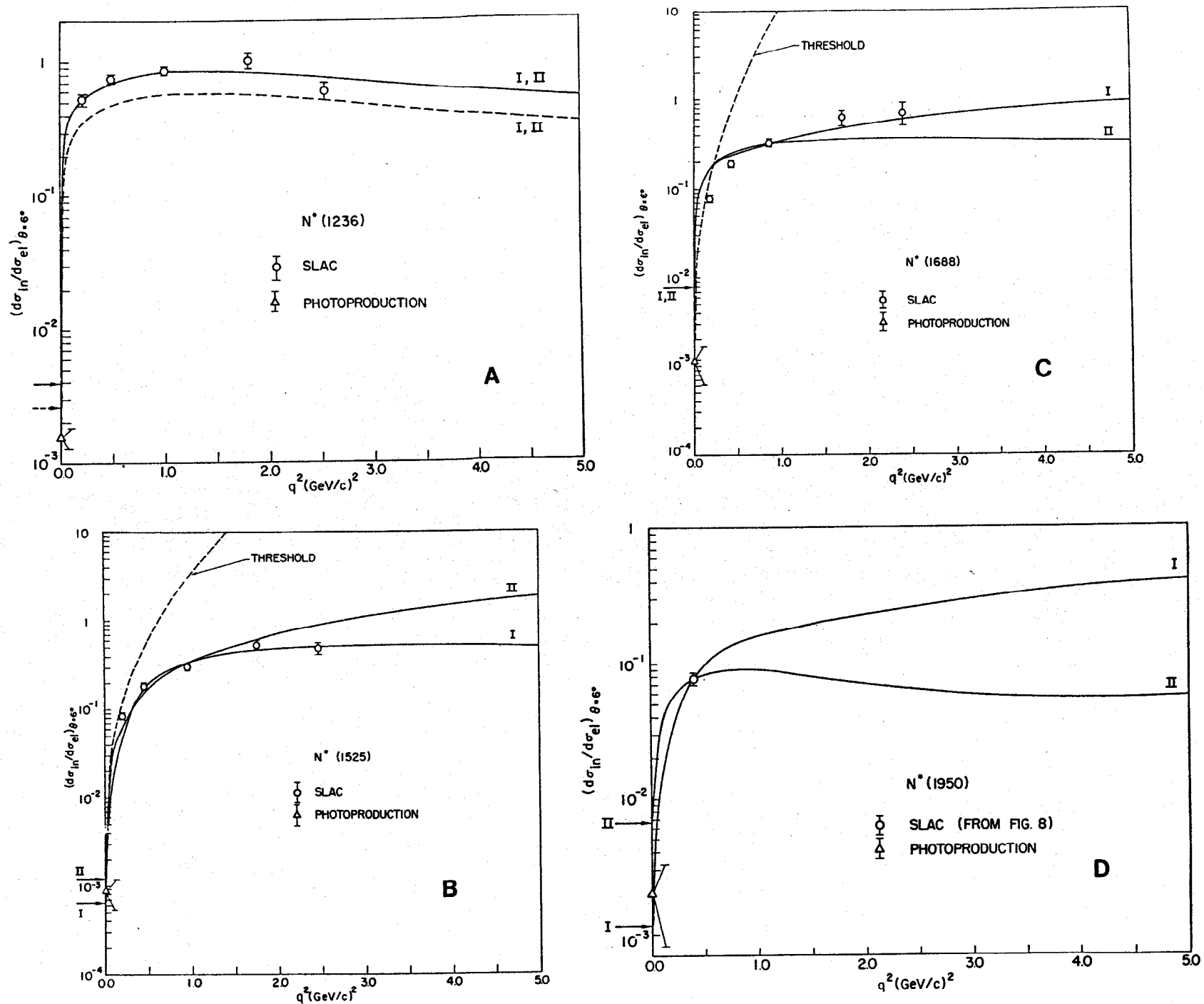
N*(1236)
SLAC
PHOTOPRODUCTION
I, II
I, II
A
THRESHOLD
N*(1688)
SLAC
PHOTOPRODUCTION
I
II
C
THRESHOLD
N*(1525)
SLAC
PHOTOPRODUCTION
II
I
B
N*(1950)
SLAC (FROM FIG. 8)
PHOTOPRODUCTION
I
II
D
$(d\sigma_{in}/d\sigma_{el})_{\theta*\epsilon*}$
$q^2(GeV/c)^2$

Fig. 45

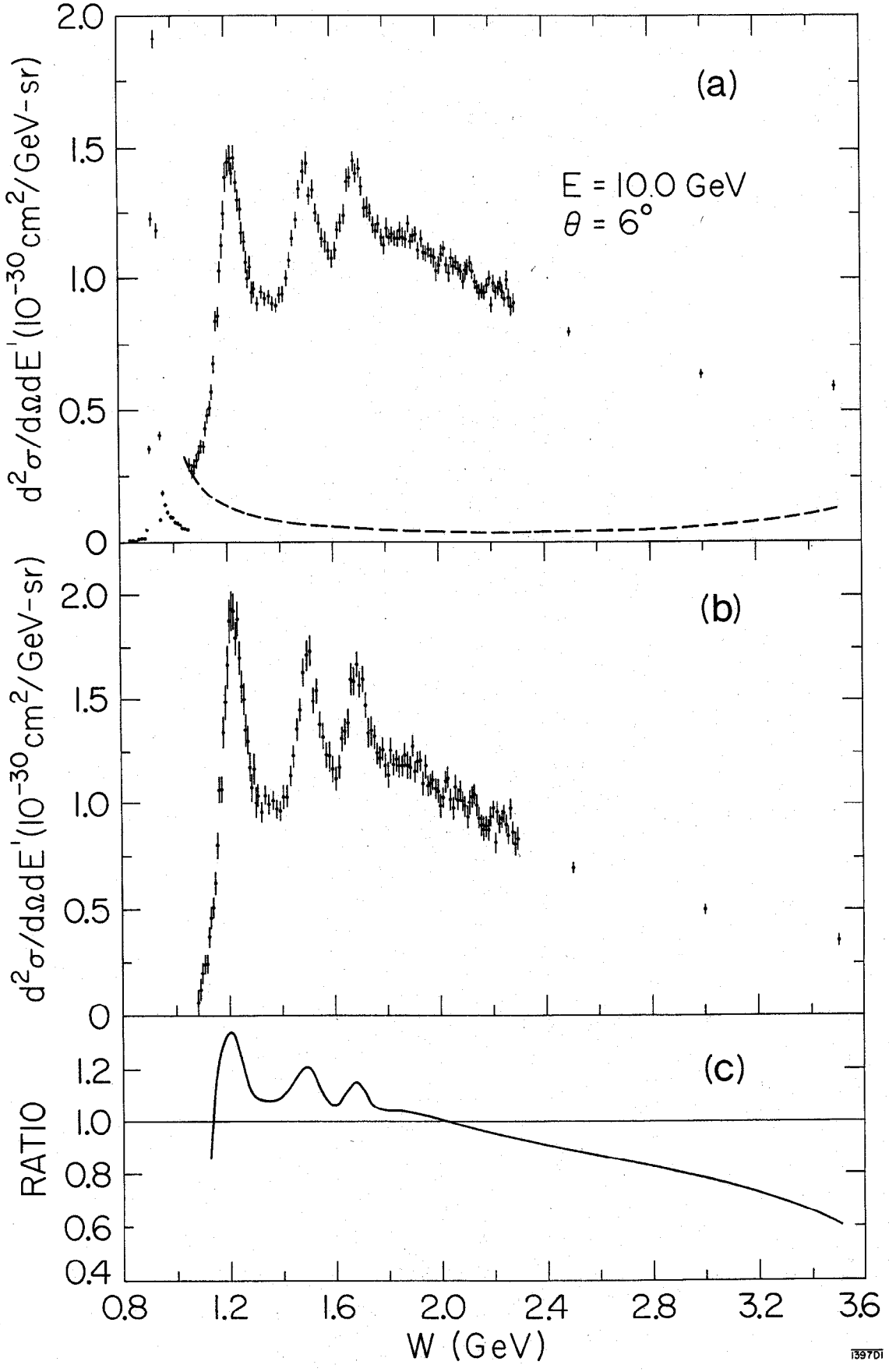
(a)
E = 10.0 GeV
θ = 6°
d²σ/dΩdE' (10⁻³⁰ cm²/GeV-sr)
(b)
d²σ/dΩdE' (10⁻³⁰ cm²/GeV-sr)
(c)
RATIO
W (GeV)
2.0
1.5
1.0
0.5
0
1.2
0.8
0.6
0.4
0.8
1.2
1.6
2.0
2.4
2.8
3.2
3.6
1397D1

Fig. 46

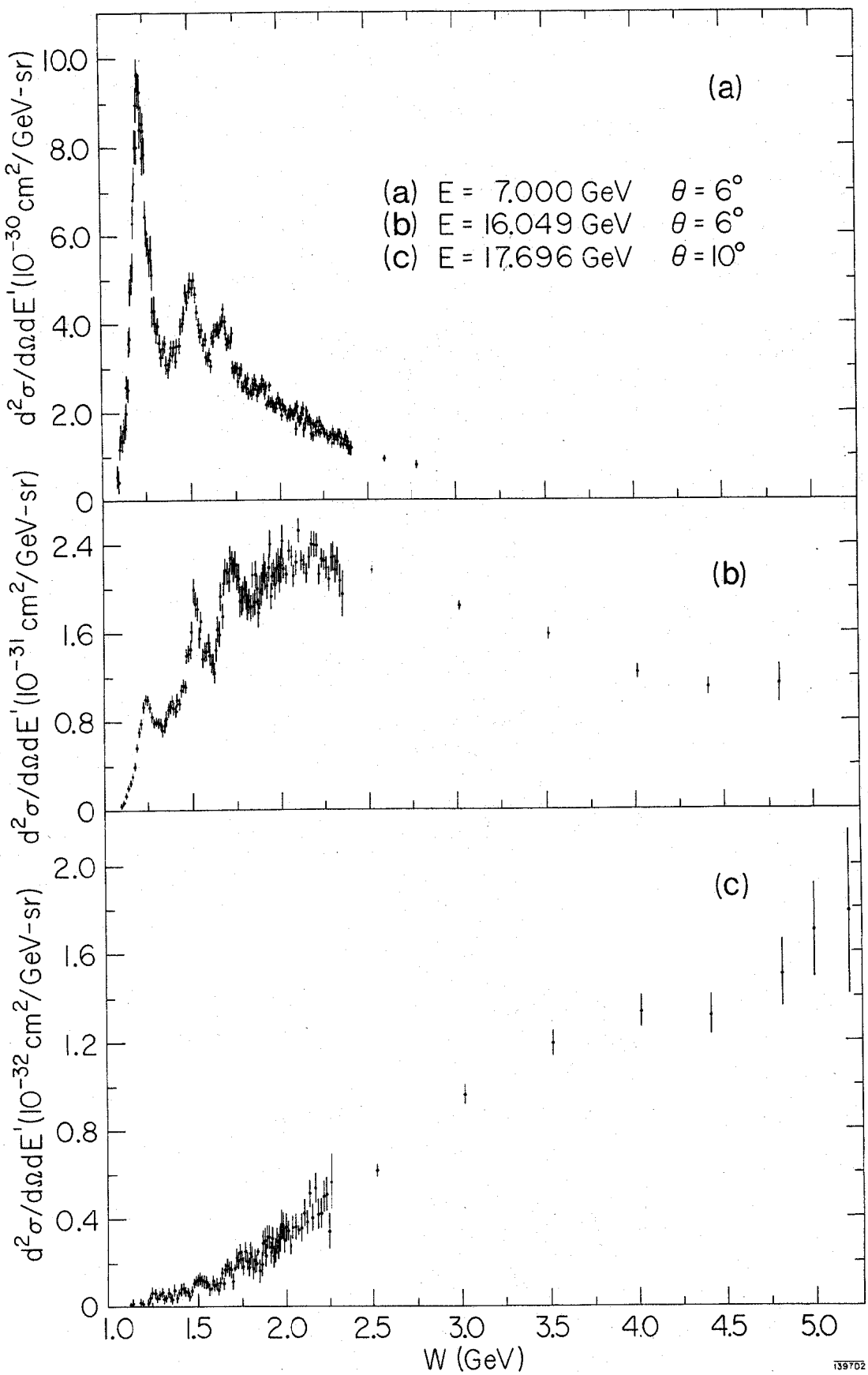
(a)
(a) E = 7.000 GeV θ = 6°
(b) E = 16.049 GeV θ = 6°
(c) E = 17.696 GeV θ = 10°
(b)
(c)
d²σ/dΩdE'(10⁻³⁰ cm²/GeV-sr)
d²σ/dΩdE'(10⁻³¹ cm²/GeV-sr)
d²σ/dΩdE'(10⁻³² cm²/GeV-sr)
W (GeV)
139702

Fig. 47

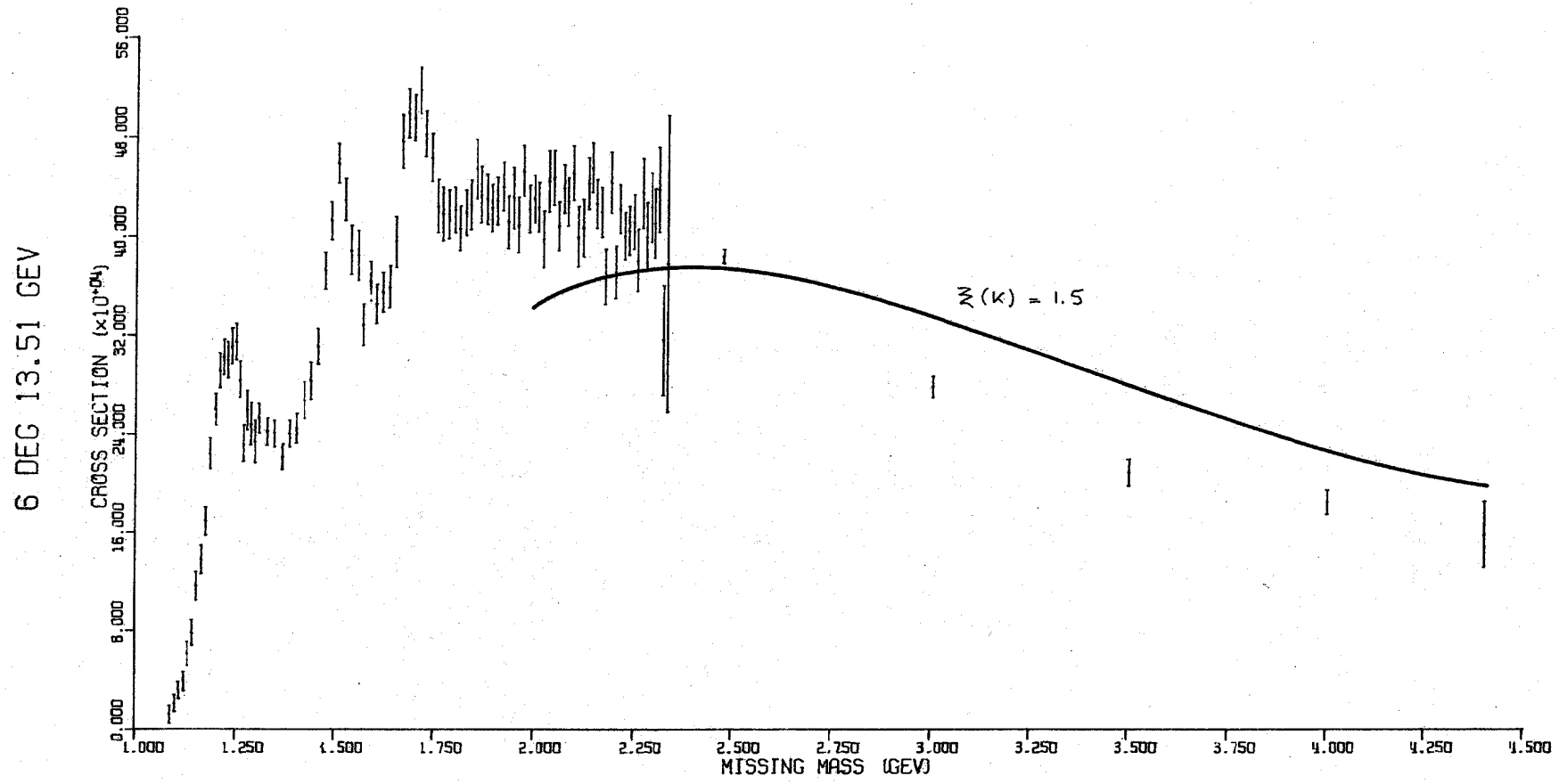
6 DEC 13.51 GEV
CROSS SECTION (x10**04)
0.000
8.000
16.000
24.000
32.000
40.000
48.000
56.000
1.000
1.250
1.500
1.750
2.000
2.250
2.500
2.750
3.000
3.250
3.500
3.750
4.000
4.250
4.500
MISSING MASS (GEV)
N(K) = 1.5

Fig. 48

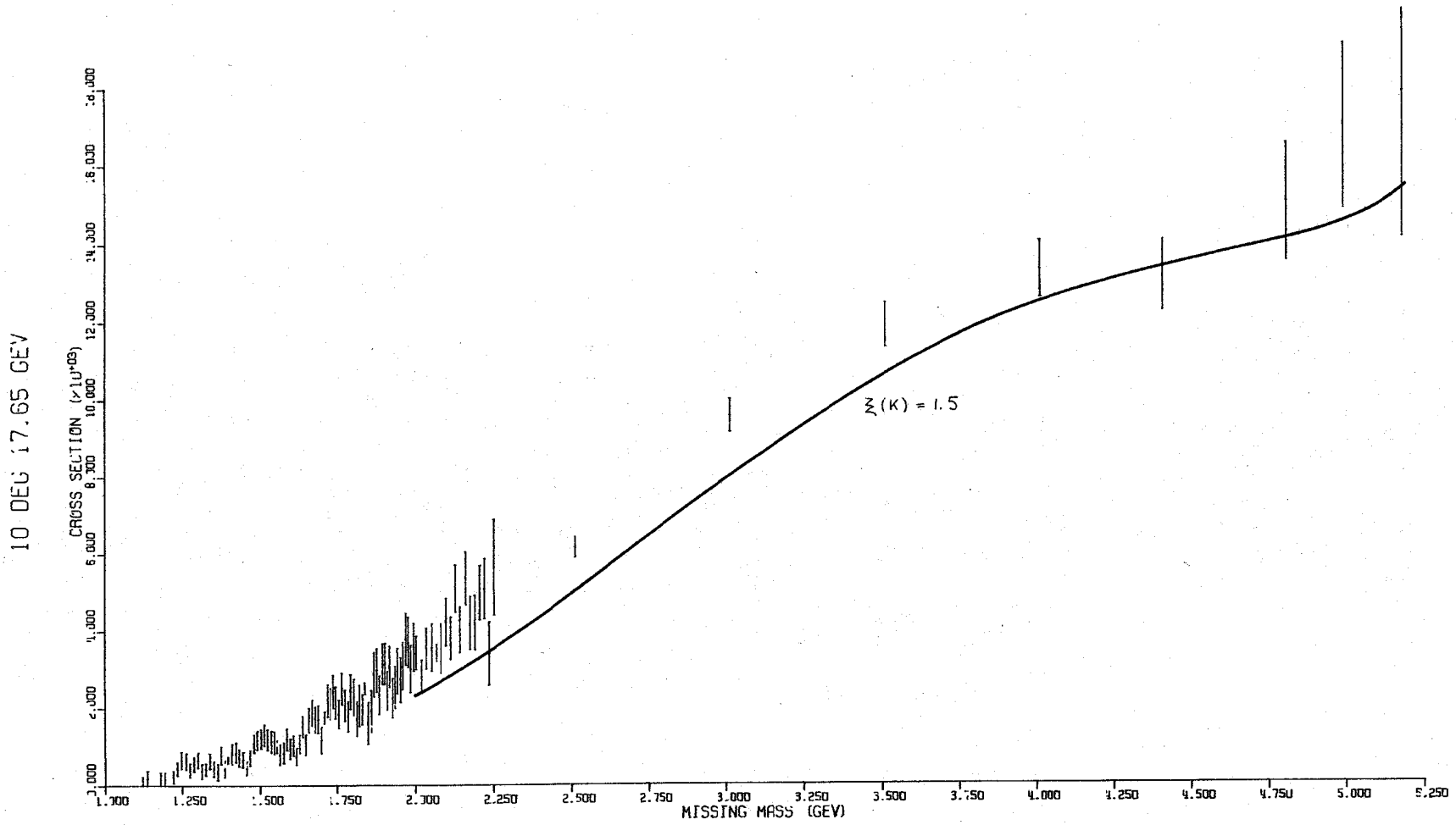

Fig. 49

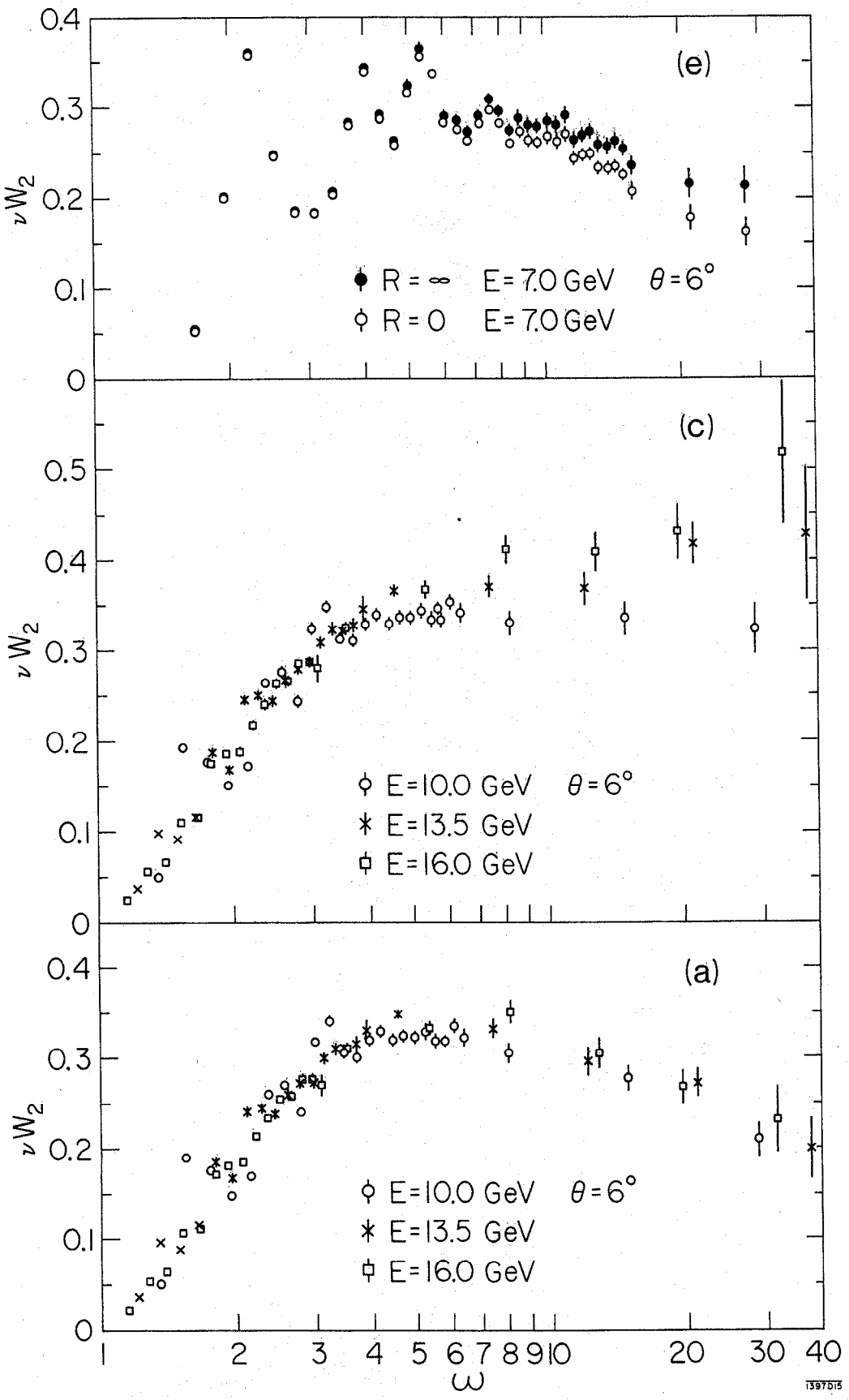
(e)
R = ∞ E = 7.0 GeV θ = 6°
R = 0 E = 7.0 GeV
(c)
E = 10.0 GeV θ = 6°
E = 13.5 GeV
E = 16.0 GeV
(a)
E = 10.0 GeV θ = 6°
E = 13.5 GeV
E = 16.0 GeV
νW2
ω
1397D15

Fig. 50

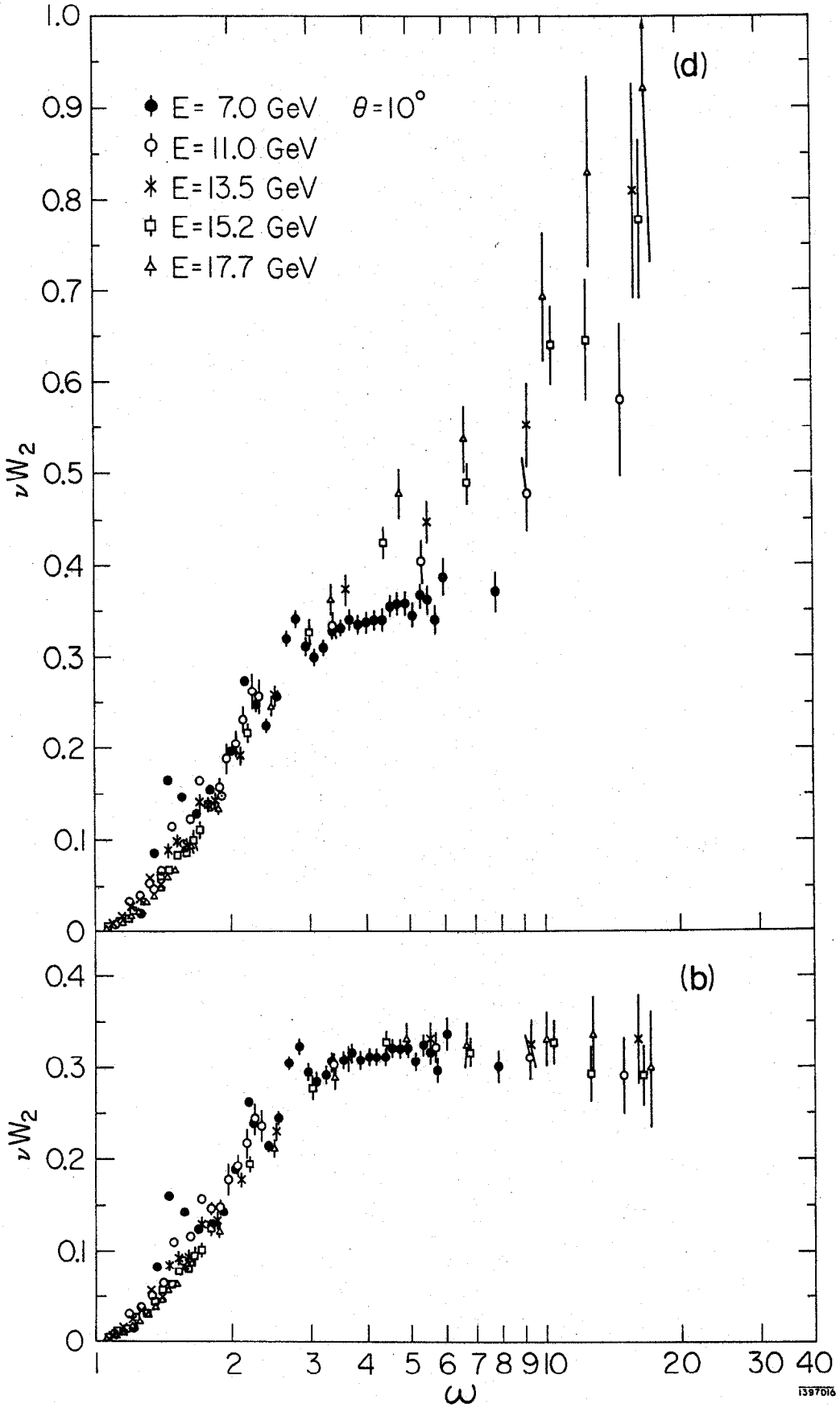
(d)
E= 7.0 GeV θ=10°
E= 11.0 GeV
E=13.5 GeV
E=15.2 GeV
E=17.7 GeV
νW2
(b)
ω
1397016

Fig. 51

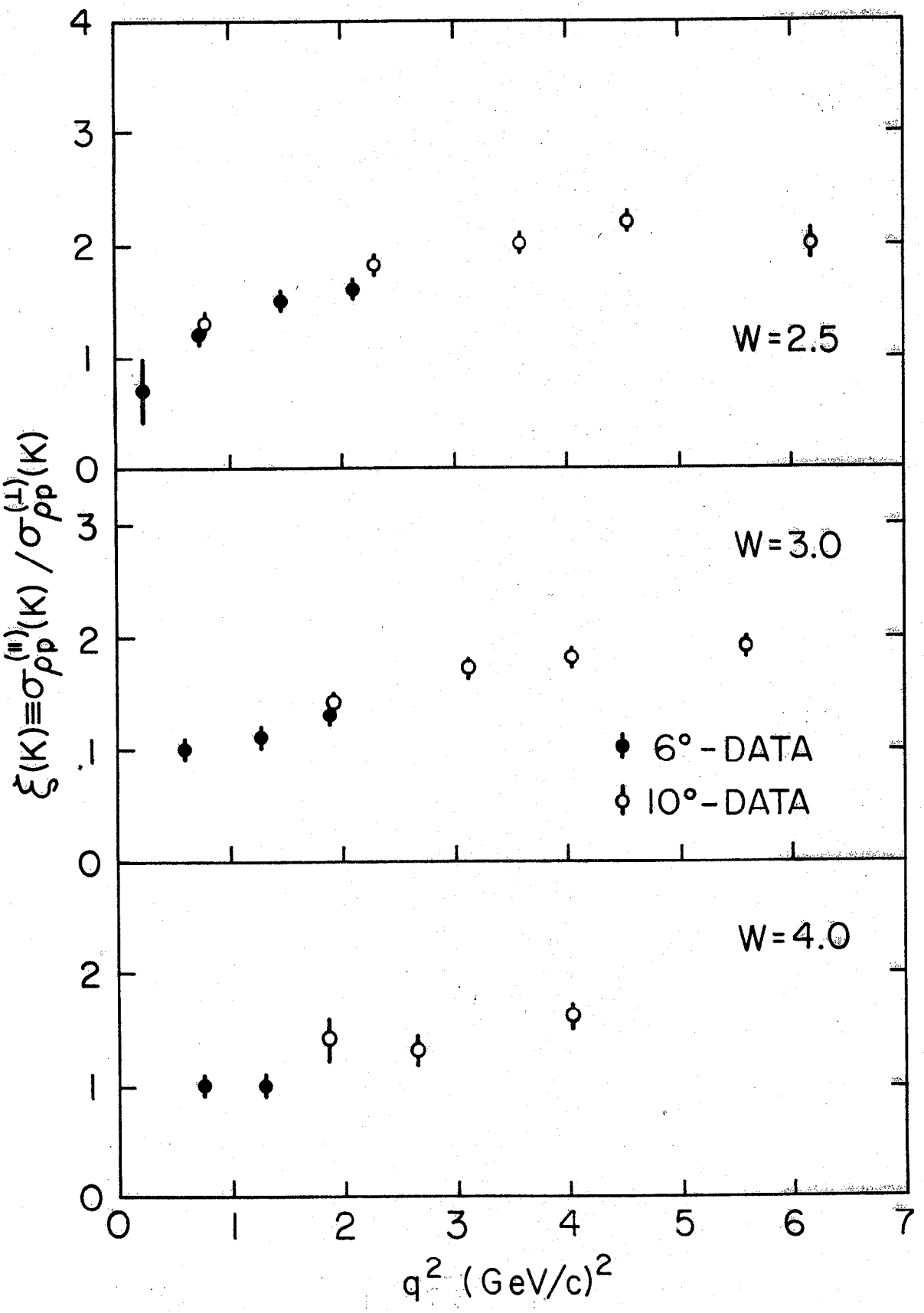
W=2.5
W=3.0
W=4.0
6°-DATA
10°-DATA
$\xi(K) \equiv \sigma_{pp}^{(\equiv)}(K) / \sigma_{pp}^{(\perp)}(K)$
q^2 (GeV/c)^2

Fig. 52

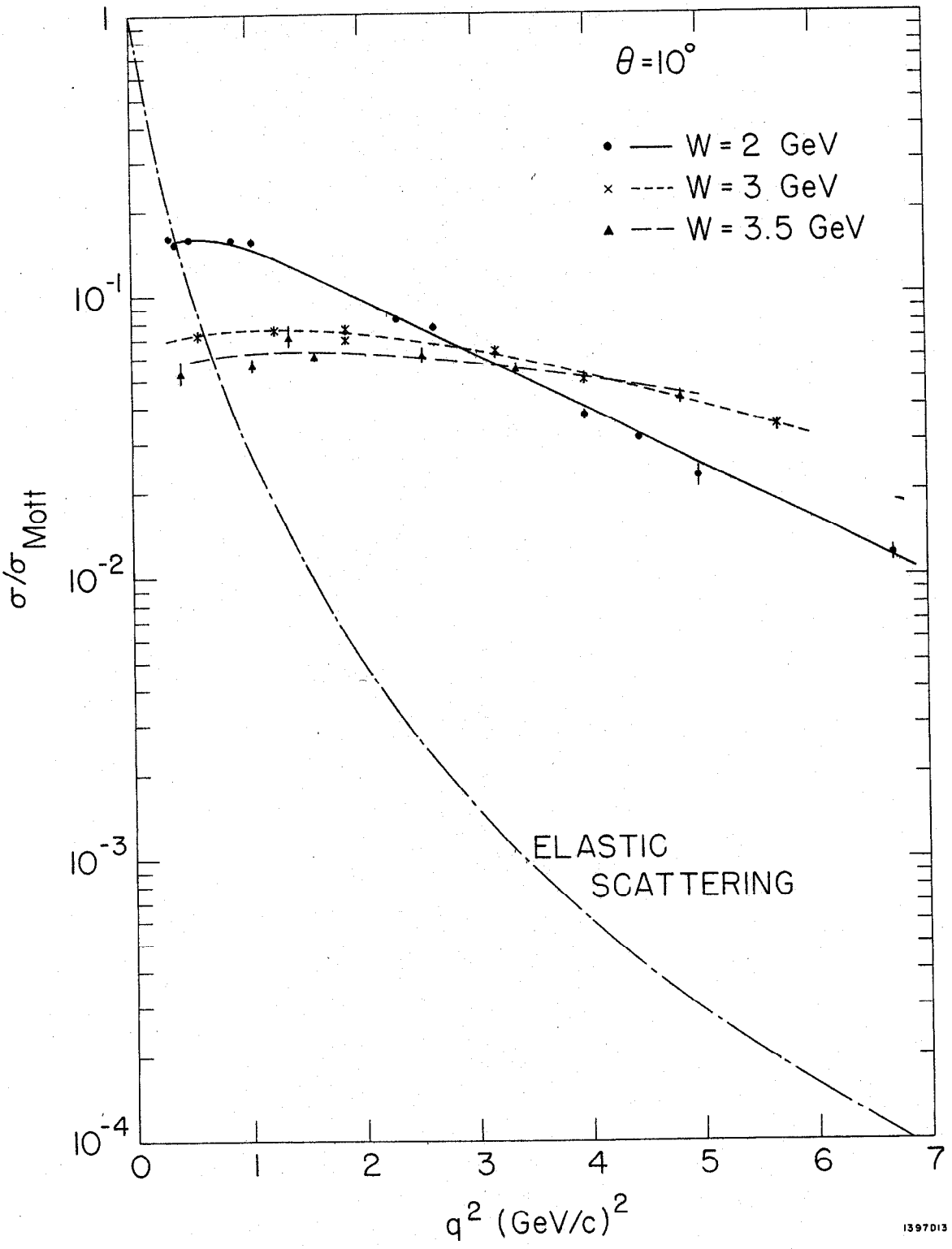
θ = 10°
• — W = 2 GeV
× ---- W = 3 GeV
▲ — — W = 3.5 GeV
ELASTIC
SCATTERING
σ/σ Mott
1
10^-1
10^-2
10^-3
10^-4
0
1
2
3
4
5
6
7
q^2 (GeV/c)^2
1397013

Fig. 53